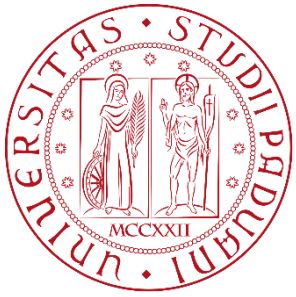

UNIVERSITÀ DEGLI STUDI DI PADOVA

Dipartimento Di Scienze Chimiche

Corso Di Laurea Magistrale In Scienza Dei Materiali

Tesi Di Laurea Magistrale

High power laser diode assembly processes: a study of the influence on the degree of polarization

Relatore:
Alessandro Martucci

LAUREANDA:
Sara Pinki Ranieri

Correlatori:
Alberto Maina
Natascia De Leo

Controrelatore:
Enrico Napolitani

ANNO ACCADEMICO 2021/2022

...dedicated to my grandparents

Table of Contents

Abstract

High-power semiconductor lasers play a key role in several fields of modern life. They have a consolidated use in many industries, where production processes often rely on high-power lasers for cutting, soldering and other treatment; but they also have applications in the medical field for surgery or in telecommunications, to mention the most known ones.

There are physical and technological constraints in the industrial production of high-power laser beams. A single chip device can only work at a limited amount of power so, where high power is needed, the common way to obtain it is through the combination of beams emitted by single sources (e.g. Chip on Carrier, CoC).

There are several ways of combining beams, with different levels of efficiency and different characteristics of the resulting beam; one of the most efficient methods is polarization beam combining. For this method to produce the best results, however, very strict characteristics of the single emitters are required. In particular, and here it comes the object of this work, a high polarization purity of the emitted beam is required, that is, the percentage of power in a pure polarization state (typically transverse electric, TE) out of the total power emitted.

It is known, and there is experimental evidence in this thesis, that the polarization purity, defined as “Degree of Polarization” (DoP), is strongly affected by the mechanical characteristics of the diode, which are determined during the production process.

A diode is a device made of a semiconductor assembled and connected. All of the processing involved in its production, the semiconductor wafer fabrication, the chip singulation, the chip mounting and the CoC assembly, may introduce mechanical stress.

This thesis focuses on experimental analysis of the influence of assembly processes on the Degree of Polarization for industrially produced laser diodes. More specifically, it studies the mechanical stress effects induced on the semiconductor, in function of different soldering parameter combinations.

The data obtained make it possible to identify critical assembly conditions that significantly influence the polarization state. Experimental data suggest possible optimizations of the production process that may increase the power emitted and improve the device's performances.

0 Introduction

Semiconductor optoelectronic devices, such as laser diodes, light-emitting diodes, optical waveguides, and photodetectors, have important applications ranging from telecommunications to biomedical. Semiconductor laser diodes, which represent one class of many different types of lasers, are suitable for industrial material processing applications and provide compact coherent light sources with high efficiency and emitted power.

Discovered in 1962 by the research groups at General Electric, IBM, and MIT, semiconductor lasers have been a breakthrough invention that revolutionized the industry. In combination with automated devices (i.e. robots) allowed for high volume/ high-quality production in manufacturing; made it possible for less invasive and aesthetic surgery; allowed for reliable telecommunications at once unthinkable speed. We can find laser applications in the mass market, for example in laser printing, not to mention the already obsolete laser CD reader.

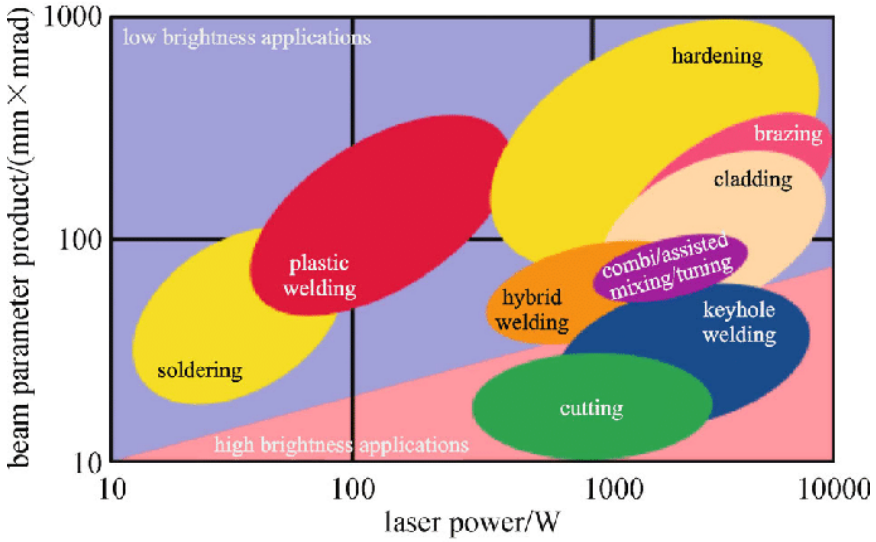

Figure 1 - Beam parameter product and laser power requirement for different material processing applications [29]

The beam quality and the power of the laser source needed depend on the applications for which the laser use is intended (*Figure 1*).
High-power semiconductor lasers are devices in which a diode, directly pumped with electrical current, generates light with the same phase, coherence, and wavelength creating lasing conditions at the diode's junction. Since the first work for high-power semiconductor lasers, the technology and market requirements have advanced dramatically.
Growing demand for higher power and the constant effort to reduce energy dispersion has driven laboratories and research centres around the world.

To improve high-power semiconductor lasers technology, a lot of effort has been spent in several fields. There have been great advances in technologies for semiconductor crystal production, in the development of double heterostructure lasers and, subsequently, in quantum well lasers. Materials passivation and heatsinking technologies have improved, as well as breakthroughs happened in device designs.

This thesis work is the result of an activity carried out inside the R&D group at Prima Electro S.p.A, a business division of Prima Industrie, mainly based in Turin, where high-power semiconductor lasers are developed and produced.
The work focuses on the analysis of the effects of the assembly process over the performance of high-power lasers. After studying the production process and the physics related to its different phases, we focused on the soldering phase and checked for different behaviour under different physical conditions.
Part of the experiment was the use of a manual tool to improve the soldering phase, one of the objectives is the checking its effectiveness, in order to evaluate industrial process integration.

The High-power semiconductor lasers studied in this work consist of edge-emitting diodes controlled with a current injection, an output power of around $15\ W$ can be obtained from a single emitter.
This kind of device emits radiation in the $900 - 980\ nm$ region, which allows for the coupling with optical fiber, to be used as an optical pumping source. Typical laser diodes are realized with *III-V semiconductors*, in particular InGaAs/AlGaAs alloys.

1 Laser Diode Theory

1.1 Semiconductors

Semiconductors are an intermediate step between insulators and conductors. The electronic structure of semiconductor crystals generally includes a set of allowed energy bands that electrons populate according to the rules of quantum mechanics. At the temperature of $0\ K$, the highest energy band is the valence band, which hosts the electrons participating in the chemical bonds and is entirely filled, the conduction band instead is entirely empty in absence of any excitation. In insulators, the valence band is separated from the conduction band by a large energy gap (Eg), of the order of a few electronvolts (eV). In conductive materials there is no gap. Depending on the dimension of the gap some materials may become conductive If energy is supplied to electrons in the valence band (i.e. increasing the temperature). [1] [2]

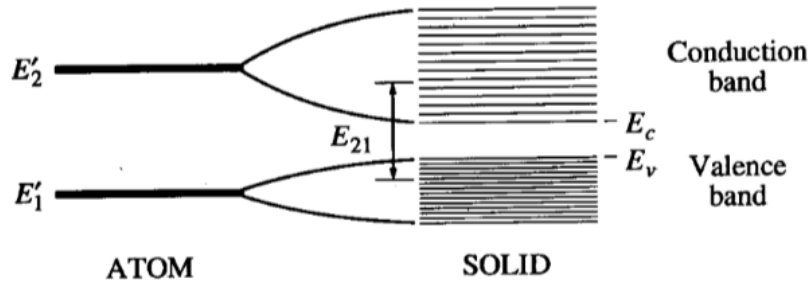

Figure 2 - Illustration of how two discrete energy levels of an atom develop into bands of many levels in a crystal [2]

In the case of a solid semiconductor, the presence of a lattice of covalently bounded atoms causes the separation of the energy levels of the single atoms and the consequent formation of bands of energy (*Figure 2*). The valence band is formed by the electrons that occupy the non-excited states at the highest energy while the immediately higher energy band is called the conduction band.

When an electron located in the valence band receives enough energy to overcome the forbidden band it can occupy an available level in the conduction band and leave a hole in the valence band. Electrons and holes constitute the mobile charge carriers that allow conduction into the material.

When electron state transitions between different energy levels are initiated by interaction with a photon, they can only occur between energy levels with the same momentum since the photon momentum ($\Delta E/c$) is negligible. The total momentum must be conserved, so the electron cannot undergo a momentum variation during the transition. This implies that the semiconductor used to realize the laser must have a direct-band gap, i.e. the minimum energy of the conduction band and the maximum energy of the valence band must be coincident (*Figure 3*). [3] [1]

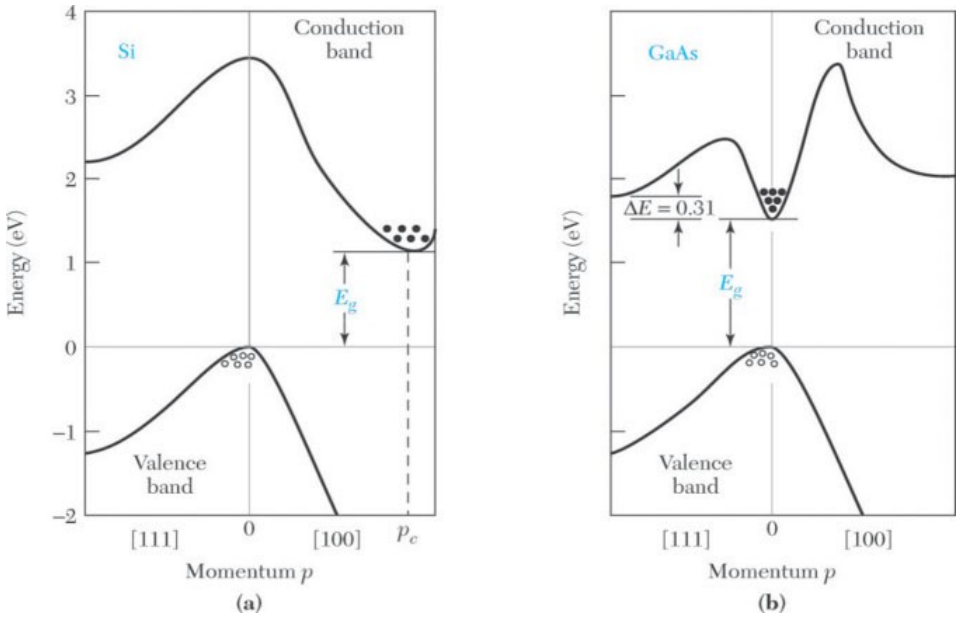

Figure 3 - Typically, direct-band gap semiconductors can absorb and emit light, while indirect-band-gap semiconductors absorb light but are unable to operate as high-efficiency light emitters, particularly in lasers. [3]

1.2 Electronic Transitions

As we have seen absorption and emission of a photon are associated with electronic transitions between states in the valence band and conduction band. The photon energy is given by the separation between levels according to: $h\nu = E2 - E1$.

The recombination and generation mechanisms of charge carriers can be schematized into four principal categories as shown in *Figure 4*.

♦ Spontaneous emission of a photon (or spontaneous recombination): it consists of the generation of a photon due to the recombination between an electron in the

conduction band (*CB*) and a hole in the valence band (*VB*) without any interaction with already existing photons.
The radiation emitted by these transitions turns out to be incoherent and with a wide spectral range, this is the case of LEDs.

♦ Absorption of a photon: it consists of the excitation of an electron from the valence band to the conductive band and the consequent generation of a hole in the valence band due to the interaction with a photon of proper energy.

♦ Stimulated emission: requires the interaction between photons and electrons in the conduction band, an incident photon perturbs the energetic system stimulating the recombination of a couple of electron-hole and generating the stimulated emission of a second photon coherent with itself. The emitted photon is characterized by the same wavelength, phase, polarization, and propagation direction of the incident photon. This kind of electronic transition is exploited in laser devices. Such a process requires electrons already present in the conduction band, a condition called population inversion that can be realized either through carrier injection (commonly used in high-power laser diodes) or by optically pumping the material (as in the case of optical fiber lasers). Population inversion is the fundamental requirement to have optical gain in the active material.

♦ Non-radiative recombination: it is an exchange of energy with impurities, other electrons, or with the crystalline lattice. These exchanges do not produce any photons, instead, we have thermal dissipation (phonon interaction). This effect is unwanted in semiconductor lasers and high-power devices and may lead to efficiency reduction or catastrophic optical damage.

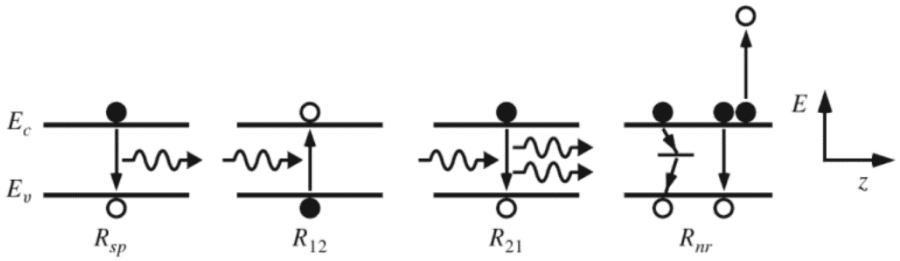

Figure 4 - Electronic transitions between the conduction and valence bands. The first three represent radiative transitions in which the energy to excite or dis-excite an electron is supplied by or given to a photon. The fourth illustrates two nonradiative processes. [2]

1.3 Laser Diode Working Principle

A diode is a two-terminal electronic component that conducts current primarily in one direction (asymmetric conductance); in other words, it has low resistance in one direction, and high resistance in the other.

Electrical proprieties of semiconductors can be modified by introducing a small concentration of impurities in order to change the number of charge carriers. It is possible to increment electrons in the conduction band, adding donor atoms which have an extra valence electron. These atoms introduce energy levels close to the conduction band, thus electrons can easily move through and reach it. With the same process, holes can be added introducing atoms that need one more electron to complete the bondings with the lattice atoms.

When donors are added to the semiconductor, the material is called *n doped* (it has more electrons in excess), while if acceptor atoms are added the material is called *p doped* (holes in excess). [1]

When an *n doped* semiconductor is put in contact with a *p doped* semiconductor a *PN* junction is formed.

A semiconductor diode is a crystalline piece of semiconductor material with a *PN* junction connected to two electrical terminals.

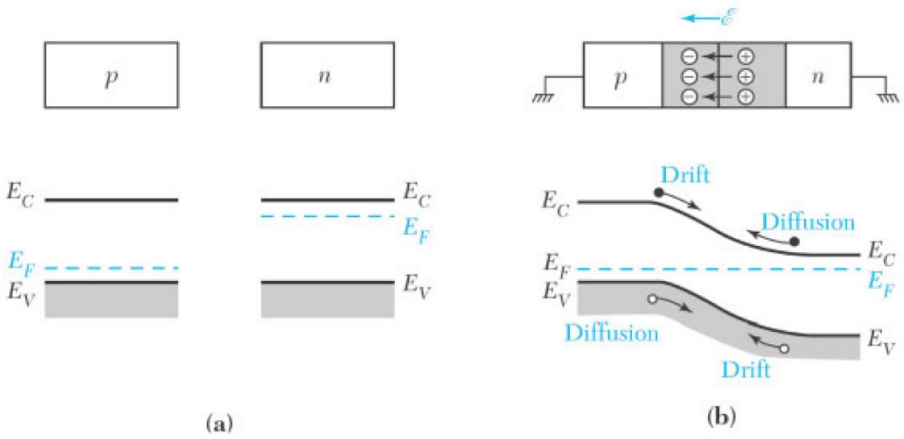

Figure 5 - a) Uniformly doped p-type and n-type semiconductors b) The electric field in the depletion region and the energy band diagram of a p–n junction in thermal equilibrium. [3]

By applying a voltage V connecting the negative pole to the *p side* and the positive pole to the *n side* the diode is polarized inversely. The presence of this voltage causes an increase in the potential barrier: there is therefore a reduction in the flow of majority charges, that is, electrons on side n and holes on side p are prevented from crossing the barrier. On the other hand, minor charge carriers are not affected, the holes on the n-side and the electrons on the p-side, therefore, contribute to create a current, called inverse saturation current. Such a current has a temperature dependence, doubling roughly in modulus every $10°C$.

The opposite behaviour is achieved if the junction is directly polarized (i.e. positive pole on the *p side* and negative pole on the *n side*). In this case, the voltage V is subtracted, lowering the potential barrier. There is no more equilibrium, electrons are injected from the *n side* while holes are injected from the *p side* through the interface region called the *depletion region*, the electrons of the n side (majority carriers) tend to move towards the *p side* while conversely, the holes from the *p side* move towards the *n side*: their sum creates a direct current in the diode.

This mechanism leads to the population inversion condition, which gives rise to radiative recombination.
This is the radiation used in lasers. Unfortunately, in ordinary *PN junctions*, the radiation is produced at very high current density threshold at room temperature (J_{th}~$10^5\ A/cm^2$) which makes it difficult to realize applications. To obtain radiation with a lower current density threshold, homojunction devices can be used. A homojunction is a semiconductor device or interface that occurs between the layers of similar materials, with equal bandgap but different doping concentration, while a heterojunction is the interface that occurs between two-layers or regions of dissimilar crystalline semiconductors. The concentration of multiple heterojunctions together in a device is called a heterostructure. [4]

In order to have radiative recombination with high performance a high density of carriers is needed, so it is important to get space confinement of electrons and holes in the junction. This can be done by creating potential wells that confine carriers. It is possible to build a structure to spatially confine both photons and charge carriers and so control the optical properties of the semiconductor. Carrier confinement is obtained

by realizing a quantum well, a double heterostructure (better explained later) of thickness comparable with the electronic wavelength (~100 Å) [5]. A thin slab of undoped active material (intrinsic) is sandwiched between p-type and n-type cladding layers having a minor energy gap. This forms a *PiN* junction. The main advantage of this approach is that the electronic potential inside the heterostructure creates a well in the intrinsic region in which electrons are confined. This enhances considerably the optical recombination rate and lowers the threshold current, or rather the value of the injected current at which the diode emits the laser beam. Since the band gap of cladding layers is larger than the quantum well's one, light generated in the active region will not have sufficient photon energy to be absorbed in them. The electron wavefunction is confined in the well ad its energy levels become quantized as shown in *Figure 6.*

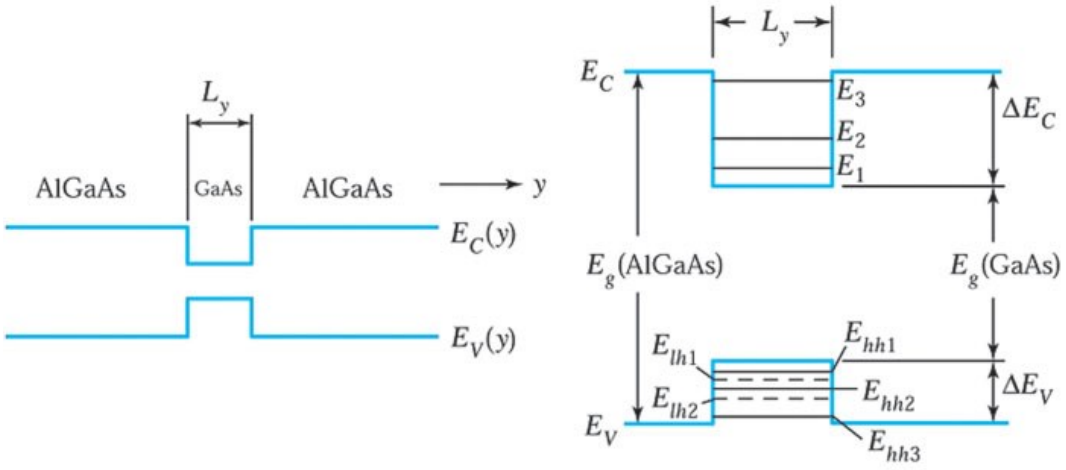

Figure 6 - The quantum-well (QW) laser: (a) single GaAs QW surrounded by AlGaAs, (b) discrete energy levels within the well [3]

There are several types of laser diodes that differ in structure and in direction of emission. In this work, we will discuss only the Fabry-Pèrot laser diodes.

As shown in *Figure 7,* the *p* and *n* semiconductor layers are packed in the upper and in the lower part of the epitaxial heterostructure (in yellow) and the QW active layer is embedded between them and has a thickness of a few nanometres. *P-side* and *n-side* contacts are composed of multiple layers of metals (contacts).

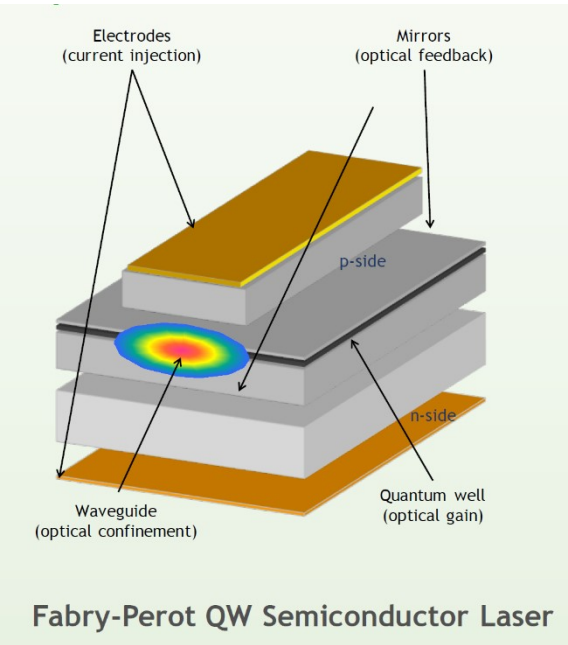

Figure 7 - Representation of a Fabry-Perot QW Semiconductor

The contacts allow the injection of carriers through the p-contact and the n-contact connected to the two poles of the power supply.

The package structure with the *p contact* above, named *epi-up* package structure, where the *n doped* chip substrate side is soldered to the carrier and the epitaxial layer side, which contains the active region, is wire bonded to form the p-connection, has been used for many years. In this configuration, the active region is well above the carrier and far away from the solder bonding interface which is the thermal transfer interface to the carrier. Since the epitaxial layer containing the active region is typically much thinner than the substrate, to minimize the thermal resistance and improve heat dissipation, it is favourable to build the laser diode in the *epi-down* configuration, with the *n contact* below, thus, the active region is normally only about a few micrometers away from the diode connection interface.

The *epi-down* structure has then replaced the *epi-up* structure in the making of high-power semiconductor lasers. The current injection flows into the laser chip from the *n side* metallization to the *p side* as shown in *Figure 8.*

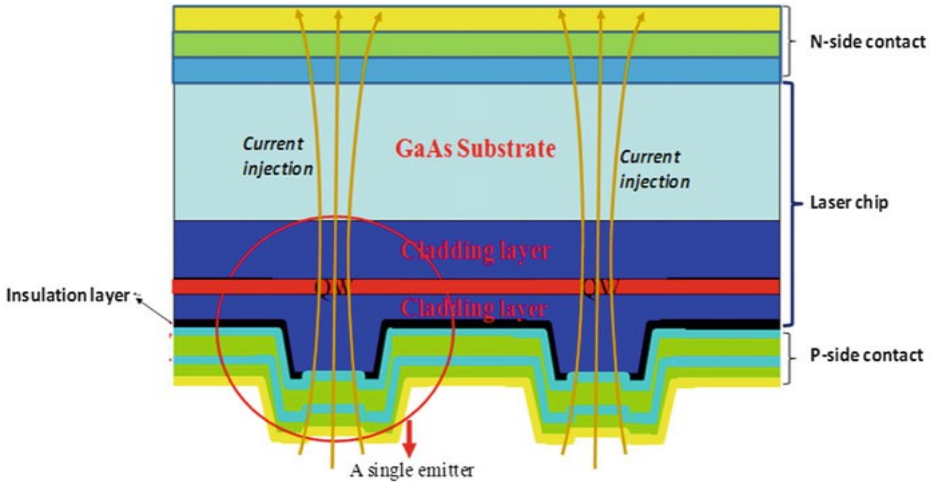

Figure 8 - Schematic structure of an epi-down bonded semiconductor laser

In order to amplify the optical energy obtained inside the active layer, an optical resonator is used. The optical resonator of a semiconductor diode laser consists of a waveguide structure between the mirrors made by crystal facet, see *Figure 9*. To achieve optimal reflectivity facets are coated with a dielectric material.

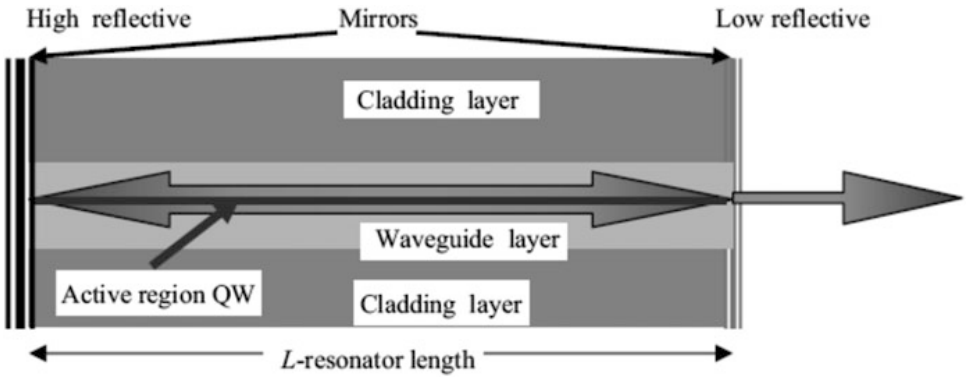

Figure 9 - The structure of the Fabry-Perot resonator of a diode laser

Light confined in a resonator will reflect multiple times between the mirrors and, because of interference, the resonator will sustain only certain patterns and frequencies of radiation, with the others being suppressed by destructive interference.

In general, radiation patterns that repeat themselves on every round-trip of light through the resonator are the most stable, and these are known as the modes of the resonator.

Resonator modes fall into two types: longitudinal modes, which differ in frequency from each other; and transverse modes, which may differ in both frequency and the intensity pattern of the light.

In the vertical dimension, perpendicular to the *PN junction* (which will be described later), the mode intensity distribution and the number of modes are determined by the thickness and composition of the epitaxial layers. Wave guide supports two polarization modes, one transverse electric (*TE*) and one transverse magnetic (*TM*). For the *TE* case, the electrical field vector oscillates in a plane parallel to the epitaxial layers; for the *TM* case, the electric field vector oscillates in a plane orthogonal to the epitaxial layers.

The semiconductor laser beam propagates in the form of the standing wave in the resonator as shown in *Figure 10*.

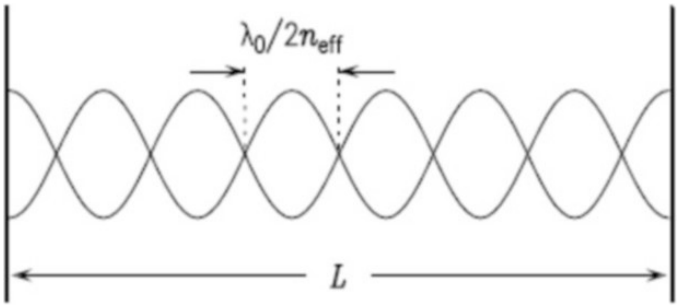

Figure 10 - The beam propagates in the form of the standing wave in the resonator

The distance between the mirrors is L and the effective refractive index of the optical waveguide is n_{eff} in the propagating direction. The resonator provides feedback when a standing wave develops between the mirrors.

$$L = m\lambda_0/2n_{eff}\ , \qquad m = 1, 2, 3, \ldots \tag{1.1}$$

where m indicates the number of nodes of the standing wave and the order number of the longitudinal mode, and λ_0 is the wavelength in vacuum. [6]

Semiconductor lasers generate stable laser beams when three conditions are satisfied: population inversion, optical gain, and stable laser oscillation.

1.4 Resonant Cavity and Optical Gain

Fabry-Pérot laser devices consist of a resonant cavity, where stimulated emission takes place, delimited by two semi-reflecting mirrors, one with high-reflectivity (*HR-facet*), to properly reflect the photons, and the other anti-reflective (*AR-facet*) from which the laser radiation is emitted.

The resonant cavity is realized with an active material, e.g InGaAs, properly chosen to amplify the light radiation at the desired frequency. In unperturbed conditions, the material absorbs the radiation without a gain but, if it is properly *pumped*, electrically or optically, the electrons of the active medium can be excited so that they are at a higher energy level than the equilibrium, in order to have the population inversion. The photons, which propagate through the resonant cavity, interact with charge carriers stimulating their recombination and hence causing the emission of new photons that in turn propagate through the resonant cavity producing an amplified stimulated radiation (optical gain). Laser emission takes place, through the AR-facet, when the gain compensates for the intrinsic losses inside the material. Then the process can reach the threshold to be self-sustainable and the active material starts to emit coherent light in a narrow spectral region. [3]

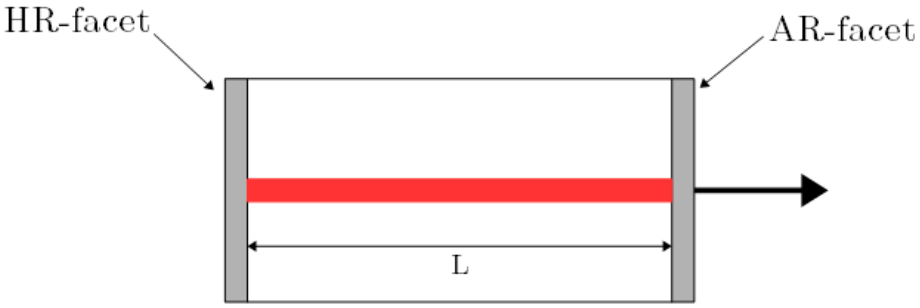

Figure 11 - Schematic representation of a resonant cavity

Photons reduction may happen because of different factors, for instance, the losses through the mirrors during light emission. Other issues are the absorption mechanism, the interaction of photons with free carriers, and the scattering. As the injection current increases, the number of injected carriers grows up as well, causing the rise of optical gain.

The optical gain which balances the loss is called the threshold gain, G_{th}. Only when the optical gain reaches the threshold gain G_{th}, the laser operation can be established.

The threshold gain G_{th} can be calculated as:

$$G_{th} = a_i + \frac{1}{2L}\ln\frac{1}{R_1 R_2} \tag{1.2}$$

where a_i is the internal loss coefficient. L is the length of the optical resonators, and R_1 and R_2 are the reflectivity of the two mirrors that compose the optical resonator. [6]

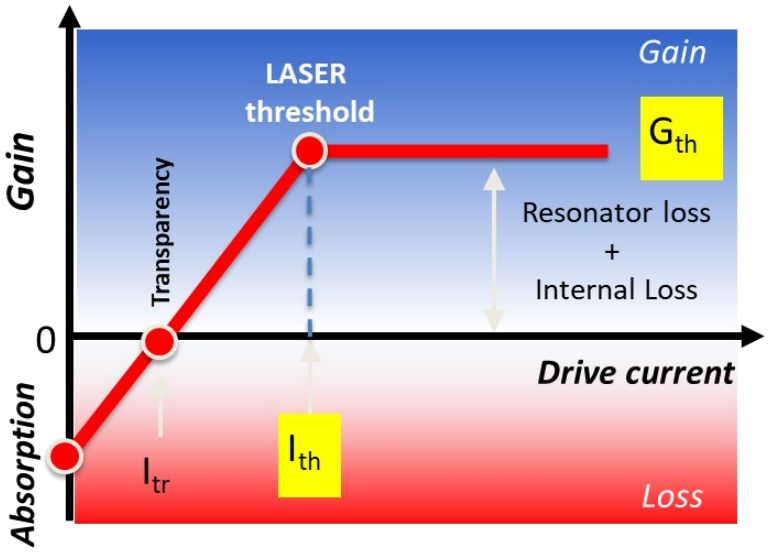

Figure 12 - Threshold gain representation

Once the injected current overcomes the threshold current the laser is triggered, and the power emitted increases linearly with the injected current value (*Figure 13*). [7]

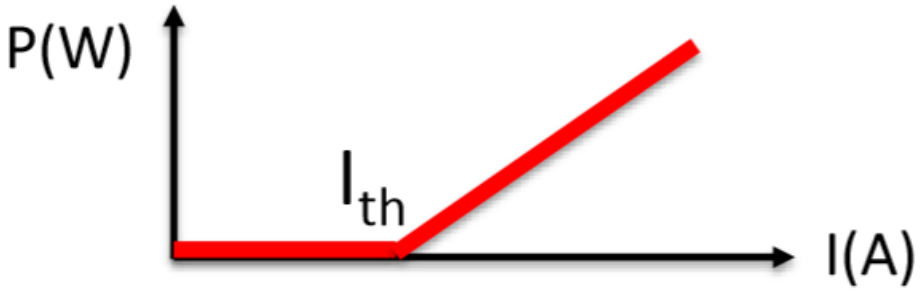

Figure 13 - Optical power emitted trend in function of injection current

1.5 Heterostructures and Quantum Well

Since the heterostructure is a waveguide, as already described in *Paragraph 1.3*, two sets of field configurations are allowed, called transverse electric TE and transverse magnetic TM modes.

The gain G_{th} in a normal heterostructure (bulk) is independent of polarization. In other words, it is the same for both *TE* and *TM* modes. This is no longer true when quantum well heterostructures are used. When the thickness of the heterostructure active region is of the order of the De-Broglie wavelength $\lambda_e \sim \frac{h}{p} \sim 100$ Å, quantum effects are no more negligible, and electron and hole energy levels become discrete.

A quantum well laser is a laser diode in which the active region of the device is so narrow that quantum confinement occurs. The wavelength of the light emitted by a quantum well laser is determined by the thickness of the active region rather than just the bandgap of the material from which it is constructed.The efficiency of a quantum well laser is also greater than a conventional laser diode due to the stepwise form of its density of states function.

Quantum well lasers have active regions of about 100 Å thickness, which restricts the motion of the carriers (electrons and holes) in a direction normal to the well. This results in a set of discrete energy levels and the density of states is modified to a two-dimension-like density of states. This modification of the density of states results in several improvements in lasers characteristics such as lower threshold current and higher efficiency. Quantum well lasers require fewer electrons and holes to reach the threshold than conventional double heterostructure lasers.

Successful production of diode lasers depends strongly on the properties of the materials involved. Nowadays the development of crystalline growth techniques has made it possible to produce epitaxial structures composed of several ultrathin layers (< 100 Å). In this way, it is possible to obtain a quantum well where charge carriers could be confined, and different layers with different refractive index allow to confine photons. To build the desired structure it is necessary to combine the same crystalline structure and almost the same reticular constant to avoid defects that become centres of non-radiative recombination.

Quantum well lasers have been manufactured using an active layer whose lattice constant differs slightly from that of the substrate and of the cladding layers. Such lasers are known as strained quantum-well lasers. Over the last few years, strained quantum well lasers have been extensively investigated all over the world.
The origin of the improved device performance lies in the band-structure changes induced by the mismatch-induced strain. Strain splits the heavy-hole and the light-hole valence bands at the Γ point of the Brillouin zone, where the band gap is minimum in direct band-gap semiconductors.

It is worth noting that every time an epitaxial growth is performed, stress acts on the heterostructure if the lattice parameters of the layers and the substrate are mismatched, and subsequently, strain in the material may become important.

The mismatch m is defined as:

$$m = \frac{a_L - a_S}{a_S} \tag{1.3}$$

where a_L, and a_S are the lattice parameters (physical dimensions that determine the geometry of the unit cells in a crystal lattice) of the layer and the substrate respectively. If $m > 0$ the strain is compressive, while for $m < 0$ the strain is tensile.

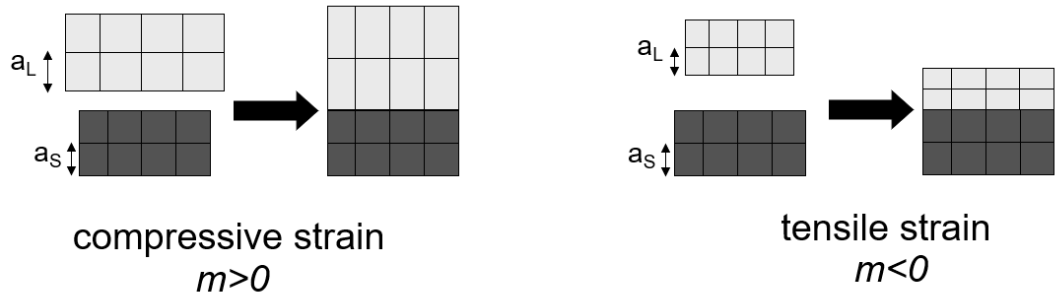

Figure 14 - Kinds of strain

Semiconductor laser devices are built using alloys made of elements of the *III-V groups* in the periodic table, *Figure 15*, which provide the wavelength needed for the specific application, for example, emitting in the $900 - 980\,nm$ range for material processing. [8]

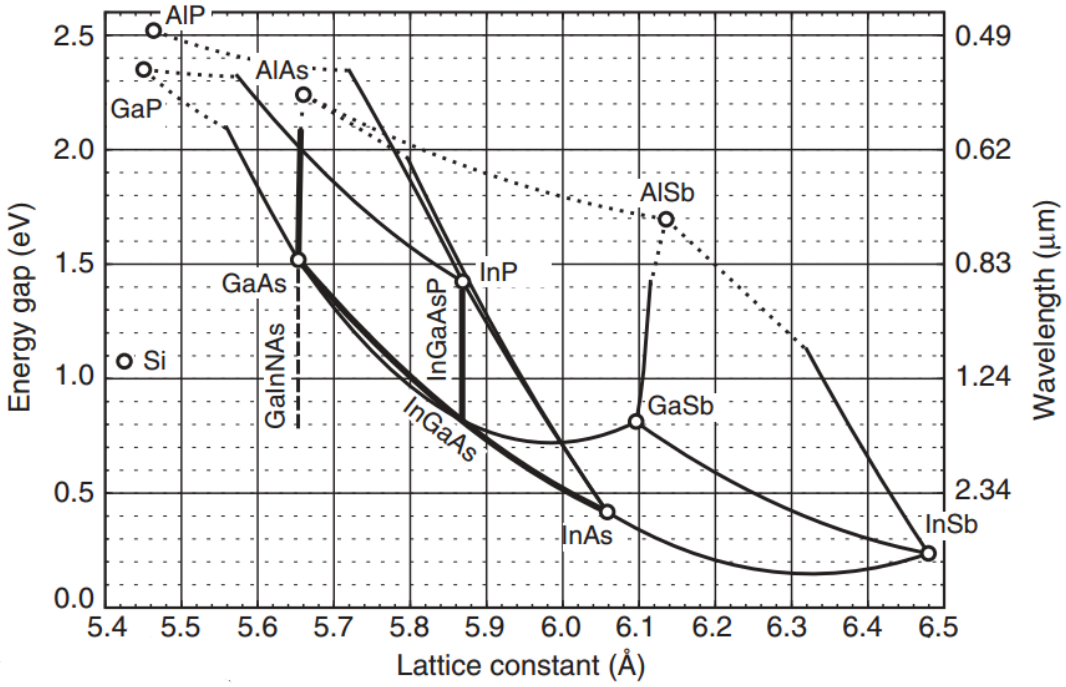

Figure 16 - Semiconductor alloy diagram [2]. *The structure is realized in AlGaAs/GaAs but, to be able to optically pump the fiber laser, the quantum well consists of a single layer of InGaAs which provides the proper wavelength.*

This kind of alloys have a similar band structure, characterized by a conduction band, and two valence bands, degenerate at the band Γ edge ($k = 0$), called heavy-hole and light-hole bands.

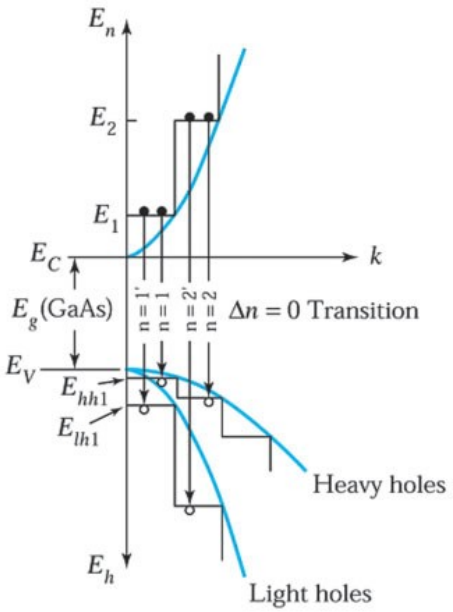

Figure 15 - *Scheme of the energy bands of III – V semiconductor* [3]

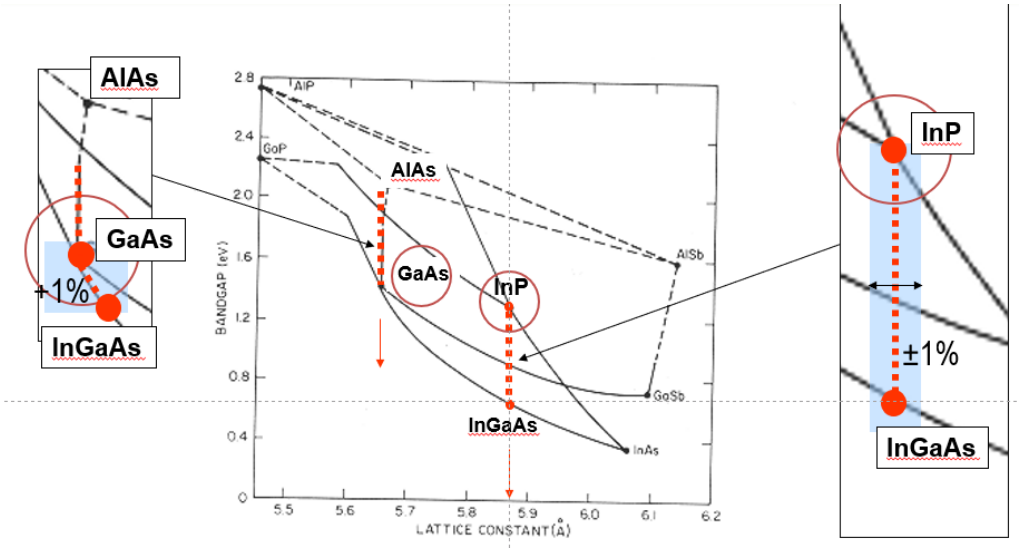

Figure 17 - *Energy gap vs lattice constants for different materials. The two highlighted in red are the main alloys used for semiconductor lasers*

As it is shown in *Figure 17* a quasi-bidimensional structure is created, called a quantum well, where charge carriers are forced to move in the plane transverse to the epitaxial growth direction.

The main advantages of quantum well structures are the following:

• lower threshold current density

• 1% of strain is allowed

• gain G_{th} becomes polarization-dependent.

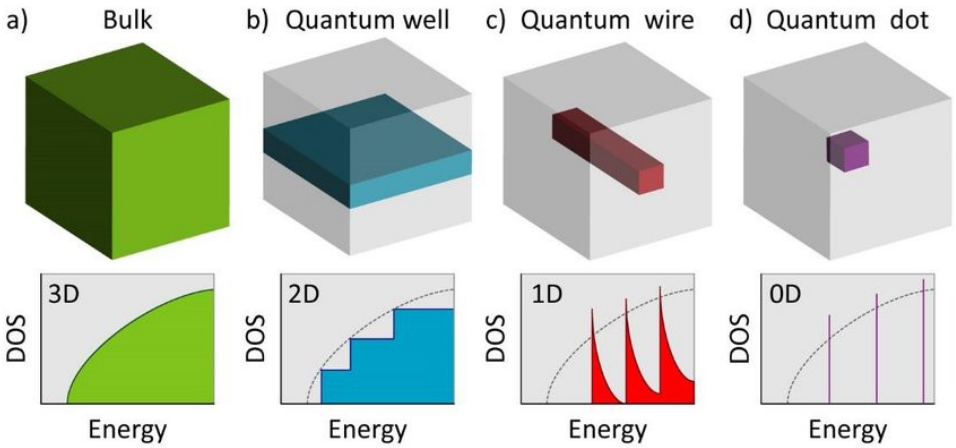

Figure 18 - *Bulk material and some quantum mechanics structures for carrier confinement with their respective density of states functions (DOS).*

1.6 Photons and Charge Carriers Confinement

As seen, in a diode laser we must simultaneously control two different kinds of particles: photons and electrons. Different equations describe the dynamic of each particle. The photons propagation is governed by Helmholtz equation, while electrons are governed by Schrodinger's equation in the case of a quantum well.

Helmholtz equation: $\left[\frac{d^2}{dz^2} + {k_0}^2 n^2(z)\right] \Psi(z) = {n_{eff}}^2 \Psi(z)$ (1.4)

Schrodinger's equation: $\left[-\frac{\hbar^2}{2m}\frac{d^2}{dz^2} + V(z)\right] \Psi(z) = E\, \Psi(z)$ (1.5)

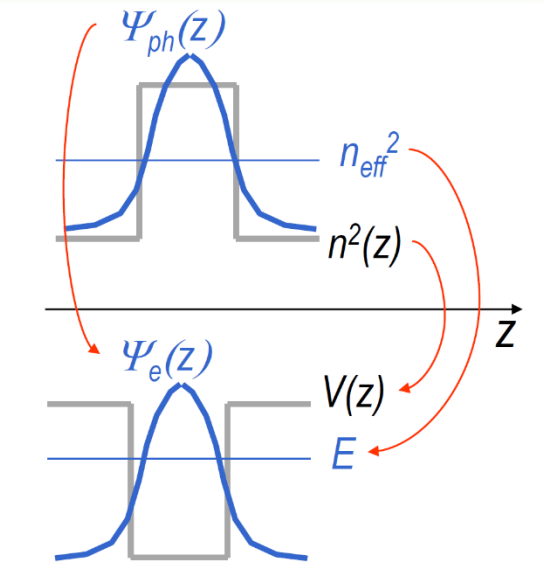

Figure 19 - Photon and electron confinement

To reach the lasing conditions we must confine both electrons and photons in a narrow region, the active region. As anticipated, to confine electrons we need a quantum well while to confine photons we have to create a waveguide.

The engineering of the materials constituting the laser diode allows to modify its optical and electrical properties, giving the possibility to control the behaviour of photons and electrons inside the device. In particular, the laser diode is made with a multilayer structure in order to form profiles of different energy gaps and different refractive indexes. Electronic confinement is achieved by the quantum well, creating a potential well where the energy gap is smaller than in the adjacent layers. In this layer, the recombination of the charge carriers is favoured by a lower energy variation

between the bands of the adjacent material. When the layer is thin enough, $8\,nm$ in the studied case, there are quantum effects: the available states are discretized and the transitions of the carriers no longer take place between bands, but between discrete energy levels.

The optical confinement provides the high photon density needed for the laser diode and it is realized with a separate confinement heterostructure (SCH) in the vertical direction and a waveguide in the horizontal direction. The characteristic dimensions of these waveguides are much larger than the quantum well thickness, being the optical wavelength longer than the electronic one.

In the horizontal direction, the waveguide is fabricated with a ridge structure in which a chemical etch process is used to remove part of the material, thus introducing a significant refractive index variation $n(z)$, the intrinsic region refraction index n is greater than the cladding one. In the vertical direction, instead, the index guiding is realized with layers having different refractive indexes. The vertical waveguide is realized during the epitaxial growth using *III-V* compounds but with a different composition in each layer. Both lateral and vertical confinements are schematically represented in *Figure 20*.

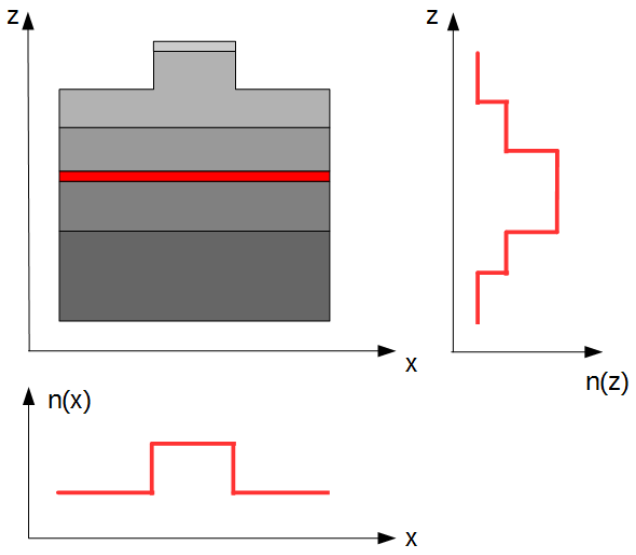

Figure 20 - Optical confinement with a ridge structure

Optical confinement occurs in two directions: along the vertical axis, because of the refractive index profile of epitaxial materials, while along the horizontal axis it is due to effective index variation. The presence of a ridge determines a horizontal refractive index profile with a maximum in correspondence to the ridge, able to laterally confine the optical beam. The resulting waveguide is therefore rectangular and, regarding the *Figure 21*, the confinement is in the xy plane while the propagation occurs along the z direction.

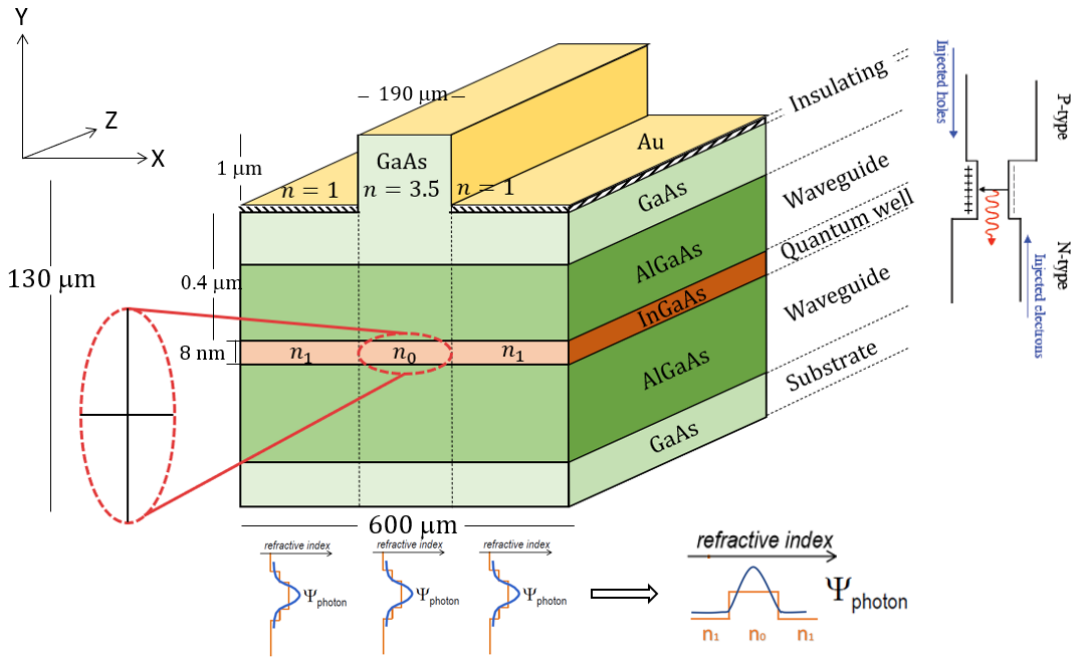

Figure 21 - Schematic representation of the complete structure of the laser diode. (The proportions are not respected for representative reasons).

1.7 Fiber Lasers

In material processing and, in particular, in the processing of steel and other metals, the laser beam used must have two important characteristics. First of all, it has to be a high-power laser beam, in the order of magnitude of kW, moreover, the optical beam must preserve a high brightness, because a high-power density is needed. Laser diodes alone are not able to satisfy both requirements since a single laser diode can emit a high-brightness laser beam, but the power reached is in the order of tens of watts. Combining many beams, the required power can be achieved, but the brightness is partially lost. Due to this limitation, laser diodes are typically used as optical pumping sources for rare-earth-doped fiber lasers. The active fiber is a laser whose

active medium consists of the core of the active fiber doped with rare earth elements (*Figure 22*).

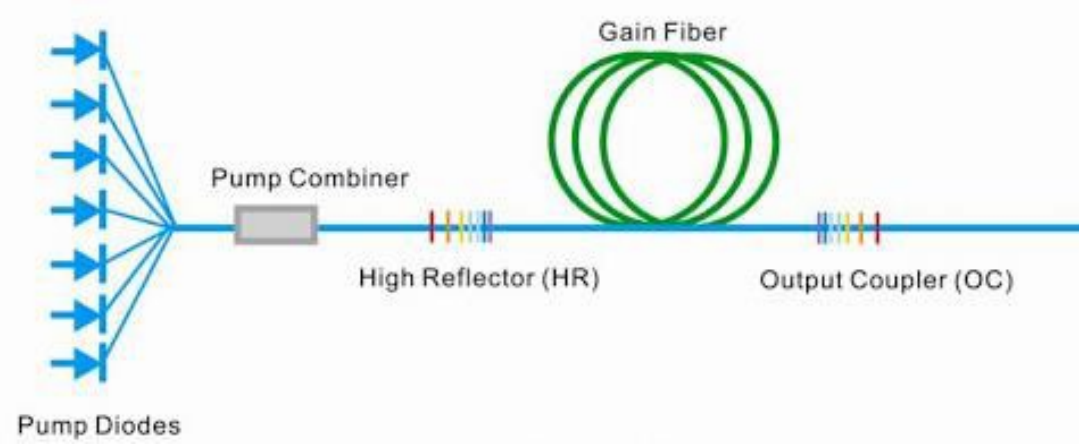

Figure 22 - *Scheme of the laser in active fiber*

Optical pumping is realized by using a structure called a multi-emitter. [6] It consists of a series of laser diodes welded in a package. The diodes are positioned side by side, but with a slight difference in height that allows the optical beams to not interfere with each other except at the moment of entering into the core of the output fiber.
This superposition degrades the beam quality, but the resulting output beam has high optical power. The active fiber is ytterbium-doped and amplifies light by stimulated emission. The photons from the multi-emitter array are injected into the active fiber to excite ytterbium ions to metastable states.
The optical confinement is realized by the difference in the refractive index between the core and cladding layers of the fiber itself.

Although the brightness of the beam coupled into the fiber is degraded, due to the coupling of numerous beams from the laser diodes, the beam generated by the fiber has high brightness. This is because the photons in the optical pump beam are not correlated with the photons emitted by the active fiber, therefore there is no correlation between the geometric properties of the incoming beam and those of the beam emitted by the fiber.

2 Optical Beams Coupling

The optical pumping of the active fiber requires a power of the order of kW. Although high-power laser diodes are very efficient, it would be unthinkable to obtain such a high output beam power using just one device. It is therefore necessary to add up the power emitted by many laser diodes. In the multi-emitter, a Fast Axis Collimator (FAC) is placed in front of each laser diode. It consists of a semi-cylindrical lens, which has the function of collimating the optical beam along the most problematic axis in terms of divergence. A Slow Axis Collimator (SAC) is placed a few mm further in the direction of propagation of the beam. The SAC has the function of collimating the optical beam along the other axis. The collimated beams are reflected by mirrors properly oriented to make them converge on an output lens, whose focus lies in the core of the output fiber *(Figure 23)*.

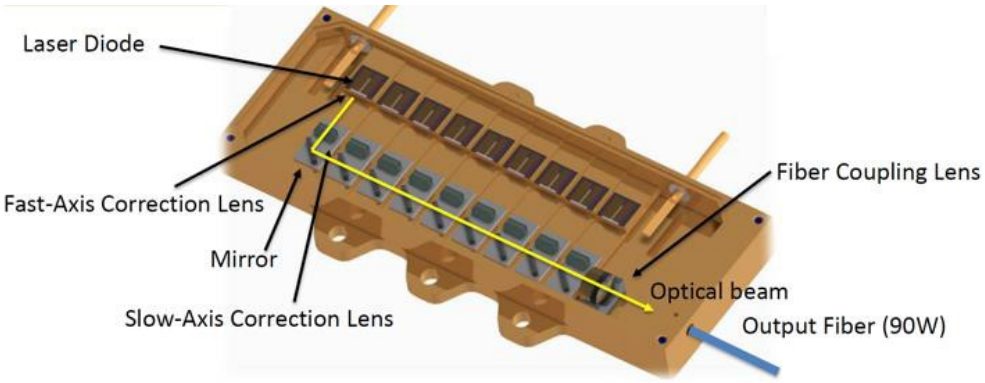

Figure 23 - Multi-emitter for coupling of optical beams emitted by laser diodes

The resulting beam power equals the sum of the powers of all the beams involved in the coupling, reaching values of one hundred Watts or higher. Then adding the output optical beams of every multi-emitter through fused fiber optic couplers, a power of kWs is reached, which is needed for the optical pumping of the active fiber.

2.1 The coupling problem

The optical coupling of single beams emitted by the laser diodes has an important limitation. The resulting beam, in fact, has a lower brightness than that of original single beams. To analyse this, a new parameter, the Beam Parameter Product (or *BPP*) [6], must be introduced. *BPP* represents the quality of an optical beam and

how well it can be focused into a small spot. It is defined as the product between the semi-divergence θ and the beam semi-width w measured at the output mirror surface in the case of an edge emitter laser *Figure 24*.

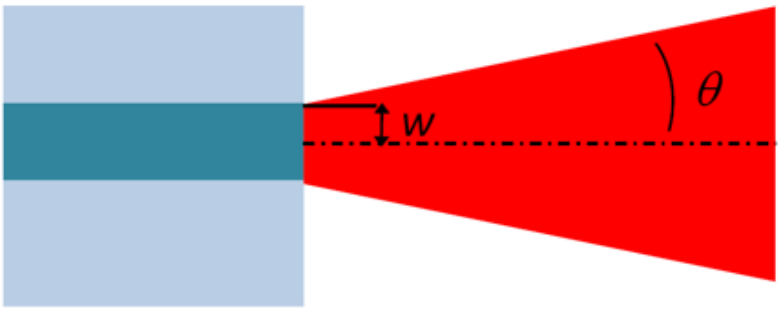

Figure 24 - Schematic representation of the optical beam emitted by the laser diode where θ is the semi divergence and w is the beam semi-width

$$BPP = w \cdot \theta \ [mm \cdot mrad] \tag{2.1}$$

In an ideal Gaussian beam, which corresponds to the highest quality optical beam, this BPP value is the lowest achievable. The *BPP* reaches its ideal minimum when:

$$BPP_{gauss} = \frac{\lambda}{\pi} \tag{2.2}$$

Where λ is the wavelength of the electromagnetic radiation constituting the optical beam.

It is useful to define the beam propagation ratio M^2 parameter, which relates the beam quality of a real beam with the one associated with the ideal Gaussian beam [9]:

$$M^2 = \frac{BPP}{BPP_{gauss}} = \frac{w\theta\pi}{\lambda} \geq 1 \tag{2.3}$$

Where M^2 is called beam propagation ratio and is a dimensionless index of the quality of the optical beam, widely used.

Of course, the ratio M^2 will always be greater than or equal to 1 meaning that no real beam can reach the quality of an ideal one.

When optical beams are coupled in order to obtain a single more powerful beam, the resulting *BPP* is also increased. With two coupled beams, the final *BPP* is about twice the original *BPP*.

We can define the brightness as:

$$B = \frac{P_{out}}{\pi w^2 \pi \theta^2} = \frac{P_{out}}{\pi^2 BPP^2} \; [W\ cm^{-2} sterad^{-1}] \tag{2.4}$$

While in the ideal case the maximum theoretical brightness obtainable is:

$$B = \frac{P_{out}}{\lambda^2} \tag{2.5}$$

As we can see, the brightness of an optical beam is inversely proportional to the square of its *BPP* and, as the *BPP* increases when two or more optical beams are coupled, then the resulting brightness decreases quadratically. Given that the highest value of B is desired, then the *BPP* should be as small as possible, and its value depends on the material processing efficiency.

The loss of brightness is not always a problem, there are fields of applications where this parameter is less important or even irrelevant. However, in the field of material processing, and in particular, in metal processing, it is very important to maintain a very high brightness, because it is necessary to focus the high-power laser beam in a very small spot on the material to be processed. Thus, the increase in BPP, and therefore the decrease in brightness, during the coupling of the optical beams is a great issue that greatly hinders the reaching of greater output power.

The lasers studied in this thesis use incoherent coupling, which consists in combining beams that originated from two distinct sources and therefore placed at different points. For two optical beams to collimate and converge at the same point (for example on the output lens) they must interact differently with some optical components present in the multi-emitter.

To make this happen, photons belonging to different beams must in some way differ by one of their characteristics (direction, wavelength, state of polarization) [10]. Hence, here arises the need to distinguish the photons involved in the coupling and

this can be achieved in different ways. The simplest one to realize, but more degrading from the point of view of the *BPP*, is the spatial beam multiplexing.
The mirrors of each of the laser diodes have a slightly different direction so that the optical beams can be oriented towards the same point (output lens), this would result in a total power that will be the sum of each single laser beam power:

$$P_{TOT} = \sum P_i \tag{2.6}$$

Unfortunately, also the following relationship holds:

$$BPP_{TOT} \approx \sum BPP_i \tag{2.7}$$

which means that the resulting *BPP*, defined in (*2.1*), will be approximately the sum of the BPP of every single beam. Since (*2.4*) holds, which states that the brightness *B* is inversely proportional to the squared of the *BPP*, even though the output beam power is increased, it would result in major brightness losses.

Another way consists in polarization coupling, which is based on the coupling of two beams with complementary polarization status. As we will see in the next paragraph, the light emitted by the laser diodes is *TE* (transverse electric) polarized, so it is possible to perform the coupling through a half wave plate that allows rotating the polarization state of one of the two beams incident, making its polarization state shift from *TE* to *TM* (transverse magnetic). *(Figure 25)*

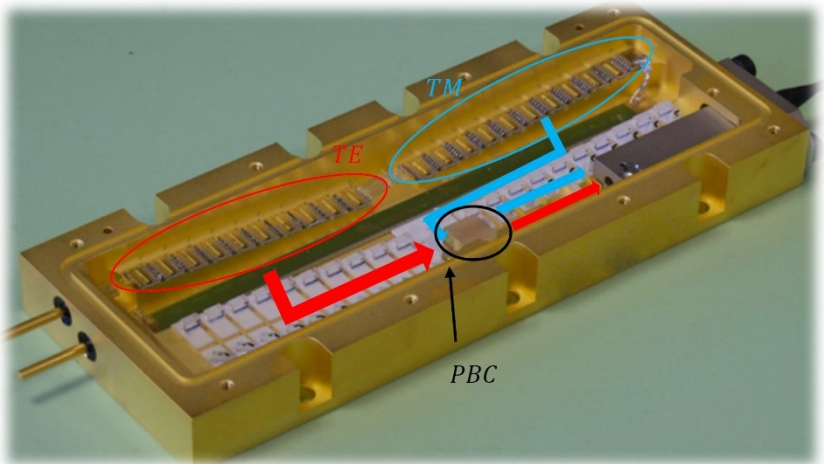

Figure 25 - A multi-emitter that uses the polarization multiplexing

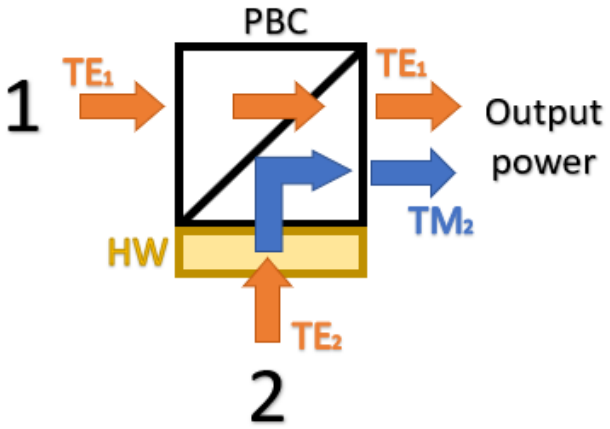

Figure 26 - PBC (Polarizing Beam Splitter) scheme

Since semiconductor lasers usually emit only in *TE* polarization, by sending the first laser beam (*TE* polarized) on the left of the *PBC* (input 1 in *Figure 26*), it will be transmitted and will pass through the *PBC*. Sending the second laser beam (again *TE* polarized) on the lower side of the *PBC* (input 2 in *Figure 26*) and interposing a halfwave plate, this will rotate the polarization state from *TE* to *TM* and the beam will be reflected by the *PBC*. In this way the two beams, having two different origins and entering the *PBC* in different directions, can be oriented in the same direction, resulting in a combination of a single beam preserving *BPP* and then brightness, with the doubled power.

Within this process, the degradation of the degree of polarization would be a problem (as we will see in more detail in the next chapter), and this would result in a loss of power from the two incident laser beams.

2.2 TE/TM Gain

We have seen that to couple two optical beams without increasing the *BPP* using the technique of polarization multiplexing, it is necessary to start from two polarized beams. This is possible because the optical beams emitted by laser diodes are polarized and generally have a high degree of TE polarization. The reason of this characteristic lies in the different gain that photons with different polarization states have within the resonant cavity of the laser diode.

We have seen that the carriers in the laser diode are confined in a quantum well and this thin layer of material is grown on a bulk semiconductor material having different

lattice parameters, this induces stress in the material. The electronic levels in a QW depend on the carrier mass, thus being different the heavy-hole mass and the light-hole mass the degeneracy between their energy is removed. Moreover, the strain has the effect of further removing heavy holes and light holes degeneracy at the band edge, moving away, or approaching their potential line-ups. [11] The final consideration has important consequences on the optical beam polarization: in a quantum well the heavy holes and light holes interact differently with the electric field. The gain G_{th} is proportional to the quantum dipole matrix element that, for a quantum well at the band edge, is proportional to the following values:

Heavy holes, TE: $3/4$

Heavy holes, TM: 0

Light holes, TE: $1/4$

Light holes, TM: 1

For compressive *QW*, like the one used in the present investigation, it is found that the wavelength of the *QW* gap, coinciding with the transition electron-heavy hole (*eh1-hh1*), strongly favours the gain for the *TE* polarization. Accordingly, the emitted and amplified optical beam at 976 nm will be *TE* polarized. (*Figure 27*)

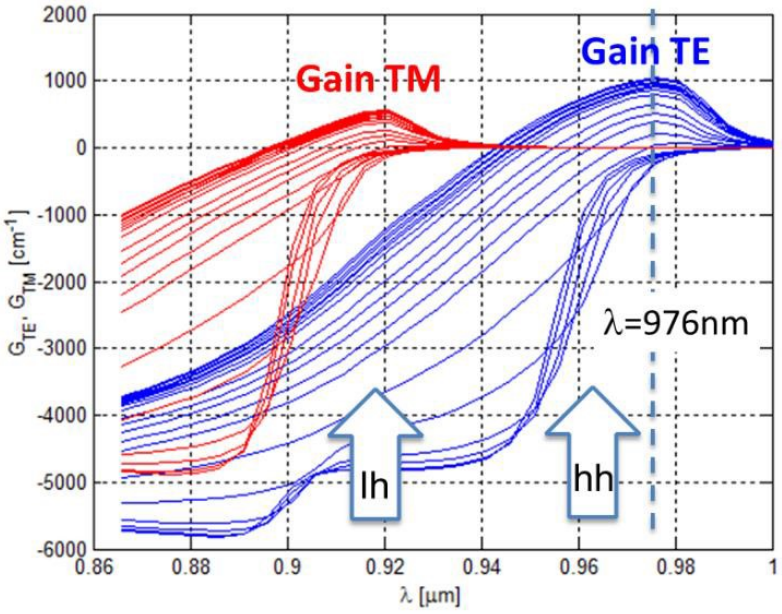

Figure 27 - TE and TM modes gain as a function of the photon wavelength

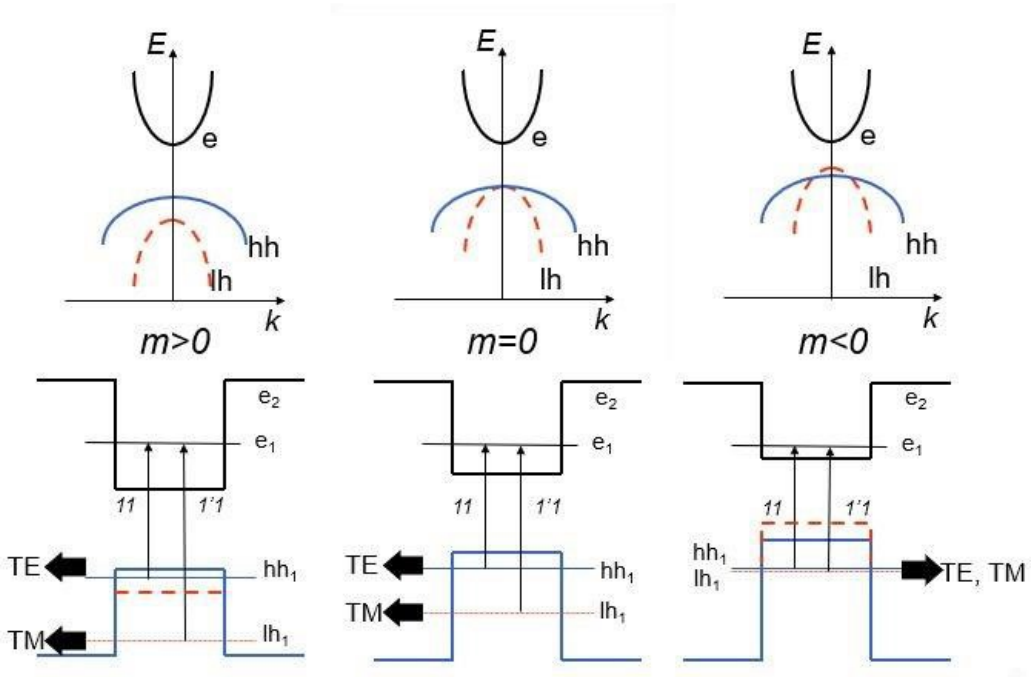

Figure 28 - Effect of strain on quantum wells. Heavy holes-light hole degeneracy is broken if there is a lattice mismatch. Valence band line-ups can be neared (tensile strain) or moved away (compressive strain) and the output optical beam, due to the first electron heavy hole optical transition, can be composed of pure TE modes or both TE and TM modes.

Separating heavy holes and light holes band line-ups can further improve the degree of polarization (this is the main theme of the thesis, and it will be discussed in the next chapters). This result can be obtained if a strain is applied to the material. When compressive strain is applied, heavy holes and light holes potential line-ups move away from each other, and this results in pure *TE* radiation at the laser emission wavelength.

To get the best results in beam coupling total polarization is wanted, so here comes the need to have an emitted beam completely TE polarized. We will see, in the next chapter, that when a photon changes its polarization from *TE* to *TM*, because of some external stress, it will not contribute to the stimulated emission and some power is lost.

3 Degree of Polarization (DoP)

The main theme on which this thesis is focused is the Degree of Polarization (DoP) of the laser beam and its preservation.

For mainly *TE-polarized* laser beams, like those emitted by high-power laser diode investigated here, this is defined as:

$$DoP = \frac{P_{TE}}{P_{TE}+P_{TM}} \tag{3.1}$$

where P_{TE} and P_{TM} are the *TE-polarized* and *TM-polarized* optical power, respectively.

The intrinsic *DoP* of a high-power laser diode can be very high, due to proper active material design aiming to maximize the *TE/TM* gain ratio. However, inevitable mechanical stress is introduced when the laser diode is mounted on the carrier causing a relevant reduction in DoP. [12] The *DoP* reduction implies important effects on the overall laser functional characteristics. The threshold current and slope efficiency are affected by the *DoP* reduction, and the analysis of the relevant changes is of general interest for the investigation of the stress-induced photoelastic effect on laser diodes.

3.1 Photoelastic Effect

Mismatch induced by the epitaxial growth is not the only stress to which the material is subjected. The described structure of the laser diode highlights the presence of different layers of material, such as metals and dielectric layers used for the electrical contact. Different materials have different mechanical and thermal properties. In particular, metals are more subject to deformation as the temperature varies, unlike more stable dielectrics. When the metal layers cool down after deposition, which occurs at around $100°C$, the contraction they undergo is greater than the dielectric on which are deposited. This contraction difference generates mechanical stresses at the interface. Also, the soldering process of the chip on the carrier (this operation is described in the next chapter) is an important source of stress for the device, both for the elevated temperature at which the chip is soldered (about $350°C$) and because of the not-planar profile of the semiconductor material, as the presence of the ridge for the optical confinement of the waveguide. [13]

The different sources of stress determine a strain in the material which in turn produces a change in the optical properties due to the photoelastic effect. The dielectric permittivities, hence the refractive indices, for different orientations in a crystal are in general functions of the strain in the material. The strain that results from die bonding is often not uniform like the strain that results from an epitaxial layer mismatch, in which case it may be possible to predict accurately the strain from the known material parameters. [12]

The reason why the photoelastic effect is so impacting on the polarization state of the optical beam is to be found in the mixed terms of the stress tensor:

$$\sigma = \begin{pmatrix} \sigma_{xx} & \sigma_{xy} & \sigma_{xz} \\ \sigma_{yx} & \sigma_{yy} & \sigma_{yz} \\ \sigma_{zx} & \sigma_{zy} & \sigma_{zz} \end{pmatrix} \tag{3.3}$$

The anisotropic mechanical stress, due to the technological process and the mounting process, changes the refractive index an it not only acts along the main axes but involves all directions. This means that the variation of the refractive index will not only affect diagonal components but also mixed components. Refractive index components are related to the stress components through the following equation [14]:

$$\begin{pmatrix} n_{xx} \\ n_{yy} \\ n_{zz} \\ n_{xy} \\ n_{xz} \\ n_{yz} \end{pmatrix} = \begin{pmatrix} n_{xx}^0 \\ n_{yy}^0 \\ n_{zz}^0 \\ n_{xy}^0 \\ n_{xz}^0 \\ n_{yz}^0 \end{pmatrix} = \begin{pmatrix} C_1 & C_2 & C_2 & 0 & 0 & 0 \\ C_2 & C_1 & C_2 & 0 & 0 & 0 \\ C_2 & C_2 & C_1 & 0 & 0 & 0 \\ 0 & 0 & 0 & C_3 & 0 & 0 \\ 0 & 0 & 0 & 0 & C_3 & 0 \\ 0 & 0 & 0 & 0 & 0 & C_3 \end{pmatrix} \times \begin{pmatrix} \sigma_{xx} \\ \sigma_{yy} \\ \sigma_{zz} \\ \sigma_{xy} \\ \sigma_{xz} \\ \sigma_{yz} \end{pmatrix} = \begin{pmatrix} n_{xx}^0 + \Delta n_{xx}^s \\ n_{yy}^0 + \Delta n_{yy}^s \\ n_{zz}^0 + \Delta n_{zz}^s \\ n_{xy}^0 + \Delta n_{xy}^s \\ n_{xz}^0 + \Delta n_{xz}^s \\ n_{yz}^0 + \Delta n_{yz}^s \end{pmatrix} \tag{3.4}$$

where n_{ij}^0 are the unperturbed components, Δn_{ij}^s are the stress-induced changes, and

$$C_1 = \frac{n_0^3(p_{11} - 2\nu p_{12})}{2\Upsilon} \qquad C_2 = \frac{n_0^3[p_{11} - \nu(p_{11} + p_{12})]}{2\Upsilon} \qquad C_3 = \frac{n_0^3 p_{44}}{2G}$$

The parameters p_{ij} are the strain-optic constants; Υ, G, and ν are, respectively, the Young's modulus, the shear modulus, and the Poisson's ratio of the material layers. [15]

Refraction index anisotropies have the effect of rotating the electric field polarization, lowering the *DoP*.

3.2 Setup DoP Analysis

The purpose of this analysis is to measure the DoP of the optical beam emitted by a diode laser mounted on different types of supports and using different soldering conditions.

In the next chapters, we will compare the DoP of diodes before and after soldering on the heat sink; the variation in the DoP value changing the soldering condition is studied as the DoP line trends in function of the current.

During the measures the emitted light power can reach 10W, as the emission wavelength is in the IR region, it is not visible, but at the same time, it is highly damaging to the human eye. High-power laser diodes studied in this thesis are classified in hazard class 4, according to the international standard enshrined in the norm IEC SN EN 60825-1:2014. The danger classes are summarized in the following table.

1- Not Dangerous
2- Low Risk, P < 1 mW, VISIBLE
3R- Medium Risk, P < 5 mW, VISIBE
3B- High Risk, P < 500 mW
3- High Risk also for spread beam, dangerous for eyes and skin

Figure 30 - Picture of the laboratory and the DoP experimental set-up

The measures of the degree of polarization of the bars, the chips on carrier (CoC) and the CoC mounted on the heat sink (HS) have been carried out at an optical bench realized expressly for this purpose; *Figure 29* shows a view of the experimental bench in the Prima Electro laboratory.

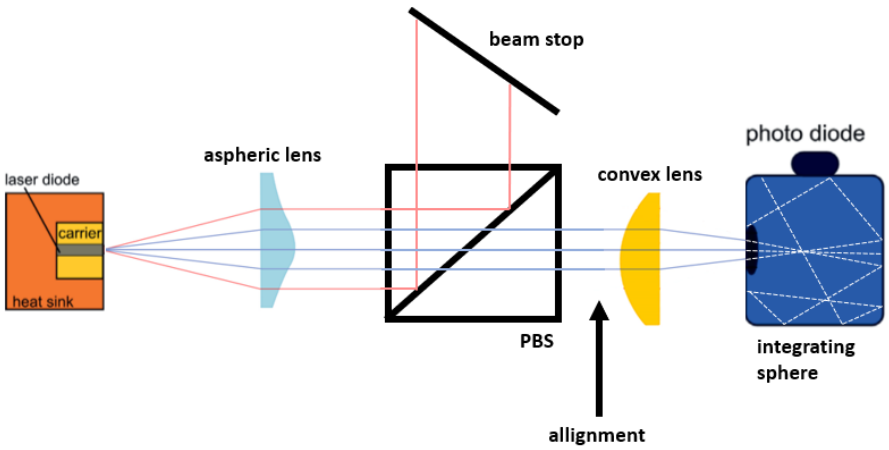

Figure 29 - DoP experimental set-up: top-view and scheme representation

3.2.1 Electronic and thermal instruments

For the experiment, a LABVIEW-controlled current generator supplies a current ranging between 1 and 12 A.

A Peltier Cell, in conjunction with a heat spreader plate, is used to set the CoC temperature and for its fine adjustment. The Peltier cell is directly below the CoC device and can thus immediately modify the temperature. It is connected to a thermal controller that provides the required current for setting the temperature. A thermocouple, positioned below the device used, gives a tension signal that is analysed by the thermal controller.

Positioning CoC, bars and HSs, on a support made of an Indium plate allows for the refinement of thermal contact.

In order to refrigerate the device, a refrigerator system is connected to the CoC support. It is positioned under the lower surface of the Peltier cell and is made of a cold plate in which a copper serpentine, controlled by two valves, carries cold-water. The flow completes the circuit in a chiller which brings back the temperature to $18{,}5°C$, in order to maintain a constant temperature of $25°\ C$ on the diode.

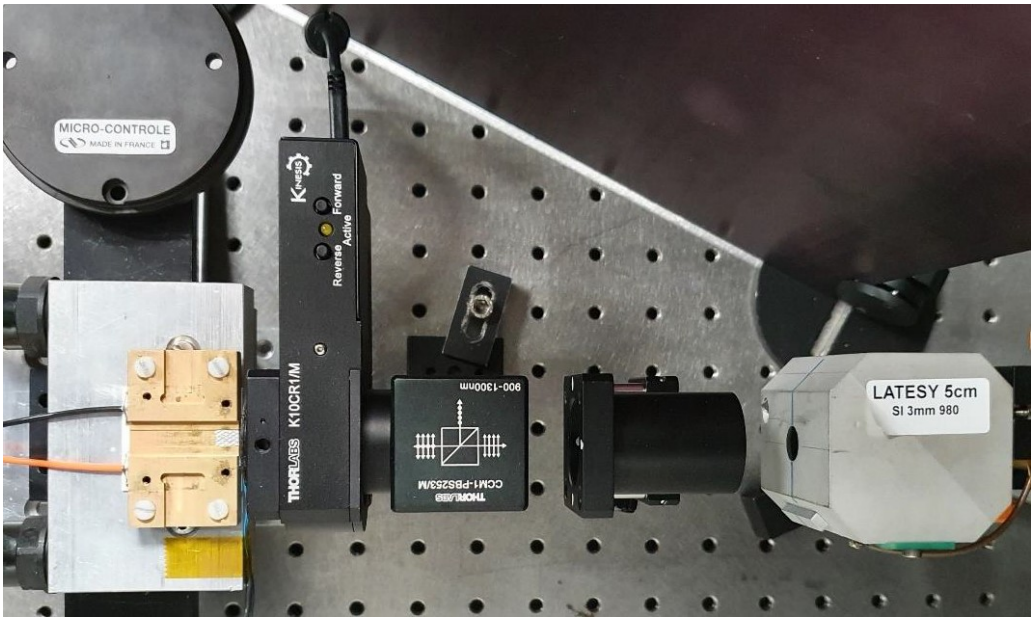

Figure 31 - Photograph from the top of the optical bench used during the DoP measurements

3.2.2 Optical components and instruments

The core optical device of the experiment is the Polarizing Beam Splitter (*PBS*, the square black box in the centre of *Figure 31*). It reflects the hitting radiation perpendicular to the crystal orientation. The LABVIEW software can set its rotation angle through an actuator directly connected to the *PBS* (the rectangular black box in the centre left of *Figure 31*.

To perform the DoP measurements the transmitted components of the polarized beam, transverse-electric (*TE*), and transverse-magnetic (*TM*) are measured separately, in order to calculate the ratio according to *Formula 3.1*.

The reflection properties of the PBS permit to separate the two components. The separated light beam components run across two different paths along the optical bench. The transmitted one continues the optical path towards other constituents of the optical bench until its revelation, while the reflected one ends the run hitting the beam stop which consists of a black panel (to absorb the radiation), properly placed beside the PBS.

The beam leaving the PBS is highly divergent and needs collimation, a very low focal lens is positioned immediately in front of the CoC support for this purpose.

Since high optical power is in play, we need to reduce it without affecting DoP for its measurement. To obtain it, a convex lens directs the beam to an integrating sphere (the black cylinder and the gray box on the right in *Figure 30*). It is a hollow sphere with only an opening through which the optical beam comes in, the internal surface is covered with a reflective coating, in this way the incident light spreads throughout the cavity until it gets out. At the exit of the integrating sphere, there is a Germanium photodiode acting as a detector, it allows a current proportionate to the optical power of the incident beam.

The LABVIEW software monitors or manages all measurements and conditions, results are automatically saved on a separate server.

3.3 Experimental Procedure

It is important to carefully follow the procedural steps for the measurement in order to prevent damages or unreliable measures. To grant the correct thermal

conditions the first step requires activating the cooling devices: turn on the compressor and open the water flow valves, it will start the refrigerator, and then turn on the thermal controller.

Having set the right thermal conditions, we can start positioning the devices for measurement. Depending on the measured device, different turrets and hence different procedures, are used:

- *Bars*: the bar is positioned on the indium foil; then, with the help of an optical microscope, three conduction needles, directly connected to the current source, are put in contact with it.
- *CoCs*: after setting it on the indium foil, an insulating support with eight conductive needles is positioned over the CoC by using four screws; the current will flow through the eight needles.
- *HSs*: with the help of a tweezer, the CoC is positioned on a support, and a plate with two tips is leaned above the HS; we must ensure that the tips are in perfect contact with the carrier terminals. The turret is designed in order to allow the measurement of the three diodes mounted on the heat sink without disassembling the plate each time.

Once the connection is done, using the LABVIEW software, a low current (about $1A$) is delivered to the device. This produces a low-energy beam used to regulate the collimation. By using a strip of paper (in order to be able to see the infrared beam) and by rotating the micrometric screws on the turret, the beam is regulated in order to guarantee its collimation and entering the integrating sphere. The last test before starting the measurement is about the *PBS*, we control if it works properly rotating it 90° in one direction, then rotating back again, using the LABVIEW software.

All preparations and checks are done, and the measurement can start. The current, in the allowed range (usually $1\ A \div 12\ A$), is selected and the program can start to make measures of the optical power at regular values of current.

Emitted light goes through the PBS which has the separation plane for the two polarizations inclined by $45°C$ cross to the optical beam propagation plane. So, *TE* polarized component is transmitted, while *TM* polarized component is reflected, and we can measure the optical power for the *TE* polarization.

At the end of this step, by rotating the *PBS*, it is possible to switch the transmitted light component with the reflected one. Now the power of the *TM* polarized radiation is measured. The software automatically computes the DoP and saves the result in Prima Electro servers.

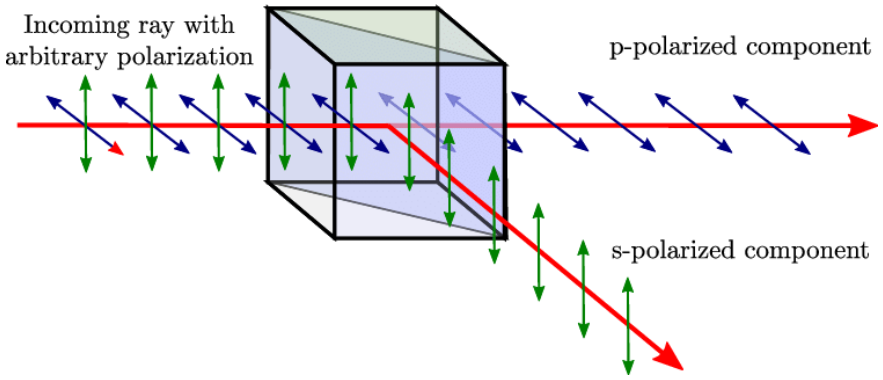

Figure 33 - Schematic representation of a Polarizing Beam Splitter (PBS) used in the measurements of the DOP, in order to separate and measure individually the polarized components of the optical beam.

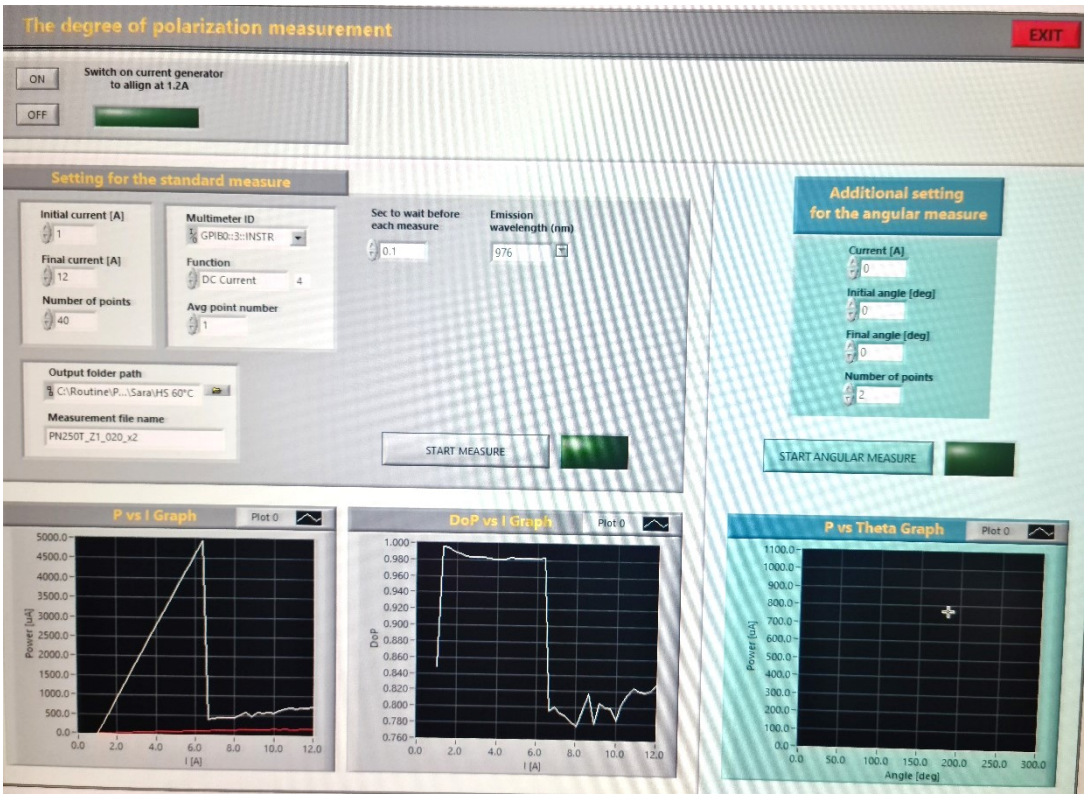

Figure 32 - Example DoP acquisition

4 Assembly processes

4.1 Diode Realization

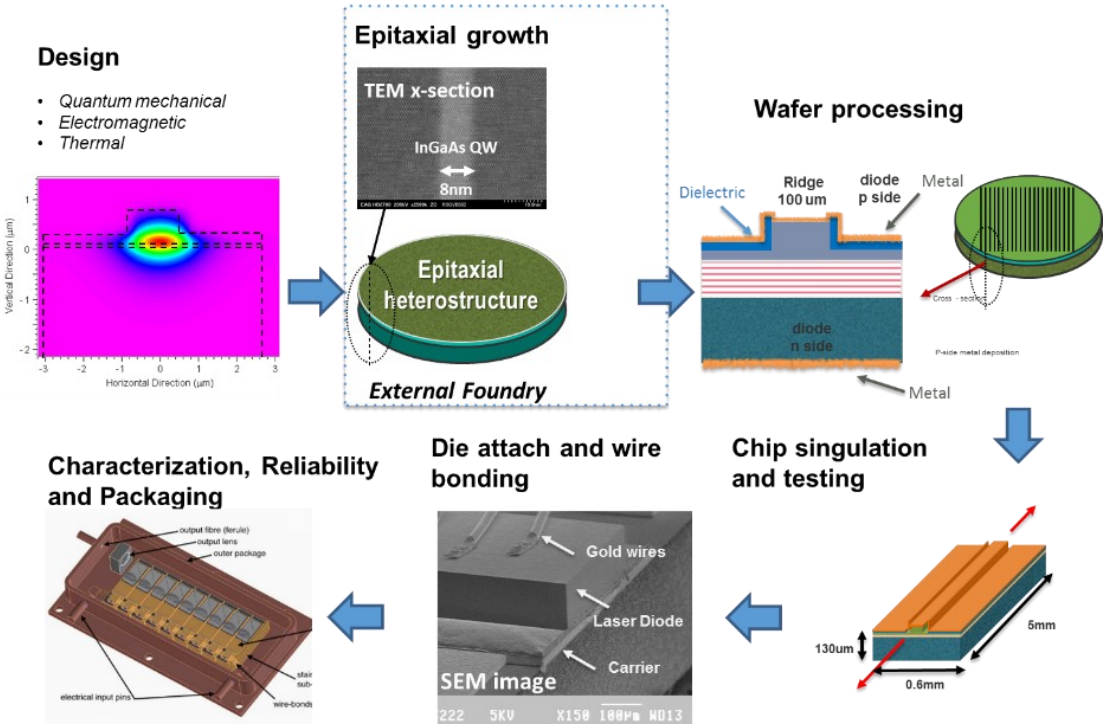

Figure 34 - Diode realization process scheme

The diode is designed to have the desired optical and electrical features. The most suitable materials must be identified and the heterostructure profile must be studied. Once it is ensured that the required properties are satisfied with the chosen design and materials, the wafer growth is started. The wafer is then processed with lithography and chemical etch in order to define its geometrical profile and with physical deposition of appropriate dielectric and metals thin films for insulation and contact. At the end of this process, diodes are separated and optical coatings are deposited on their facets. From a wafer, thousands of chips are produced and then they will be tested one by one with automatic characterization systems to guarantee that the required performances are reached. Now each diode is a finite object able to emit light but, to be utilized it needs to be soldered on a support (carrier) which guarantees strength and heat dissipation. The diode will then be bonded (n side) to the carrier with a gold wire.

Eventually, the completed diodes are mounted on a structure called multi-emitter that has the function of combining the emitted beams of several chips in order to reach an emission power of hundreds of watts.

Once the mounting process is finalized, one realizes that emitted power decreases compared to the expectation and the quality of the beam worsens. This problem was faced up by analysing the results of the measures and with the support of the literature.

4.2 Clean Room and Precautions

Every production process, from wafers production to diodes mounting, is carried out inside a clean room.

A Clean Room is a closed, contamination-controlled environment that protects processes from impurities, ensuring maximum cleanliness. The air inside is filtered in order to have very low levels of suspended micro-particles. Temperature, humidity and pressure levels are kept under constant control so that processes and operations that require a contamination-controlled environment can be carried on under stable conditions.

Clean rooms must conform to some structural requirements:

- materials must not release particles;
- surfaces must be smooth and easy to clean;
- joints must have rounded edges;
- sockets and frames must be flush;
- pipes must pass outside the room.

The production process itself, together with the machinery, represents one of the main sources of contamination inside a clean room. Particular attention must in fact be paid when moving the products and when cleaning and maintaining the clean room. Also, operators can emit millions of particles that are a hazard for a sterile environment.

In addition to being accurately professional, workers entering a clean room must in fact wear sterilized or disposable clothing following a precise sequence. Firstly, shoes must be changed or overshoes must be worn, then the hair must be collected in a headset, and a boilersuit must be worn together with disposable gloves and mask. This

dressing procedure must be carried out in a changing room located close to the Clean Room to avoid external contamination.

Operators handling electronic devices like diodes need to wear an electrostatic discharge device (ESD) to prevent electrostatic, which can damage electronic components.

Full compliance with the required standards guarantees sterile production.

The reference guideline for clean rooms is standard UNI EN 14644. Clean Rooms can be classified using ISO Class 1 to 9, which states the maximum permitted concentrations of suspended particles, those between 0.1 to 5 microns in size, per cubic meter of air. Depending on particle value, it is possible to classify a clean room starting from ISO 1, which represents the cleaner (max 2 particles of 0.2um per cubic meter), to ISO 9.

Clean Rooms used for electronic devices are usually classified from ISO7 (max 352,000 particles of 0.5 um per cubic meter) down to ISO1, depending on the type of devices produced. [16]

Figure 35 - A clean room of Prima Electro's laboratories, where wafers are processed

4.3 WaferFab and DiodeFab

The diode realization starts with the wafer production followed by the separation in single chips.

The fabrication process starts with the epitaxial growth of active layers on a substrate. The first step executed in Prima Electro clean rooms is the ridge (waveguide) fabrication that consists of photolithography and wet/dry etching. Then a dielectric layer is deposited with PECVD (Plasma-enhanced chemical vapor deposition) process. Afterwards photolithography is used again to open a contact window on the ridge removing the dielectric material in a specific area. For the p-side metal coating, metal is vaporized all over the wafer then, lift-off lithography removes the excesses. Finally, after the wafer thinning and a cleaning process, the metal n-side is deposited using again a metal evaporator.

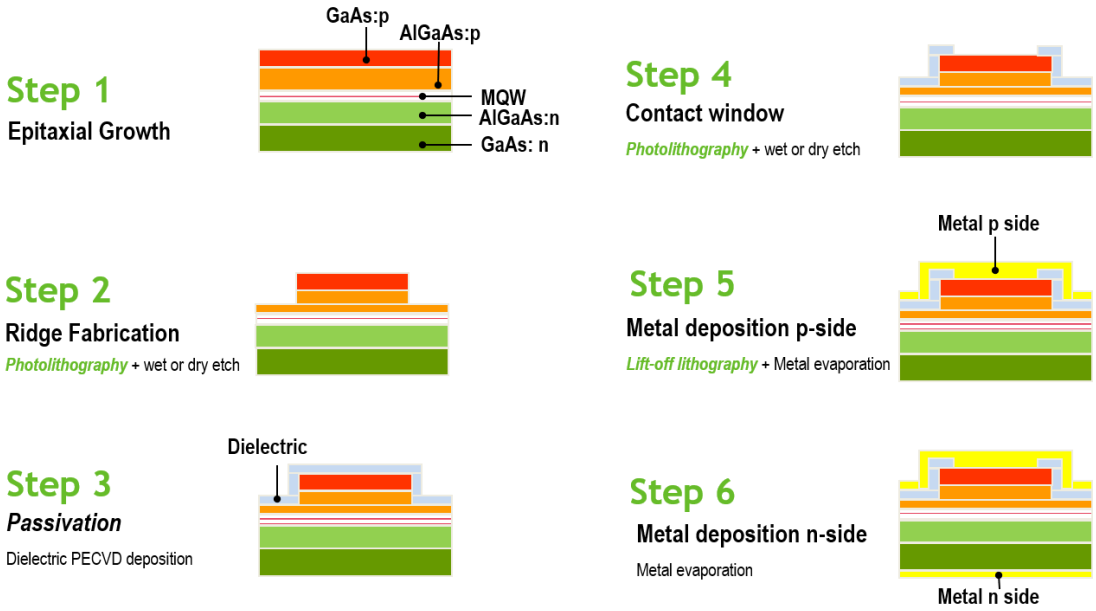

Figure 36 - Wafer fabrication steps process

Once the wafer fabrication process is completed it is ready to be cleaved into single diodes.

The diode fabrication is divided in 4 main steps: scribing, coating, dicing and visual.

4.3.1 Scribing

The wafer (which diameter is about 10 cm) is firstly divided in four pieces along the ridge direction (which length is about 2 cm, to be compatible with the evaporator width) which in turn are split into bars. Every bar is composed of 33 diodes, 30 of which are exploitable while 3 are the markers located every 10 diodes.

Every diode is assigned a code for identification, the number of the process, the number of the bar and the relative number of the diode compose the code.

For instance, the code of a diode could be PN250T_Z1_009_052, where PN means that we are considering a diode from the production, T refers to the treatment on the material before the deposition of the antireflective and high reflective coating, Z is the following run in the coating. The last two numbers are the number of the bar and the number of the diode inside the bar respectively.

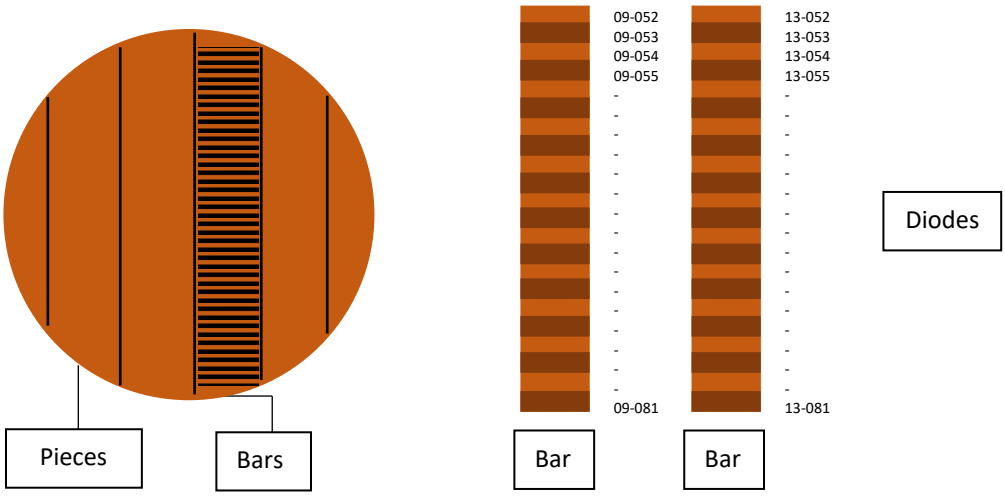

Figure 37 - Rappresentation of the diodes on the wafer

4.3.2 Coating

The cleaved bars are loaded into a dielectric deposition reactor by a specific tool. The antireflective and high reflective coatings on diode facets are performed in two different depositions. Typically, different combinations of thin aluminium, Silicon dioxide and Titanium oxide layers produce the appropriate reflectivity. After all these processes the diode can emit light with the right wavelength and power, usually above ten Watts.

4.3.3 Dicing

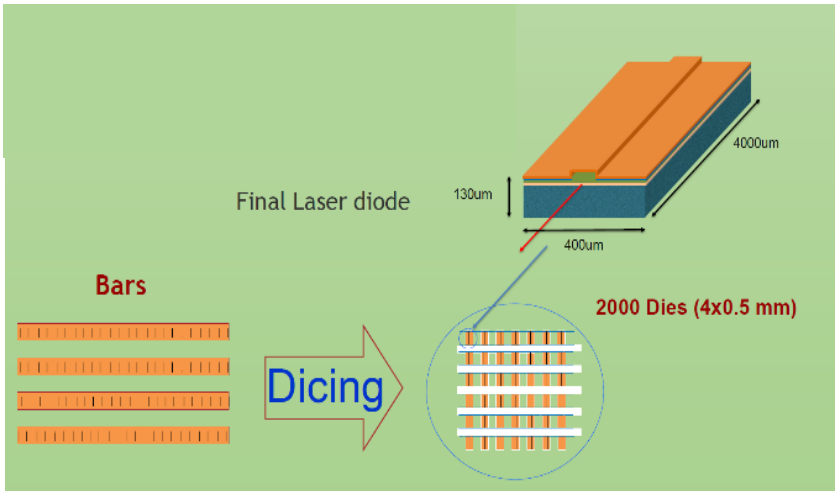

Figure 38 - Schematic representation of the dicing process

It is the step in which bars are separated into single diodes. The process is pursued under ionized air to avoid electric charges burn the bars. Bars are attached on a specific tape trapped between two rings.

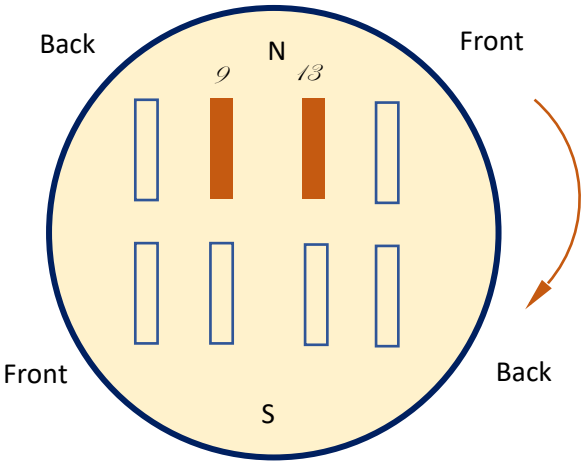

Figure 39 - Representation of the tape where bars are displaced for the dicing

Bars are then cleaved into diodes using an automatic machine based on the exploitation of the crystalline structure. Crystal anisotropy of the III-V compounds makes it possible to achieve mirror-like surfaces over a length of several centimeters.

A diamond cutter scratches the surface across and along the wafer with enough pressure, the crack extends for several micrometers inside the substrate. The wafer is then broken at the cracks by applying pressure to its back side. [17]

However, when performing cleavage on large surfaces, problems may occur, and defects can be generated. The main factors that can influence the success of the process are:

- poor accuracy of the identity markers;
- misalignment between the mask and the wafer during the lithography processes;
- misalignment during the cleaving process;
- superstructure-induced stress.

While the first three factors can be reduced and controlled as they only depend on how those processes are performed, the last factor, on the other hand, is not controllable and strictly depends on the recreated geometry and on the intrinsic characteristics of each wafer structure (e.g. the presence of defects). It has been statistically estimated over the years that the drift in one direction from the starting line is around 20 µm for a 20 mm cleaving length.

Heating the tape at 60°C on a hot plate causes its expansion and consequently diodes separate from each other.
Applying UV light, the tape hardens and the adhesion of diodes on it is reduced.
In the end, diodes are carefully transferred to the gel pack where they are kept until further processing.

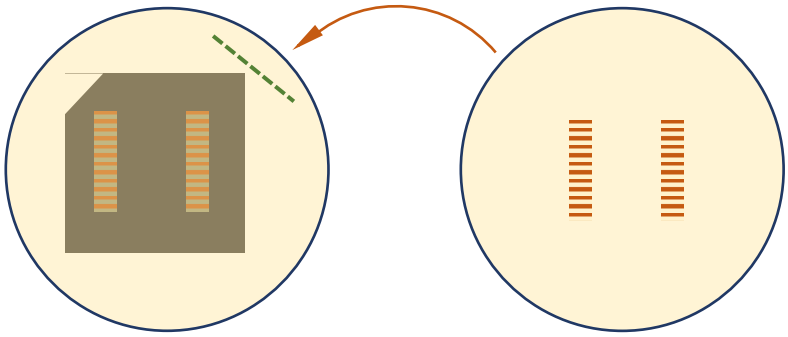

Figure 40 - Representation of the diode separation

4.3.4 Visual

An optical microscope is used to inspect the facets and the ridge. Some of the defects that must be detected are (*Figure 41*):

- Broken corner or side
- Dirty
- Metal on the ridge

If marks bigger than 5 µm are checked the device is tagged as “fail”, which means that it will be discarded because can’t be used.

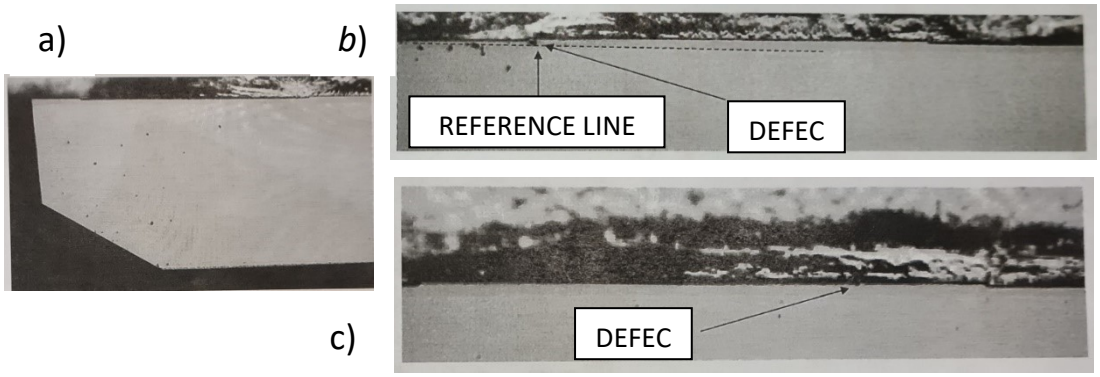

Figure 41 - Images of defects: a) Broken corner. b) Dirty. c) Metal on the ridge.

4.4 Chip On Carrier Assembly

The laser diode produced in the described process cannot be used without a proper assembly. In fact, in this state it presents some critical issues like the application of electrical contacts directly on the diode metallization: they are too weak to bear the current, over 10 A, which flows into the wires. Another problem relates to the temperature that the device reaches during operation. The current injected into the diode increases the temperature because of the Joule effect, moreover, any defects and impurities presented into the crystal and into the emitting facet could be radiative recombination centres which take part in the device's local temperature rising.

4.4.1 The Carrier

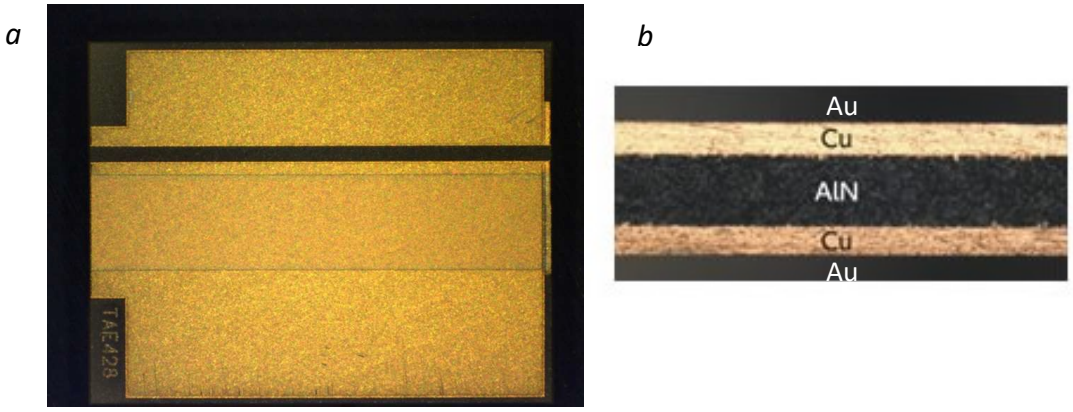

Figure 42 - a) Carrier top view seen from the microscope. b) Carrier cross section.

To solve these issues the diode is soldered on a carrier in order to maximize the heat dissipation and ensure the electrical contacts on it. This structure is made by aluminium nitride (AlN) a ceramic material with high thermal conductivity (around 180 W/mK), that allows to dissipate the heat generated by the chip. [18]

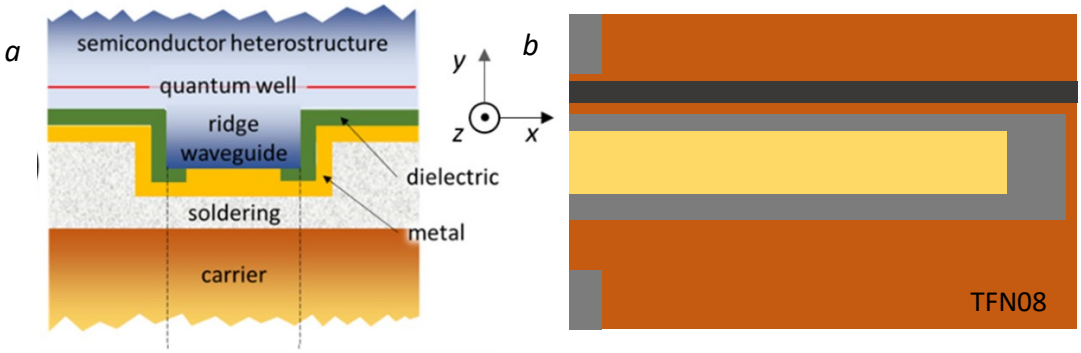

Figure 43 - a) Representation of the CoC soldering b) Representation of a top view CoC. The carrier has a code at the bottom (i.e. TNF088), and has a length of 4mm.

The electrical contact on the *n-doped side* of the diode is made by gold wires, with diameters of 35 μm, which are soldered on the diode and on the according side of the carrier.

An automatic machine (*WestBond 3700E*) melts a side of the wire generating a gold drop that sticks on the diode. Then the machine welds the other extremity of the wire on the carrier.

The electrical contact on the *p-doped side* of the diode is instead obtained by soldering the chip on the carrier. The carrier top layer is made of an Au-Sn alloy, the diode is

placed upside down n the carrier, with the gold metallization in contact with the Au-Sn alloy. At this point, a machine is used to start a ramp temperature. In this work two different machines have been used and we will investigate the differences in the diodes properties due to the two different assembly processes. We name the machines *Lambda* (manual) and *Femto2* (automatized).

Lambda

Figure 44 - Example of the temperature ramp used during the CoC assembly process by the Lambda machine. The darker line represents the theoretical ramp while the lighter line represents the ramp performed by the machine in real time

As reported in the manual of the machine, the temperature increases of $\sim 200°C$ and is kept at the top level for a few tens of seconds. Then it decreases down to the starting value that maintains for about a minute.

Femto2

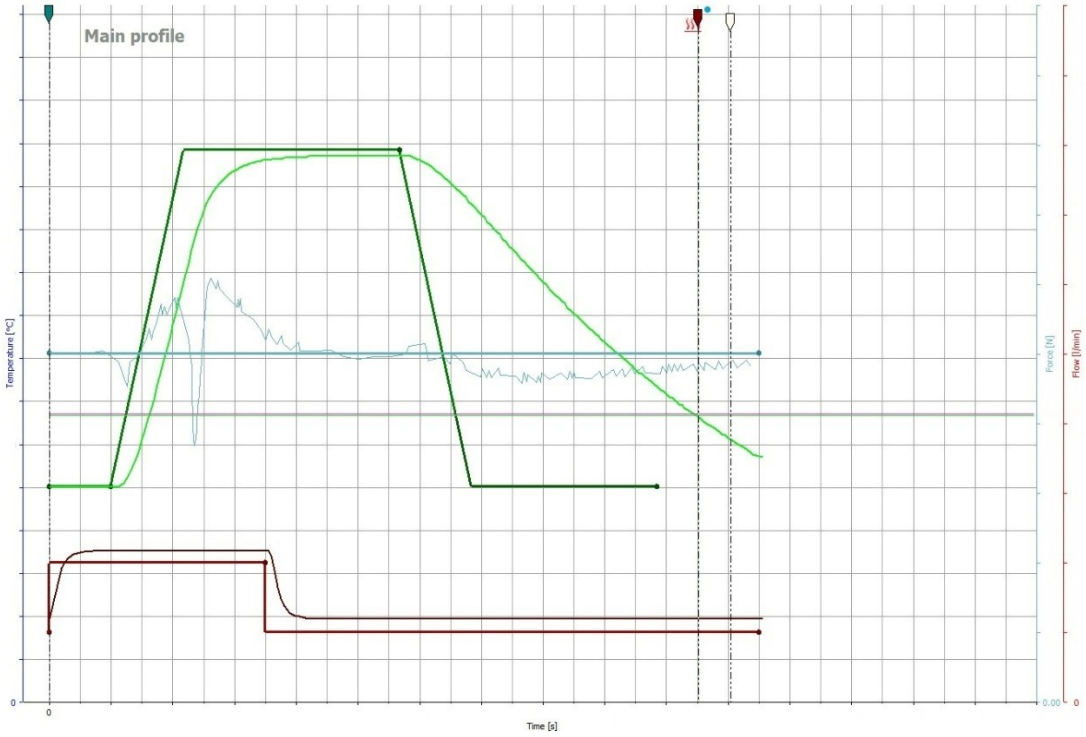

Figure 45 - Example of the temperature ramp used during the CoC assembly process by the Femto2 machine. The darker green line represents the theoretical ramp while the lighter one represents the ramp performed by the machine in real time. Below, in red, there is the representation of the forming gas flow both theoretical and real.

The *Femto2* temperature ramp is different from the *Lambda* one, being two different machines, which work differently. A fundamental aspect, beside the temperature ramp, is the force used by the machine during the soldering, outlined by the blue line in the figure above. The control of this force is the forefront outcome shown later it this work.

Once the maximum temperature is reached the melting process is triggered. A forming gas flow, containing hydrogen (H_2) and nitrogen (N_2), is commonly applied during the die attach. The forming gas can help in preventing solder oxidation at the normal process temperature that ranges up to $300^{\circ}C$. [19] The Au-Sn alloy of the carrier melts down together with the gold of the diode forming a single layer that once cooled down guarantees the soldering of the device on the carrier.

Current can flow from the diode through the soldering, along the Au-Sn layer, and then through the positive connector of the carrier.
During the welding process just explained, the laser diode is submitted to thermal and mechanical stresses which cause the deterioration of the proprieties.

4.4.2 Lambda

Figure 46 - The machine Lambda with its components

Before starting the welding procedure, one must verify that the mounted tool is the correct one to assemble the Chip on Carriers and the heating plate is mounted.
The force that the machine employs to press the diode on the carrier must be set at $1{,}5\ N$.
The machine is controlled by the PC using the software WinFlipChip. We must select the Au-Sn process.

The procedure provides the following points:

- The carriers are placed in a black box with a cut angle that should be placed on the top right.

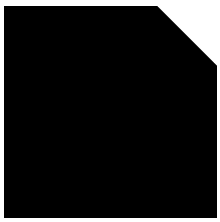

Figure 47 - Carrier box

- The carrier must be placed on the heating plate with a vacuum pipette. The right position is centred on the cross with the front facet oriented on the left.
- From the PC runs the vacuum to hold the sample.
- The gel pack with the chips must be inserted in the appropriate location, in this case the cut angle should be placed on the top left, then the vacuum must be activated on it so that the chips can be picked up with the pick-up tool.

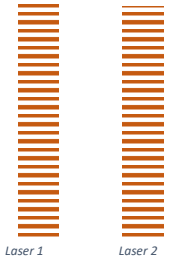

Figure 48 - Representation of the bars placed in the gel pack

- Lights and contrasts must be set so that the pick-up-tool is clearly visible by adjusting the Head Lamp and the Target Lamp on the right of the main screen.
- Pressing the right pedal, you can move the plate so that the camera sees the chips on the gel pack.
- Focus the chips with the grip that adjusts the movement in *z* on the right of the plate.
- With the help of the laser pointer, position the camera on the chosen chip and move the plate so that the pick-up-tool is aligned (also roughly) with the chip.

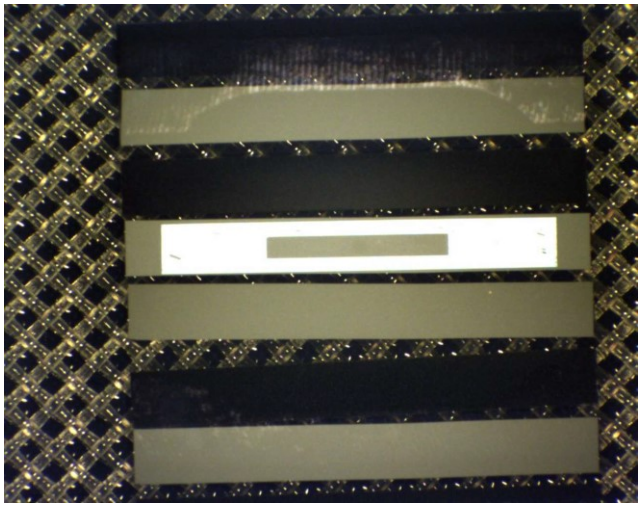

Figure 49 - Alignment of the pick-up-tool with the chip

- After the rough alignment, refine the alignment of the pick-up-tool with the chip by means of the grips that adjust the shift in *x*, *y* and rotation.
- After alignment, move the camera to the right so that you can lower the pickup-lever tool to pick up the chip.
- Lower the right lever and remove the vacuum from the pick-up-tool by pressing the left pedal.
- Gently lower the left lever, widely more precise, until the pick-up-tool is almost in contact with the surface of the chip.
- Make the vacuum on the pick-up tool by pressing the left pedal to pick up the chip.
- Once you have taken the chip, first raise the left lever and then the right lever.
- Move the camera to the left and verify that the chip you picked up is the right one (the number chip identifier you will see reversed).
- As we have already done to pick-up the chip, the chip must be aligned on the carrier.
- The chip must protrude from the carrier of 5 μm
- After alignment, move the camera to the right so that it is possible to lower the pickup-levers tool to connect the chip on the carrier.
- Lower the right lever and then gently lower the left lever to the bottoming out.
- Press the PLAY button to start the heating ramp.

- Check that the temperature follows the set ramp.
- At the end of the temperature ramp, wait for the forming gas flow for cooling to be finished.
- Press the left pedal to release the vacuum from the pick-up-tool and lift the left lever first then the one on the right.
- Move the camera to the left and verify that the chip is aligned.

4.4.3 Femto2

Figure 50 - The external view of the machine Femto2

It is a fully automatic die-attach machine that offers superlative flexibility for prototyping and production environments being fully protected from external influences.

To produce the samples for this work the machine was employed in semi-automatic mode, because of not working of the machine previously used in the production process to do the visual step.

By using *Lambda* similar modules and tools, process transfer costs are reduced. In addition, thanks to the modular platform architecture, a wide range of bonding technologies and processes can be easily converted, expanded, and replaced.

The software is identical across all systems, with the only difference being that the production systems have extended capabilities for process automation compared to the manual machine. The process profiles and parameters developed during the R&D phase can hance be transferred from a manual development system (such as *Lambda*) to a fully automated platform (e.g. *Femto2*). For production purposes, they are merely enhanced with automatic handling steps.

Although the machine is automatic is expected to be constantly observed by an operator. The procedure provides the following points:

- The box with carriers must be placed in the appropriate location on the right.
- The gel pack with the chips must be inserted on the left.
- The recipe "*Leica PN*" must be selected on the screen.
- Choose from which diode the process should starts.
- Now we must teach the machine how to pick up the chip:
  - Focus the chip manually.
  - Choose the carrier on which the chip must be mounted.
  - With the help of the grips, the chip must be aligned with the shape of the tool.
  - Press the button to pick-up the chip
  - Control that the chip kept is the right one.
  - Press the button to make start the temperature ramp.
  - Once the soldering is finished, choose the box and the place where the chip must be settled.
- Now the machine works automatically on the next chips to weld. In the semi-automatic mode, the operator must stop the machine when there is a *fail* chip that has not to be soldered.

4.5 Bonder WestBond 3700E

The diodes need to be bonded to the carrier with wire bondings in order to let the current pass. This procedure is not easy and needs a lot of accuracy and precision.

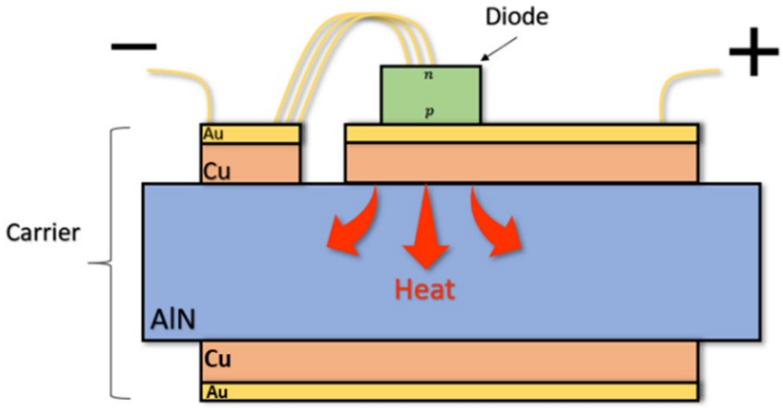

Figure 51 - Schematic of a chip mounted on a carrier with bondings

The WestBond 3700E is an automatic machine interfaced to the PC, which provides the installation of electrical connections (wire bonding) on the chip on carrier.

Figure 52 - External view of the WestBond 3700E

- Firstly, the machine must be powered up and the PC turned on.
- Turn on the power supply of the heated sample plate, and make sure that the temperature stabilizes to $125°C$ (after about 10 minutes from ignition).
- Turn on the ionizer.
- Launch the machine management software. Make sure the loaded recipe is the one indicated for the material you are working on.
- Load a test sample.
- Calibrate the movements of the bonding head manually by means of the software.
    - The head goes down towards the CoC and makes a bonding leaving a "*ball*" on the CoC.
    - Check that there is actually the ball, and at the same time, as the electrode descends towards the capillary, that there is an electric discharge between its tip and the electrode.
    - Check the presence of the new ball so formed on the tip of the capillary through the microscope.
    - The machine is now ready for carrying out the wire bonding on CoCs.
- Loading the CoCs to be worked on the heated plate following the order of the number written beside the throughs using the vacuum pipette.
- The carrier must be positioned with the front facing the right making it adhere to the edges of the trough.

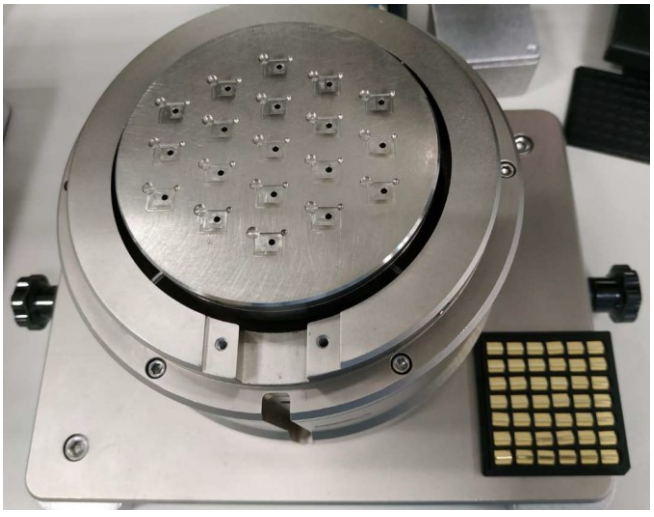

Figure 53 - Representation of the heated plate with troughs for the CoCs

- The bonding head moves on the first CoC to be bonded and automatically aligns via image recognition.
- Now the machine automatically performs the bonding on the loaded CoCs. Two 22 bonding lines will be performed on each CoC, this bonding number allows the chip to work even if not all bondings are done correctly.
- At the end of the process proceed with the unloading of the CoC.

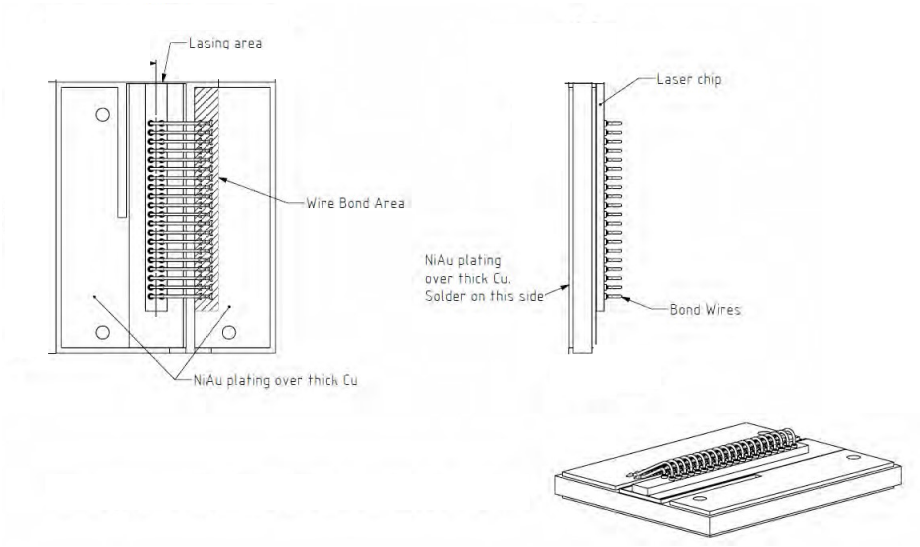

Figure 54 - Top view and lateral representation of a CoC

Chip on Carrier assembly on Heat Sink

The CoC is then soldered on a Heat Sink (HS) to simulate the packaging as it would be too bulky to be able to measure it directly. The difference between the packaging and the Heat Sink is the prevalence of Cu instead of W inside.

The machine used to solder the CoCs on the HS is the *Lambda* as the automatic machine is programmed just to solder the CoC on the multiemitter module.

In this case, we do not use a receipt to warm the sample, instead, we have a procedure to solder CoCs on the HS that involves the use of a Sn preform between the CoC and the HS. The preform is a reactive multi-layer foil fabricated of alternating nanoscale layers of Aluminum (Al) and Nickel (Ni) that provides instantaneous heat. When activated by a small pulse of local energy from electrical the foil reacts exothermically to precisely deliver localized heat up to temperatures. This mechanism was also used

for MEMS soldering by Takahiro Namazu et al. [20] and investigated by El-Mostafa Bourim [21].

We use a different tool with another shape to pick up the CoC and the plate must be substituted with one not warmed.

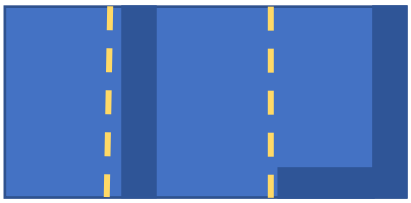

Figure 55 - Top View scheme of the tool alignment on the CoC

As the smoke spurted out from the soldering is carcinogenic it is required to use a pomp to suck it.

- The carrier is positioned so that the is facing me.
- I move the plate under the camera, and I assure that the carrier overlaps the tool.
- I remove the vacuum then I pull down the lever: the tool picks up the carrier.
- I take the Sn preform with the vacuum pipette and I put it on the HS.
- I see the HS with the Sn preform moving while the tool with the carrier is fixed.
- The force is set to 20 N, to fit the 2 pieces you go up and down with a lever 3 times.
- Energy is given off from the preform. I connect the blue wire (negative) on the ground (on the HS while the metal wire (positive) on the Sn preform. Pressing the pedal and creating an electrical arch the circuit will be closed.
- Once the sample is obtained, the name of the sample is written on the back with the permanent marker.

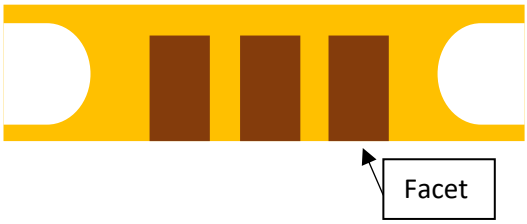

Figure 56 – Representation od CoC mounted on a Heat Sink

5 Diode deformation

We have already seen that the performance of semiconductor lasers is considerably affected by the properties of packaging materials, which mainly consist of different bonding solders or mounting substrates. [22] [23]

This thesis mainly concerns the analysis of DoP using different procedures. Observing the macroscopic deformation of the chips, caused by soldering, it is possible to use the data collected in the experiments to obtain information about its relationship with the relative DoP.

5.1 Au-Sn Alloy

The Tin-Gold (AuSn) solder has been successfully used for highly reliable die attach in the packaging process of high-power semiconductor lasers and for high-quality bonding. AuSn solder has good thermal and electrical conductivity, high corrosion resistance and high melting temperature.

In general, the AuSn alloy is commonly used at the eutectic as it is a robust solder with a composition of AuSn at or close to the eutectic point with 80 wt% gold and 20 wt%. The main physical properties of 80 wt%Au20 wt%Sn are shown in *Table 1.* [6]

Figure 57 shows the schematic diagram of the stress-strain curve for AuSn alloy [24]

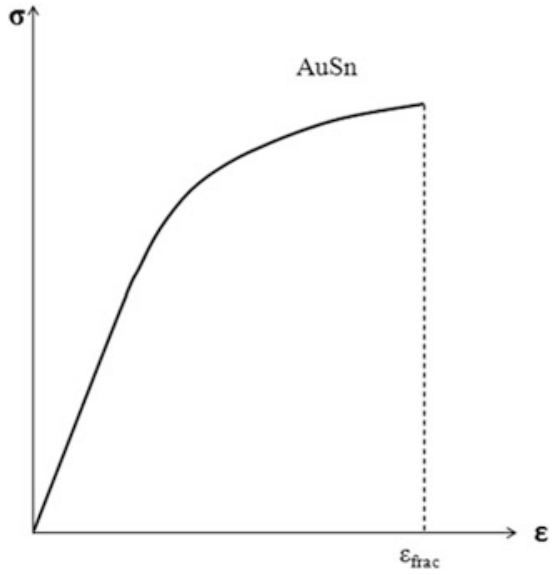

Figure 57 - Schematic diagram of stress–strain curve for AuSn alloy [24]

AuSn solder has high strength and does not undergo stress relaxation at room temperature. This could be the reason why the DoP grows with the temperature. As a consequence, the AuSn solder layer may transmit more stress to the laser chip and may even provoke cracks in laser chips. The high temperature required for AuSn die attachment would also aggravate stress when cooling assemblies.

Figure 58 shows the AuSn equilibrium phase diagram. It contains four different stable intermetallic compounds between Au and Sn at room temperature: Au5Sn, AuSn, AuSn2, and AuSn4. Among them, there is the eutectic 80 wt%Au and 20 wt%Sn composition with a melting point of $280°C$.

According to the phase diagram, the Au80Sn20 has an eutectic ξ-Au5Sn + δ-AuSn microstructure at room temperature. Experimentally, the microstructure of the AuSn eutectic alloy is comprised of ξ and ξ0-Au5Sn dendrites surrounded by the matrix of the AuSn eutectic structure (ξ + δ). ξ0-Au5Sn is the lower temperature phase while the ξ phase is stable at higher temperatures. [6]

The phase diagram of this binary alloy is shown below in *Figure 58*.

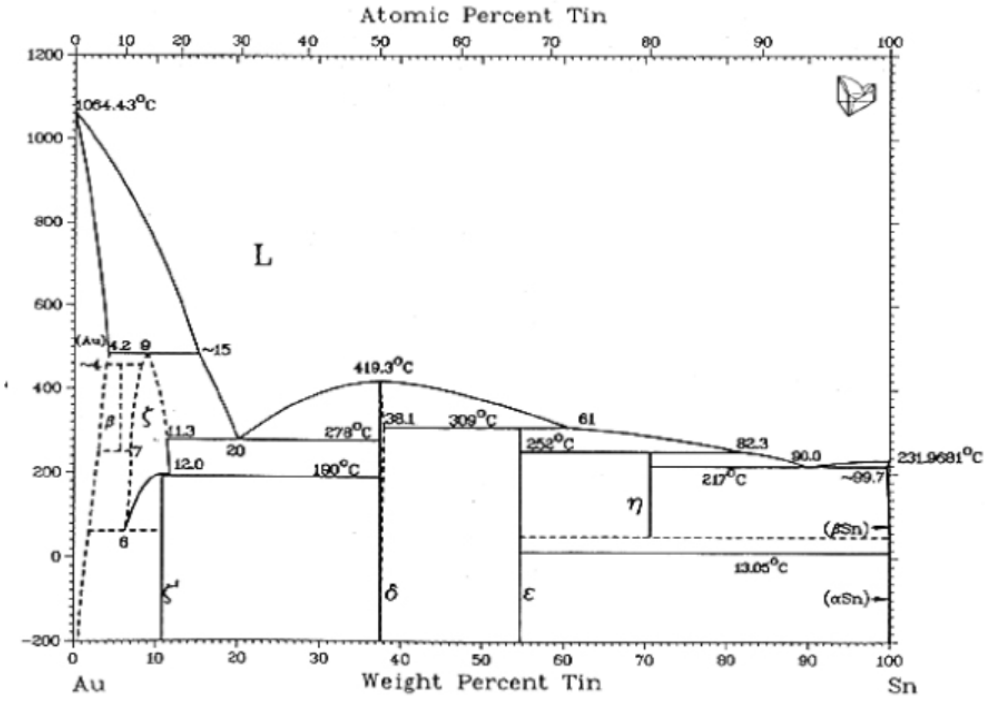

Figure 58 - Au-Sn Phase Diagram. The eutectic alloy is at 20wt% of tin with a melting temperature of 278 °C

The mechanical and physical properties of Au80Sn20 are shown in *Table 1*.

Properties of eutectic Au80Sn20	
Density at 20°C	14,7 g/cm³ [11]
Thermal Expansion Coefficient at 20°C	16 µm/K [11]
Melting Point	280 °C
Thermal Conductivity	58 W/(m·K) [11]
Tensile strength (20°C)	275 MPa
Elastic Modulus at 20°C	68 GPa [11]
Poisson's at 20°C	0,405 [11]
Shear Modulus	25 GPa [11]
Electrical Resistance	16 nΩ m

Table 1 - Properties of eutectic Au80Sn20

The advantage of this composite is its very low degree of oxidation, due to the high gold content. The alloy is available as solder preform. It can also be deposited using Physical Vapour Deposition (PVD).

Interdiffusion between gold and tin readily takes place at room temperature. The gold diffuses into the tin using the interstitial mechanism, whereas tin diffuses into gold by way of the slower substitutional (vacancy) mechanism.

Studies show that the ζ-phase of gold-tin has a lower micro hardness than the eutectic AuSn composition. Therefore, the solder and contact layers need to be arranged so that a higher amount of gold can create the ζ-phase during the packaging process. In general, the eutectic gold-tin solder is brittle, especially if compared to the ductile solder indium. [25]

The study of the crystalline phases that are formed during welding was not pursued in this thesis, but it will certainly be the subject of future analysis, to understand the causes of microscopic stresses within the crystal lattice and the possible correlation with the lowering of the DoP of the laser beam.

5.2 Interferometric Microscopy

As has already been examined by Anne-Claire Pliska [22] and other researchers [26] [27] [28] , thermal stresses are often the main cause of chip deformation.

As our diode lasers are packaged p-side down and the devices generate heat that needs to be removed. Heat picks are experienced in high-power diode lasers in the process of bonding the chip down and strain due to the difference in thermal expansion coefficients of the laser, solder, and carrier is induced in the material. The strain has been demonstrated to produce many effects in diode lasers for instance it can cause *TE-TM-mode* switching in diode lasers. In the case of strain due to die bonding it is nonuniformited so it is really difficult to predict a simple model to describe it. A first investigation into the correlation between chip deformation and DoP variation was carried out by Mark A. Fritz and Daniel T. Cassidy, it was taken as the starting point for our research. They used the DoP measurements of a diode laser facet to predict the photoelastic effect in the material. [12]

What we are going to investigate, instead, in this chapter is how this deformation can be characterised on chips and how it can be used as a benchmark.

The purpose of the analysis is to understand if different categories (with different polarisation states and thus also different optical properties) have different types of boarding.

5.2.1 Sensofar S Neox

To characterize the macroscopic deformation of the chip an interferometric microscope has been used. The Sensofar S Neox 3D Optical Profiler was made available by the INRiM (Istituto Nazionale di Ricerca Metrologica) to perform these measurements.

To obtain high-resolution images the Sensofar S Neox combines confocal, interferometry and focus variation techniques in the same sensor head without any moving parts.

A confocal microscope uses point illumination and a pinhole in an optically conjugate plane in front of the detector. As only one point in the sample is illuminated at a time,

2D imaging requires scanning over a regular raster (i.e. a rectangular pattern of parallel scanning lines) in the specimen.

The achievable thickness of the focal plane is mostly defined by the wavelength of the light divided by the numerical aperture of the objective lens, but also by the optical properties of the specimen. These types of microscopes are particularly good for surface profiling of samples because of their thin optical sectioning.

A confocal RGB image view technique allows the user to observe nano-level details within a few microns range. The red, green and blue LEDs are sequentially pulsed and synchronized to acquire three confocal images. The result is color-coded depth information determined from the chromatic depth distortion of the microscope objective. It results a pseudo-colour topography with qualitative information of the height of the topography. The S Neox uses a high-resolution CCD sensor of up to 1360x1024 pixels.

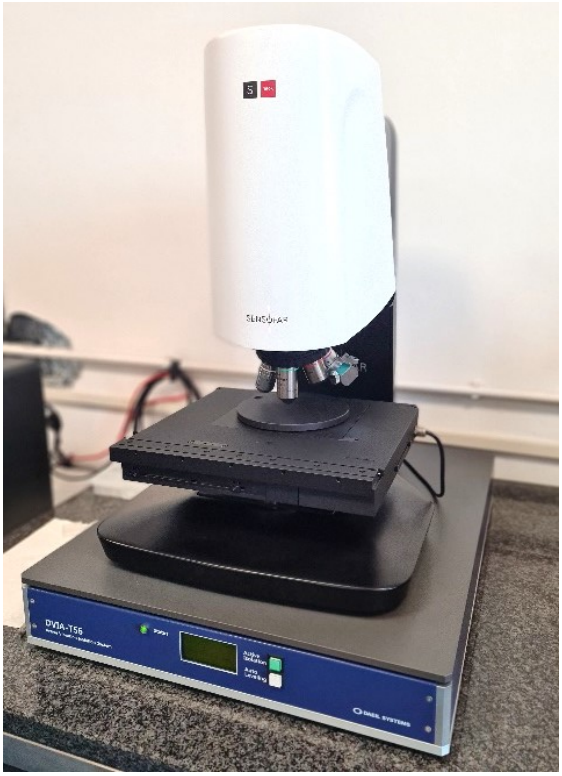

Figure 59 - INRiM Sensofar S Neox profilometer

The microscope provides two types of interferometers:

- The Phase Shift Interferometers (PSI) to measure the surface height of very smooth and continuous surfaces with sub-nanometer resolution. PSI profiling

provides sub-nanometer vertical resolution for all numerical apertures (NA). Very low magnifications (2.5X) can be employed to measure large fields of view with the same height resolution.

- White-light vertical Scanning interferometers (VSI) have been developed instead to measure the surface height of smooth to moderately rough surfaces. VSI profiling provides nanometer vertical resolution for all NAs. The VSI algorithms enable the S neox to use all the available magnifications to profile shape features with the same height resolution.

Finally, Focus Variation is an optical technology for measuring the shape of large rough surfaces. This is based on the combination of confocal and interferometric 3D measurements and is specifically designed to complement confocal measurements at low magnification. This combination of measurement capabilities is mainly used for tooling applications.

5.2.1.1 Experimental Procedure

To make measurements to the profilometer the procedure is very simple; there are only a few simple steps to follow:

- Clean the instrument with an alcohol-based solution before using it;
- Turn on the anti-vibration table;
- Turn on the instrument;
- Use the antistatic chair;
- Choose the objective you want to use, taking care not to let the objective touch the mirror on the plane on which you have the sample;
- Accurately place the sample on the profilometer plate;
- The instrument is interfaced with the computer via SensusSCAN 6.4 software. Select in the program the same lens you are using, in this case, the Nikon Epi 20x. Start the analysis.
- A joystick is used to move the sample. Turn the knob to adjust the focus on the sample.
- On the program select “Stitching”
- Set the diode analysis execution to a single line divided into seven columns

Figure 60 - *Sensofar plate where the sample is placed and the lens available by the instrument*

The program returns a two-dimensional image of the sample characterized by different shades of colours that indicate the height of the surface respect to the support surface. The data collected is saved in a text file and then processed with Matlab. The text file consists of coordinates that indicate the location of each point on the surface of the sample. The code written in Matlab allowed the display of the two-dimensional map of the chip points, similar to that returned by the program and the profiles along the two transverse directions of the chip.

Since it is not possible to be sure that the carrier has a surface perfectly parallel to the plane, it was decided to straighten the base plane by taking three distinct points of the chip and making the average of the heights in a given around, then the plane passing between these three points was calculated and used to straighten the base plane of the chip.

To find the profiles it was decided not to “cut” the chip along a certain line, because it risked running into the problem of bonding, which appears in the file as NaN (Not a Number), and for which it was created a profile making the average of the points in the opposite direction. Finally, in order to calculate the Bowing, as will be explained later, it was decided to rotate the profiles so that the two ends of the chip were at the same height, so it was easier to compare the profiles of the different chips.

5.2.2 Bruker ContourX-200 3D Optical Profilometer

In our measurements, we have had the opportunity to analyse two of the samples, previously analysed with Sensofar, with a new Bruker profilometer being tested at the Politecnico di Torino.

Figure 61 - Bruker ContourX-200 3D Optical Profilometer

This is also a profilometer with which repeatable non-contact measurements can be performed. The instrument provides surface height measurement on 3D structures with surface profiles varying between tens of nanometres and a few centimetres using innovative white light interferometry (WLI) the same technology used by Sensofar but developed in order to obtain 3D images.

With the use of multiple objectives and thanks to the sub-nanometer vertical resolution, it provides results useful for quality control and process monitoring as in the case of chip deformation.

Thanks to the free Software provided by Bruker, ProfilmOnline, it was possible to process the images obtained with the profilometer. *Figure 62* shows an example of the 2D image of the chip on the left and the 3D image of the sample on the right. Thanks to this software, it is possible to calculate the deformation directly. As the instrument

has a higher resolution, the measurements obtained will be more precise and more reliable, thus obviating instrumental error, which can also be the cause of difficult correlation of bowing data.

This section has been written for information purposes as we were only allowed to make 2 test measurements and not to carry out the analysis of an entire group of samples.

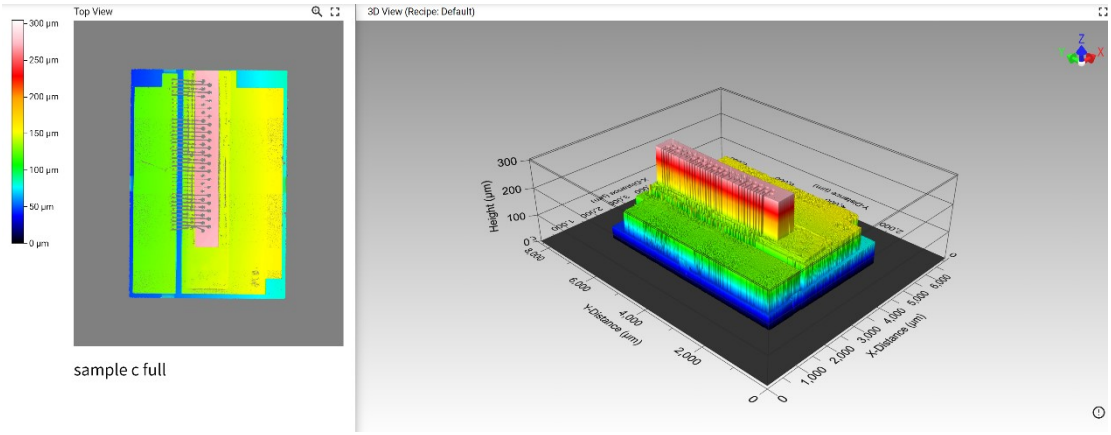

Figure 62 - 3D profile of the CoC captured by Bruker ContourX-200 3D Optical Profilometer

5.3 Bowing

To study the degree of macroscopic deformation of the chip, the Bowing was used as a measure. To determine the bowing we take the profile along the z-axis of the chip, measure the difference between the height of the points corresponding to the ends of the chip and the minimum of the curve, then divide it by the length of the chip. Bowing in both directions was calculated, but it was decided to consider only the bowing along the long side as it is of greater relevance. The reason why the value resulting from the difference between the maximum and the minimum was divided by the length of the chip is because in this way it can be considered a normalized parameter and thus comparable with other chips with similar characteristics.

During the analysis of the deformation profiles of chips produced with other types of processes, it has been observed that some of them had two minima, so it was difficult to assess this parameter as applicable to all chips. In the thesis, only those chips whose processes returned a parabola-like deformation with only one minimum were taken

into account, which is why Bowing can be considered a characteristic parameter of these profiles.

Then, as we will see later from the analysis of the data, no real correlation was found between Bowing and DoP, therefore it was supposed that the correlation was not in the degree of deformation itself but in its shape. In fact, a similarity between the profiles returned by the chips soldered with the same tools on the same machines was noticed. The profiles are shown in the data analysis chapter.

6 Data Correlations

This chapter contains the analysis of the DoP data collected measuring the behaviour of the Chip on Carrier (CoC) alone and of the CoC soldered on the Heat Sink. The statistical analysis mainly focuses on the results obtained using different machines and tools for soldering (*Femto2* machine, *Lambda* machine and *Spring Tool* on *Femto2* machine) and on results variations at different temperature conditions. For the analysis 23 samples were produced with the Femto2 machine and 29 with the *Lambda* machine. For the *Femto2* machine equipped with the *Spring Tool,* two sets of 10 samples were produced at two different temperatures. The number was limited but sufficient for statistical results, as shown in the following figures, including data analysis with statistical tests.

6.1 Data Analysis on CoC

The DoP of the CoC has been individually measured using the procedure explained above in *Chapter 3*. Then microscopic deformation measurements were performed with the interference profilometer.

6.1.1 DoP CoC for different machines

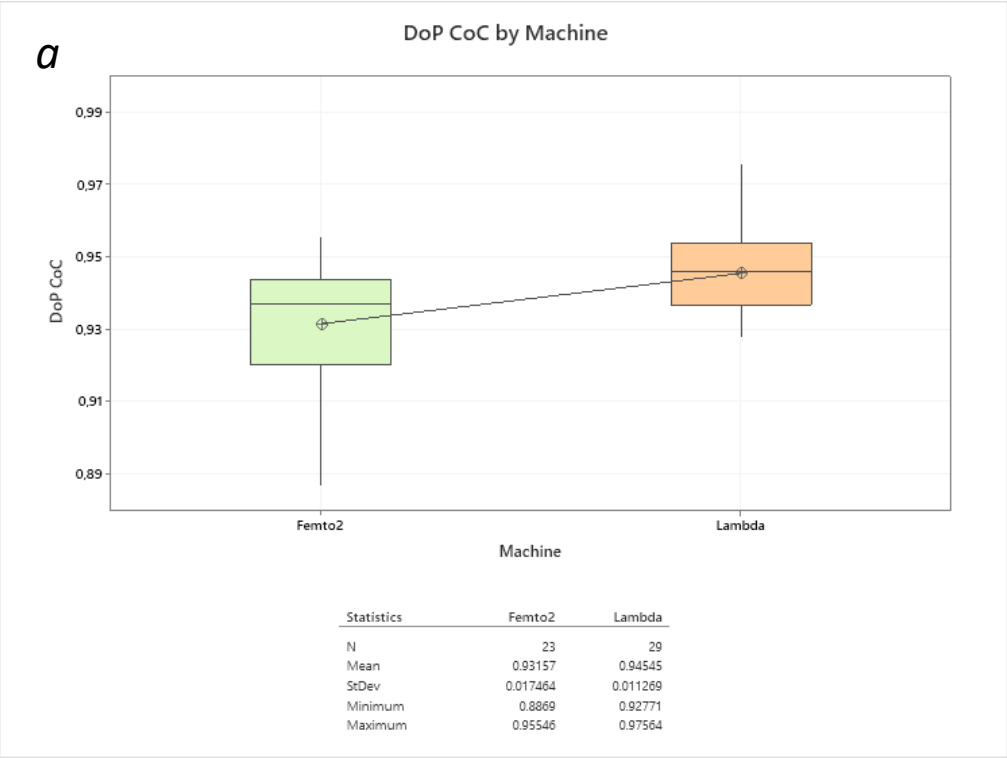

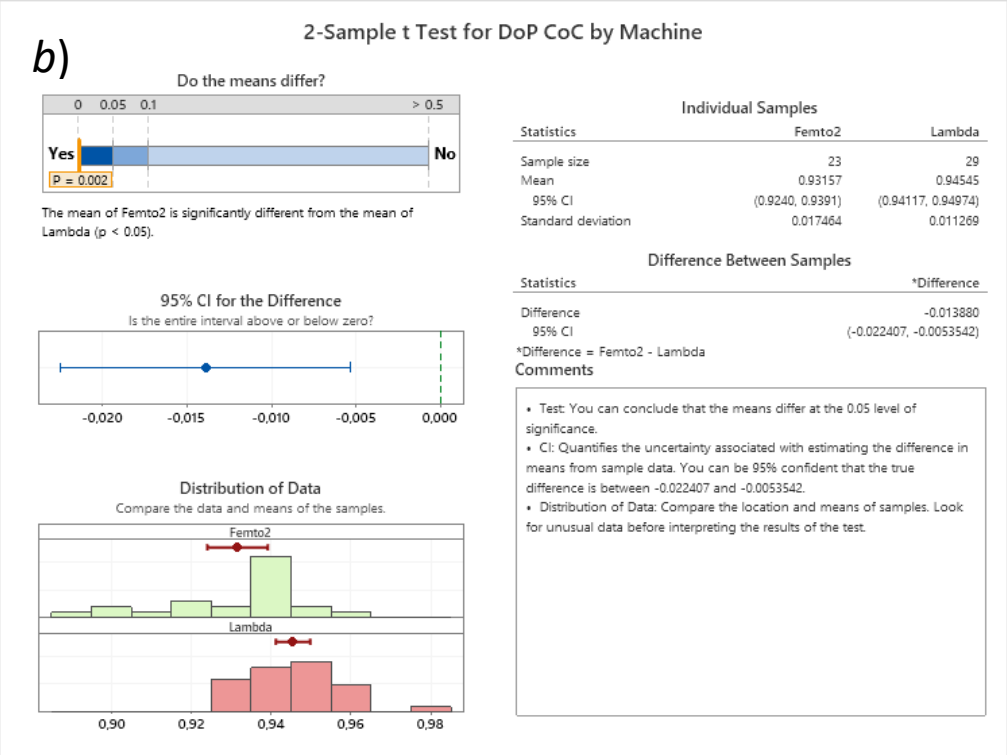

Figure 63 - a) Boxplot of CoC DoP for different machines b) Statistical analysis of CoC DoP

Data demonstrate that there is statistical evidence of differences between the two distributions: under the same conditions (process type, carrier lot), the DoP of the CoC soldered with the *Lambda* machine is always greater than the DOP of the CoC soldered with the *Femto2* machine with an average difference of about 1.4% within a 95% confidence interval.

As seen before, the *Lambda* process is a manual one, which means that it is not suitable for large-scale industrial production of laser diodes. However, since it allows for better performance in terms of DoP, trying to apply some of its characteristics to improve the *Femto2* process can be of great interest; that is why comparative studies of these characteristics have been carried out. In particular, temperature and force applied in the process are the two main parameters studied.

The bonding tools mounted on the soldering machines and the machines themselves affect the application of the force during the bonding phase.

The *Lambda* is a manual machine while the *Femto2* is an automatic motorized one. Evidence shows that the automated machine allows for less control on the applied force in correspondence to the fusion temperature of the solder. In more detail, there is an important variation of the applied force, both in intensity and in direction, as shown in *Figure 64*.

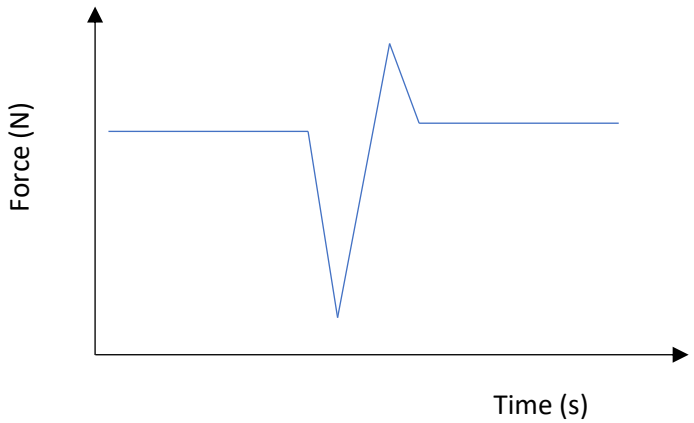

Figure 64 - Schematic graph of Femto2 force as a function of time. There is a spike in correspondence of the fusion temperature of solder.

This fast-changing force has a negative influence on the stress induced in die attach.

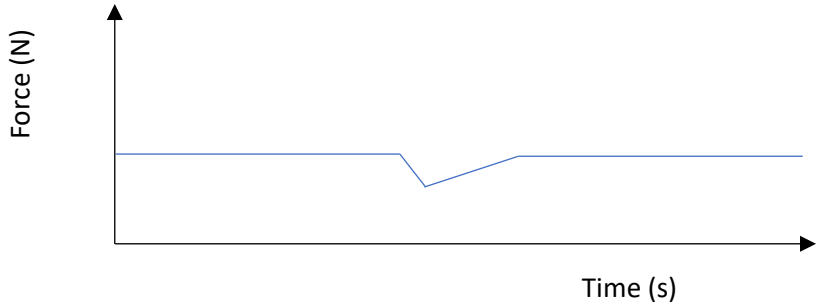

Figure 65 - Schematic graph of the desired force as a function of time to avoid the spike (achievable with the Spring Tool)

The aim is thus to make the machine "proactive", through a design that provides appropriate springs to compensate the force's spikes at the melting temperature. The introduction of a new tool, named *Spring Tool*, has the purpose to reach the expected results allowing for a better DoP in the automated industrial production of laser diodes.

The purpose of measurements on CoC produced using this new tool, was to check devices' characteristics compared to those produced by the *Lambda* machine (and of course to *Femto2* with standard tool). At the same time, we tried to prove that the *Spring Tool* would also allow a lower temperature of die attach.

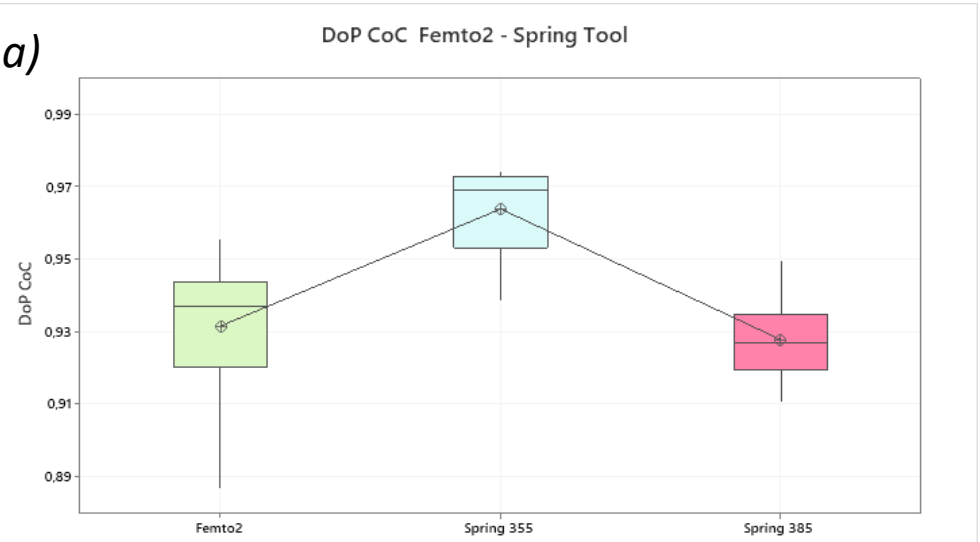

Statistics	Femto2	Spring 355	Spring 385
N	23	10	10
Mean	0.93157	0.96379	0.92783
StDev	0.017464	0.012295	0.011139
Minimum	0.8869	0.93853	0.9109
Maximum	0.95546	0.97429	0.94965

Figure 66 - a) Boxplot of CoC DoP by different Tool and temperatures b) Statistical analysis for data reported in a)

The CoC produced at high temperature ($385°C$) with the *Spring Tool* do not present statistical evidence of DoP improvement. Meanwhile, using the *Spring Tool* at $355°C$ to produce CoC provides a significantly higher DoP. Data indicate that, when using the same tool, the temperature determines the difference in DoP.

Devices' production using the *Spring Tool* should ensure the planarity along the *X axis* during die attach. This is why it allows for good control of many criticalities associated with die attach (i.e. overhang control) and to carry out the process at lower temperatures than the standards at which *Femto2* machine works. This result has allowed also working on the standard tool to check the flatness, namely a greater adherence between the tool and the CoC. Now it should be possible also do the die attach with the standard tool at lower temperature. The last one is an assumption that needs to be verified.

Comparing the results obtained with all processes (machines and tools), including the ones obtained with the *Lambda* machine, we realise that the difference does not depend only on temperature (T). In fact, using the *Lambda* machine the T is about $355°C$ too, but the DoP is lower than the one obtained using the *Spring Tool* at $355°C$.

a)

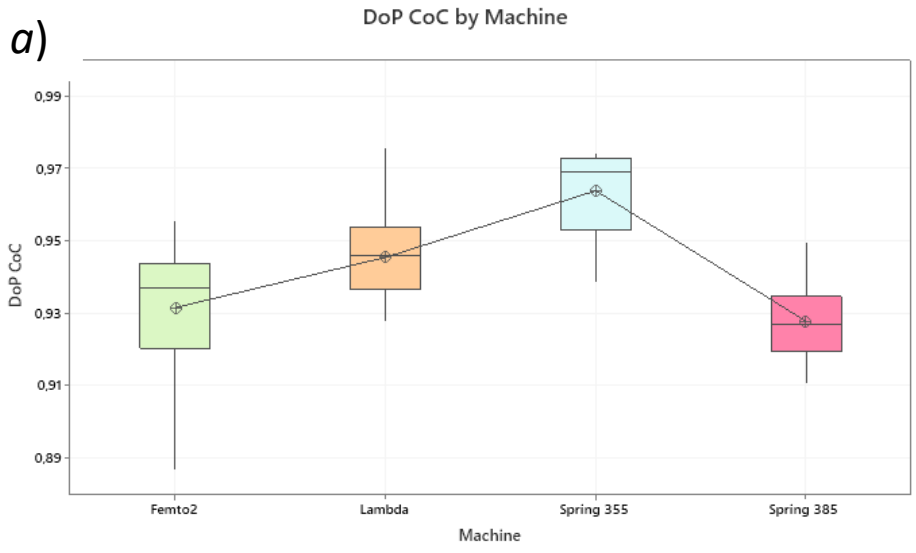

Statistics	Femto2	Lambda	Spring 355	Spring 385
N	23	29	10	10
Mean	0.93157	0.94545	0.96379	0.92783
StDev	0.017464	0.011269	0.012295	0.011139
Minimum	0.8869	0.92771	0.93853	0.9109
Maximum	0.95546	0.97564	0.97429	0.94965

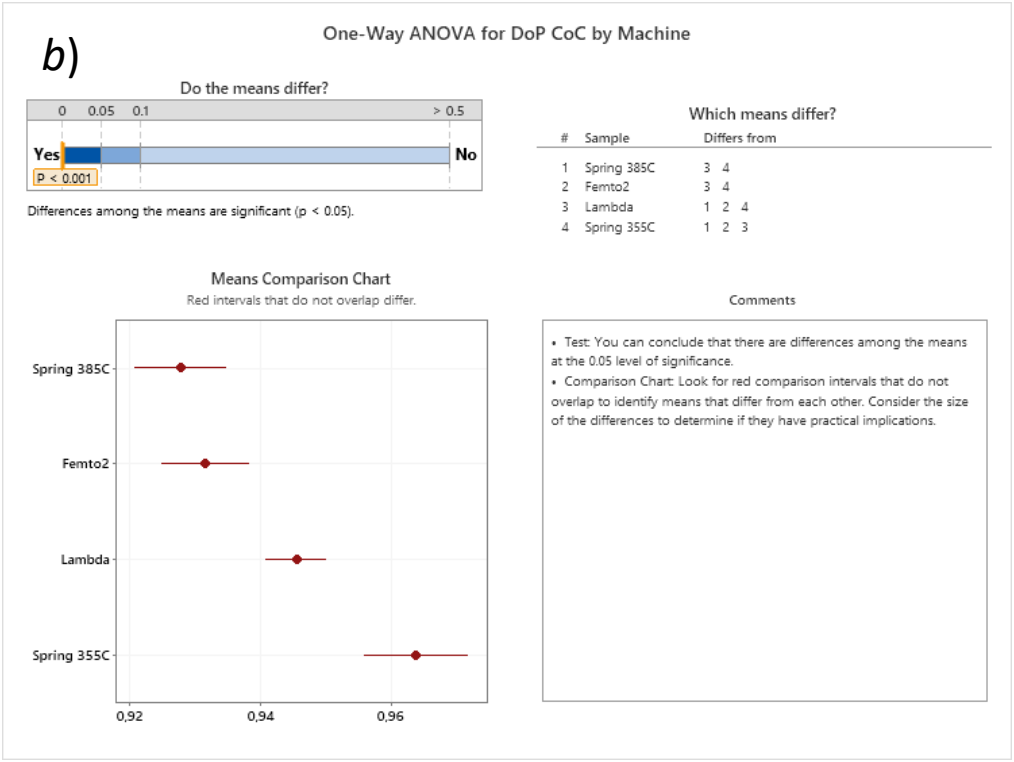

Figure 67 - a) Boxplot of CoC DoP by different machines and tools b) Statistical analysis for data reported in a)

In this paragraph, we investigate if there are ways to characterize and quantify the semiconductor mechanical stresses inducing DoP degradation.

In order to measure the microscopic deformation due to the soldering process, interferometric microscopy was chosen. This technique allows obtaining the deformation profile along the *z* and *y axis*, with reference to the following figure. Thus, along the optical cavity and the lateral direction of the laser chip.

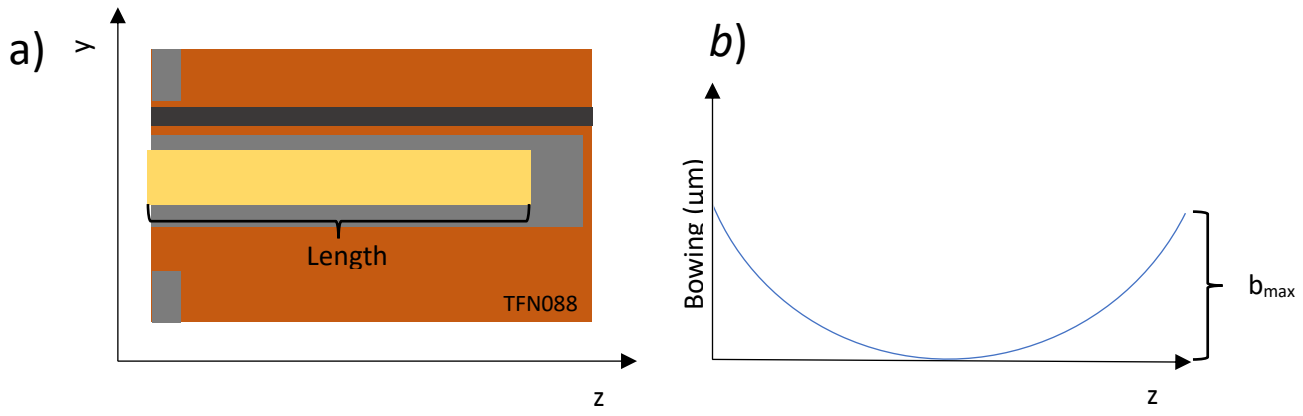

Figure 68 - a) Schematic representation of the diode with the respective axis taken into account. b) Dummy example of a deformation curve

The interferometric microscope provides the coordinates of the points of the chip surface. The resulting text file can be processed with any data analysis program. In this case, Matlab was used to create 2D maps in which it is possible to visualize the microscopic deformation of the CoC, from which the profile has been extrapolated along the two directions orthogonal to the plane. In the data analysis we will only measure the distortion (*bowing*) along the long side of the chip (z axis), given that the width of the chip is very small, in this case its deformation can be considered irrelevant.

The *bowing* was measured as:

$$Bowing = \frac{b_{max} - b_{min}}{diode\ length} \quad (6.1)$$

As we will see later, the profile similarity of the CoC soldered using the same conditions can be verified. From the shape of these profiles, we may define a fingerprint of the machine or even of the tool.

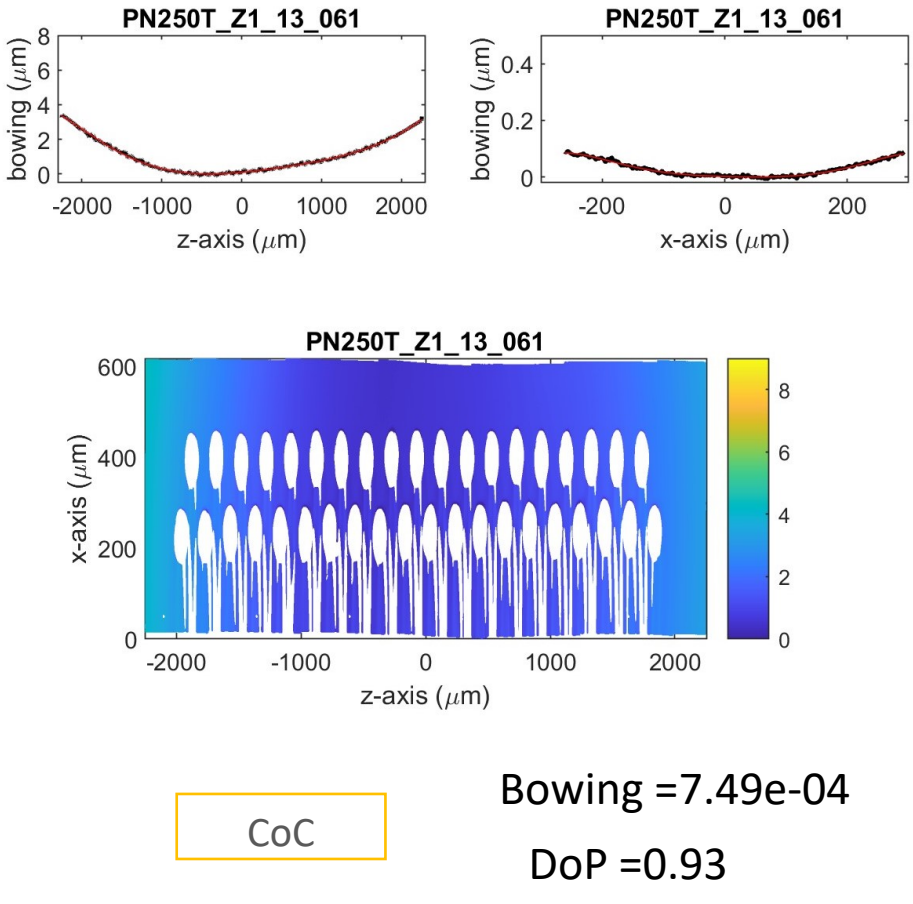

Figure 69 - Deformation map and bowing profile example of a CoC soldered with Lambda machine

The *Lambda*'s profile consists of a parabolic-like curve that has a slight shift on the diode's back facet, this is its fingerprint.

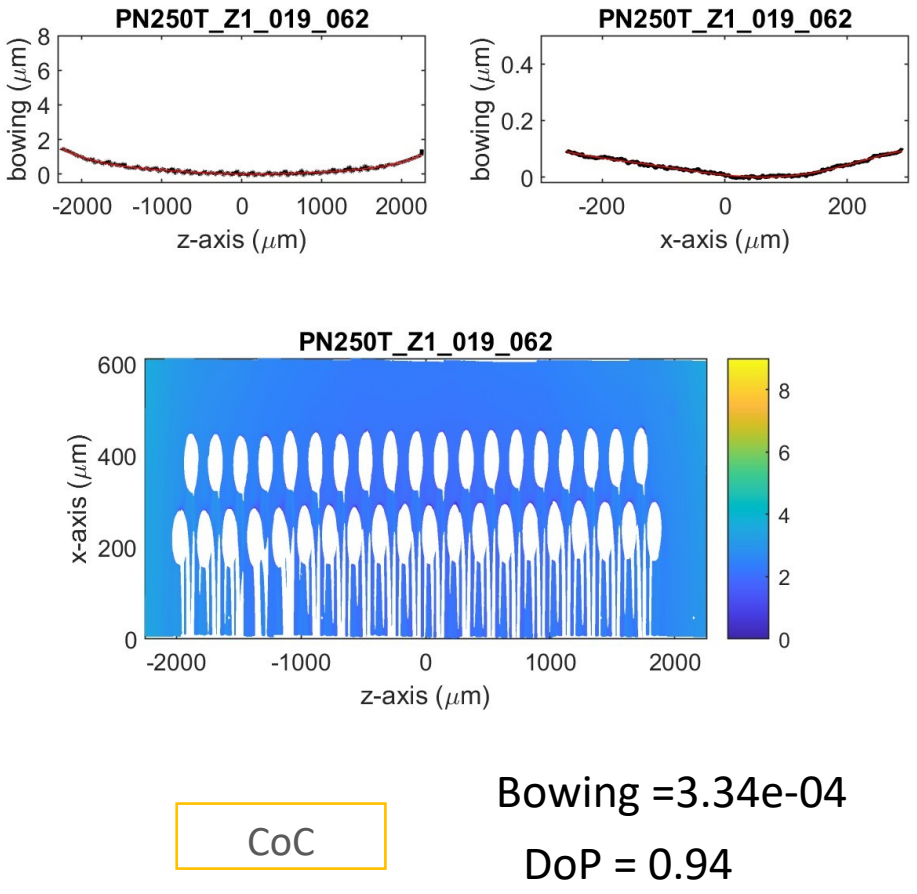

Figure 70 - Deformation map and bowing profiles example of a CoC soldered with Femto2 machine

For the *Femto2* machine, the profile fingerprint consists of a flattened parabolic-like curve with a central minimum, see the picture above.

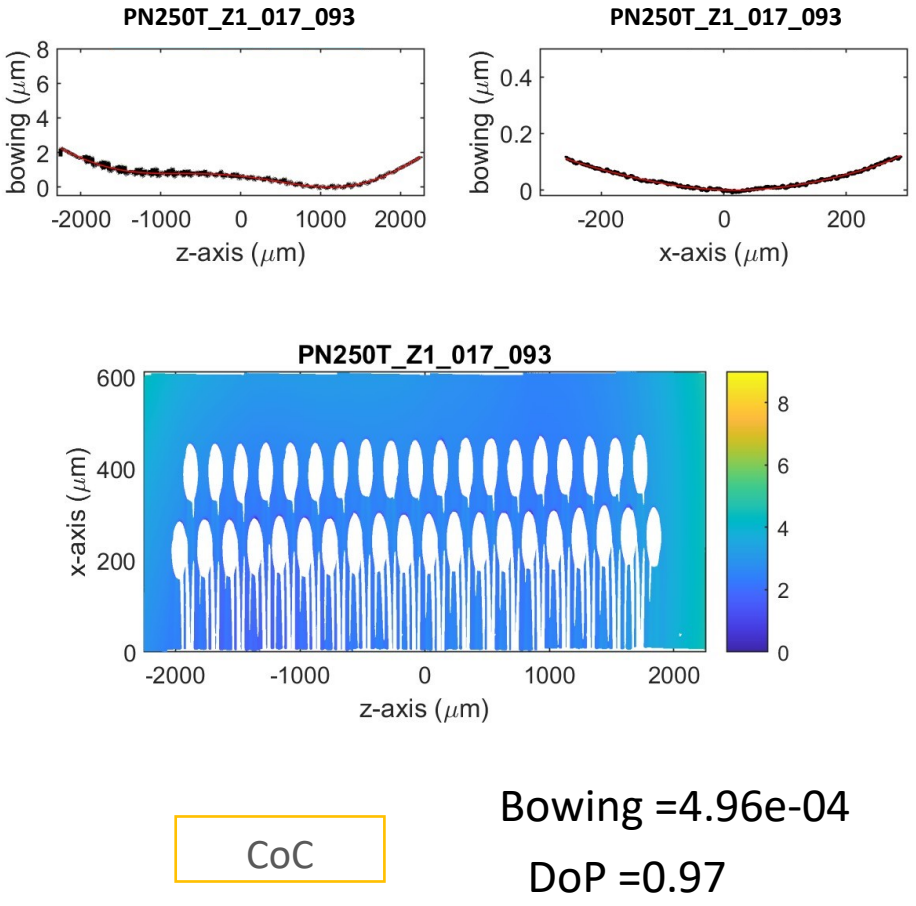

Figure 71 - Deformation map and bowing profiles example of a CoC soldered with the Femto2 machine equipped with the Spring Tool at 355°C

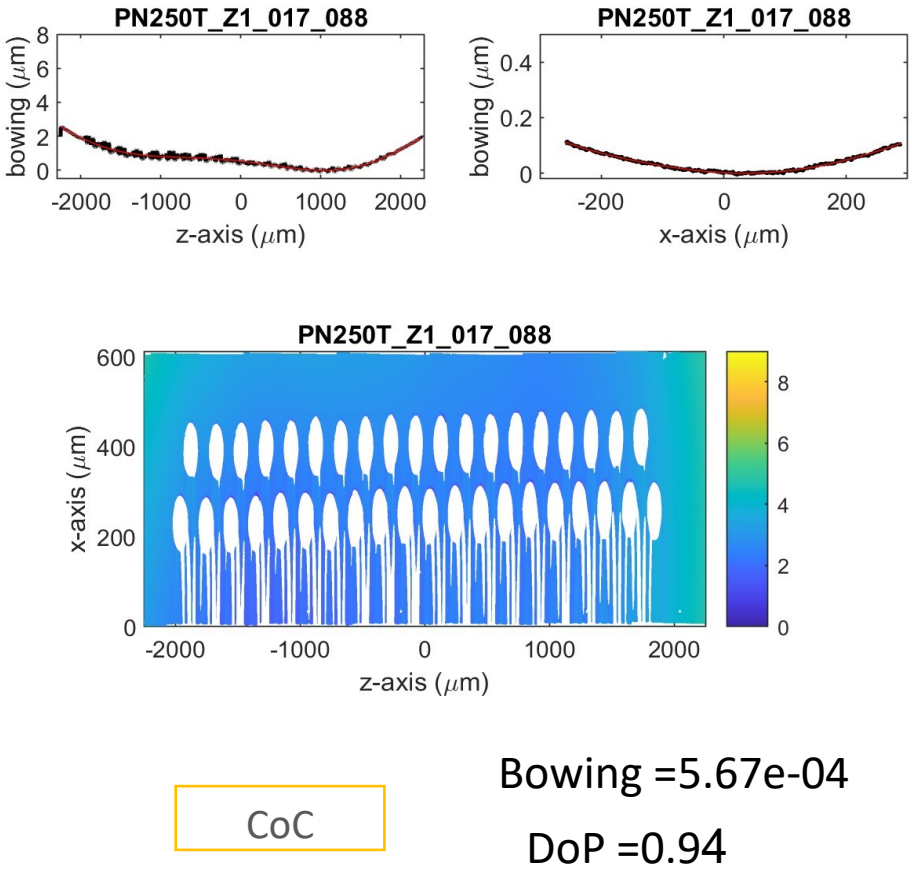

Figure 72 - Deformation map and bowing profiles example of a CoC soldered with the Femto2 machine equipped with the Spring Tool at 385°C

The profile of the *Spring Tool* is recognizable by the fact that the curve has two minima, the absolute minimum is moved towards the front facet.

Since the deformation of the chip is most likely due to soldering, it was initially thought that there might be a correlation between the chip deformation and the degree of polarization of the light emitted by the laser.

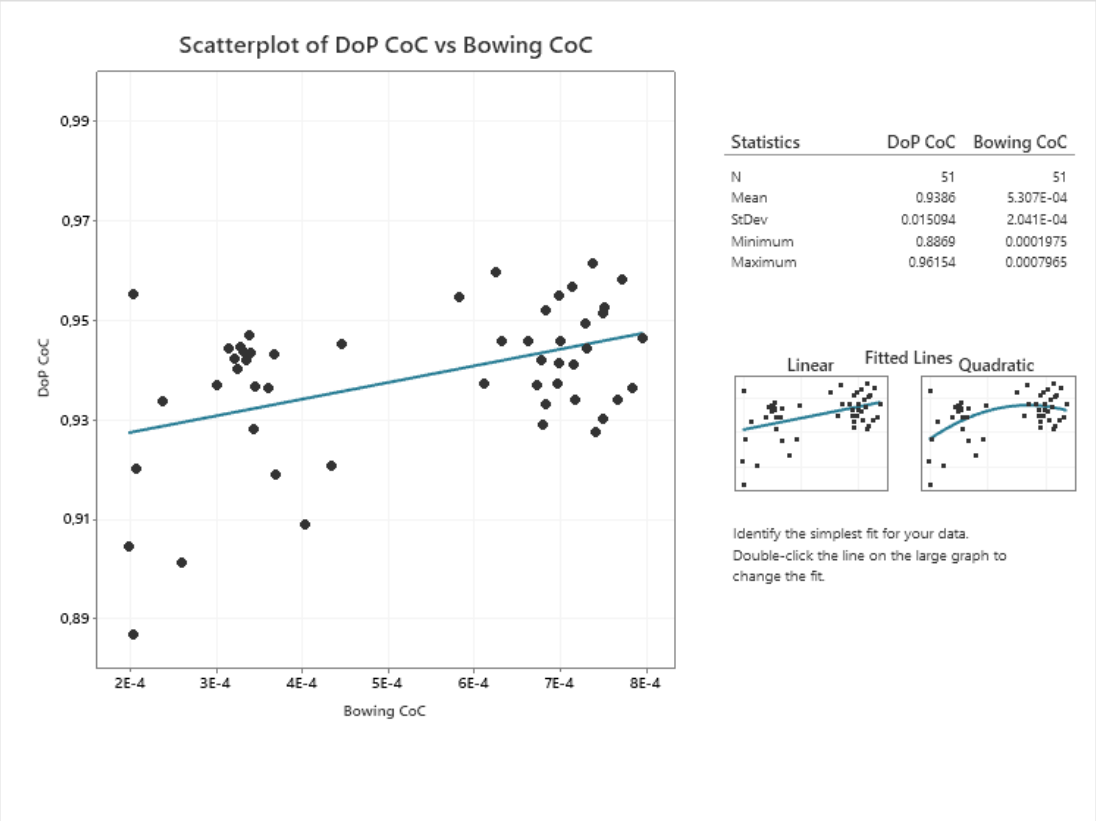

Figure 73 - Scatterplot of CoC DoP as a function of the bowing

The data of DoP as a function of the bowing, considered for all the machines and tools (*Lambda*, *Femto2* and *Spring Tool*), indicate a low correlation ($R^2 = 20\%$).

Nevertheless, analysing the plot there is evidence of a relationship between clusters of points and the machine/tool used for the production of the chips under measurement.

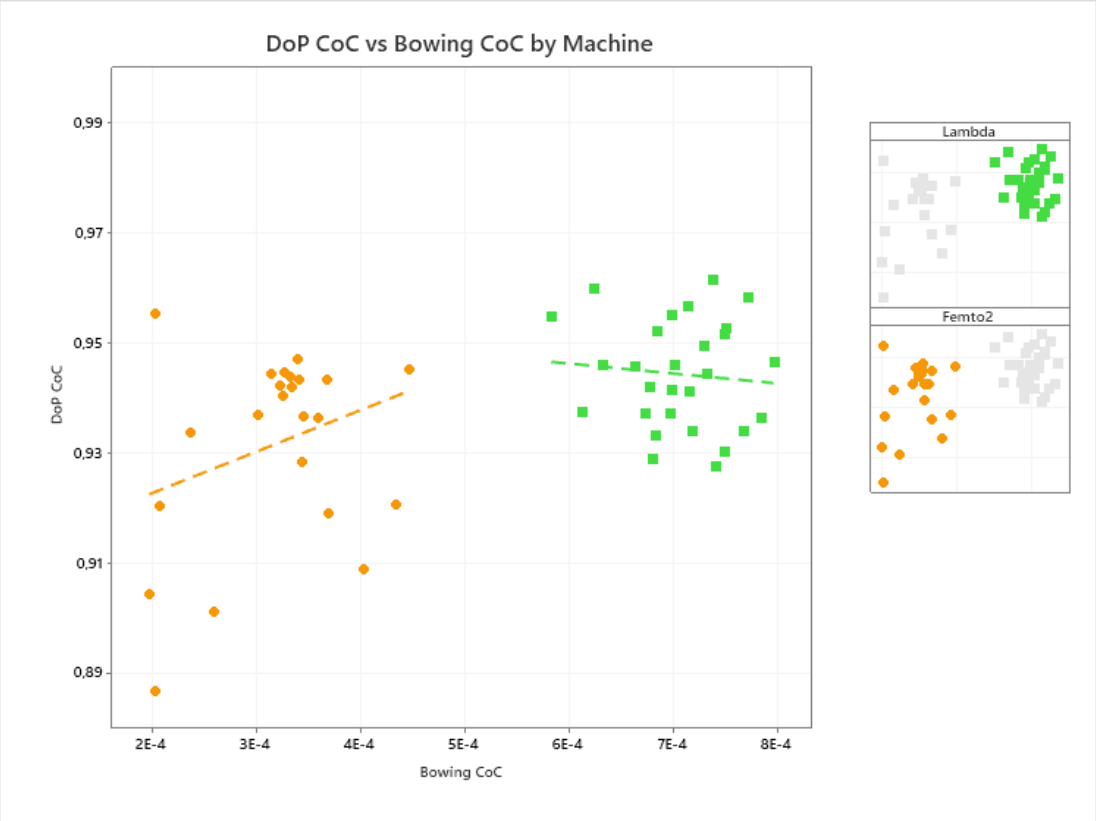

Figure 74 - Scatterplot of CoC DoP as a function of the bowing for different machines

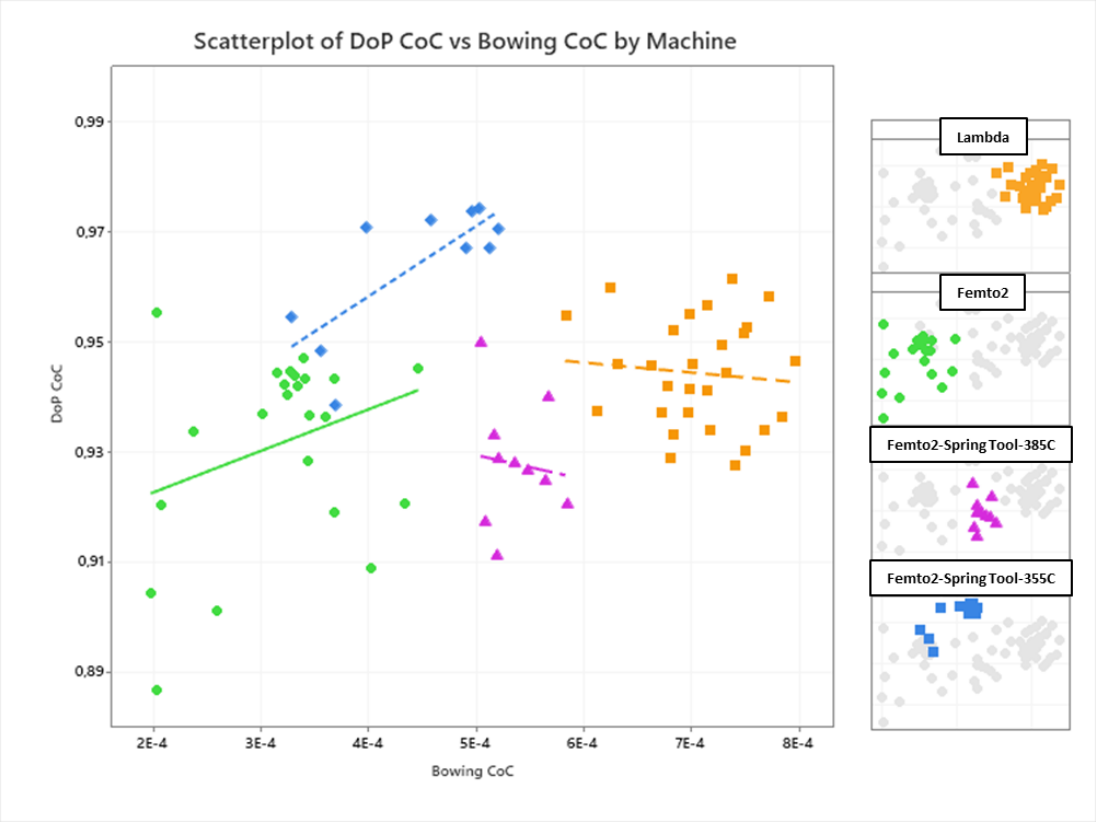

Figure 75 - Scatterplot of CoC DoP as a function of the bowing for different machines and tool

In fact, the scatterplot shows the clustering of data representing DoP as a function of bowing. In other words, it is possible to identify the fingerprint of a machine analysing the clusters. So, the bowing profile needs to be parametrized to investigate a possible correlation because the absolute value is not enough.

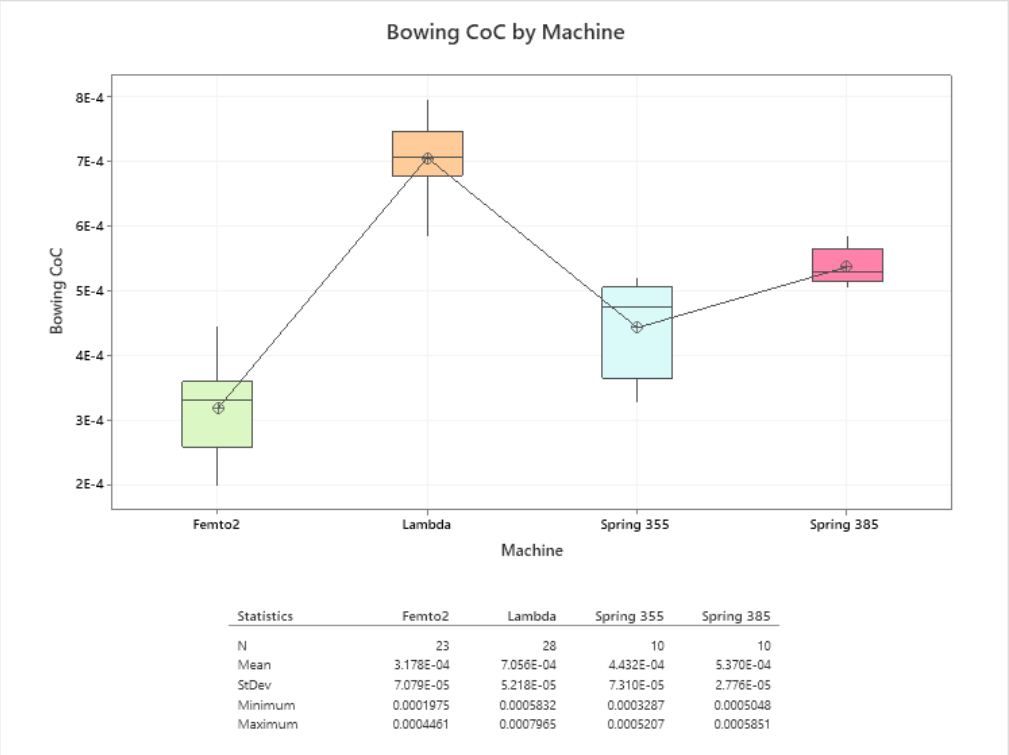

Figure 76 - Boxplot of CoC bowing by Tool

Given the production process, the bowing distributions of the machines and tools are really interesting, and, as we already showed, there are significant fingerprints for different machines and tools.

However, there is no apparent correlation between the DoP values and the bowing parameters for the four measured categories. This is another strong indication that it is the shape of the deformation profile that characterizes the DoP and not the absolute value of the bowing, at least for CoC. It is necessary to parameterize the shape of the longitudinal distortion.

6.2 DoP from CoC to HS

All the analysed CoC, those soldered with *Lambda* and those soldered with *Femto2*, with or without *Spring Tool*, were then soldered on the Heat Sink by means of the *Lambda* manual machine.

The objective was to investigate whether further soldering would further compromise the DoP and if it would affect the microscopic deformation. Again, correlations between the DoP and the bowing were sought, and the obtained data were compared with those previously measured on CoC.

The DoP-versus-current curves of the previously analysed CoC, before and after the soldering on the Heat Sink, are reported in the following pictures for the two machines.

6.2.1 DoP HS as a function of the machine

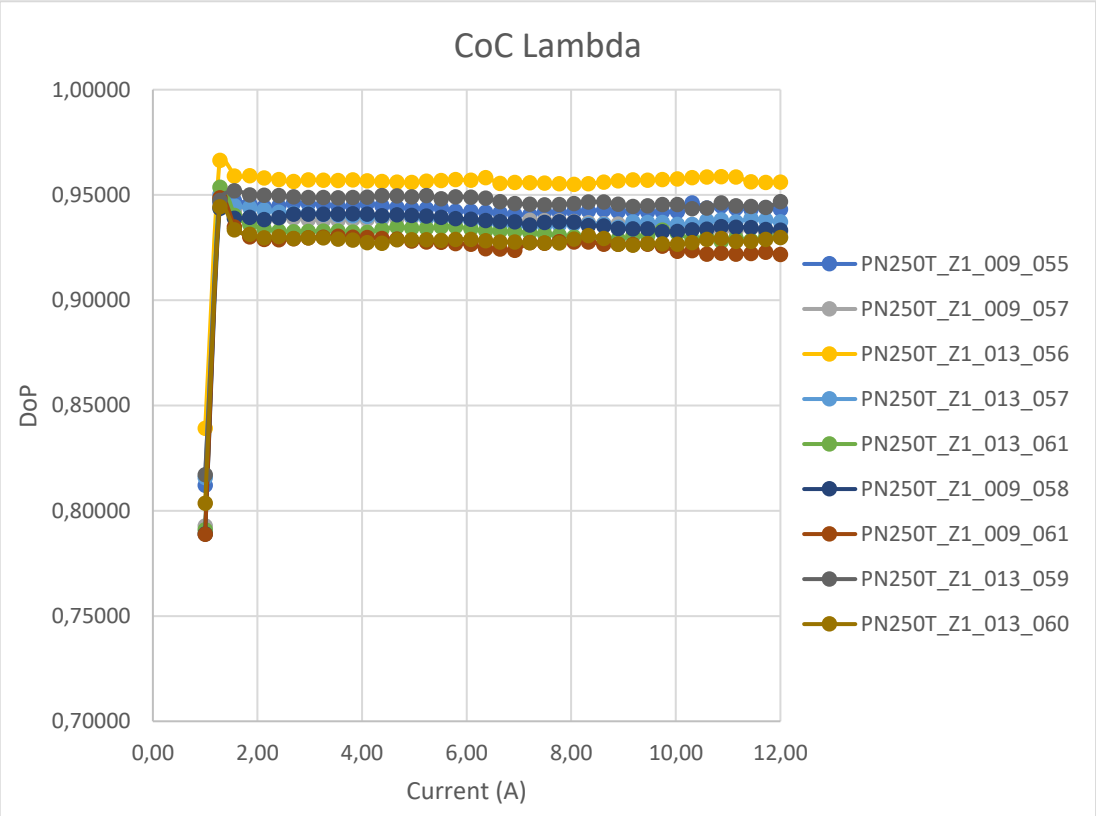

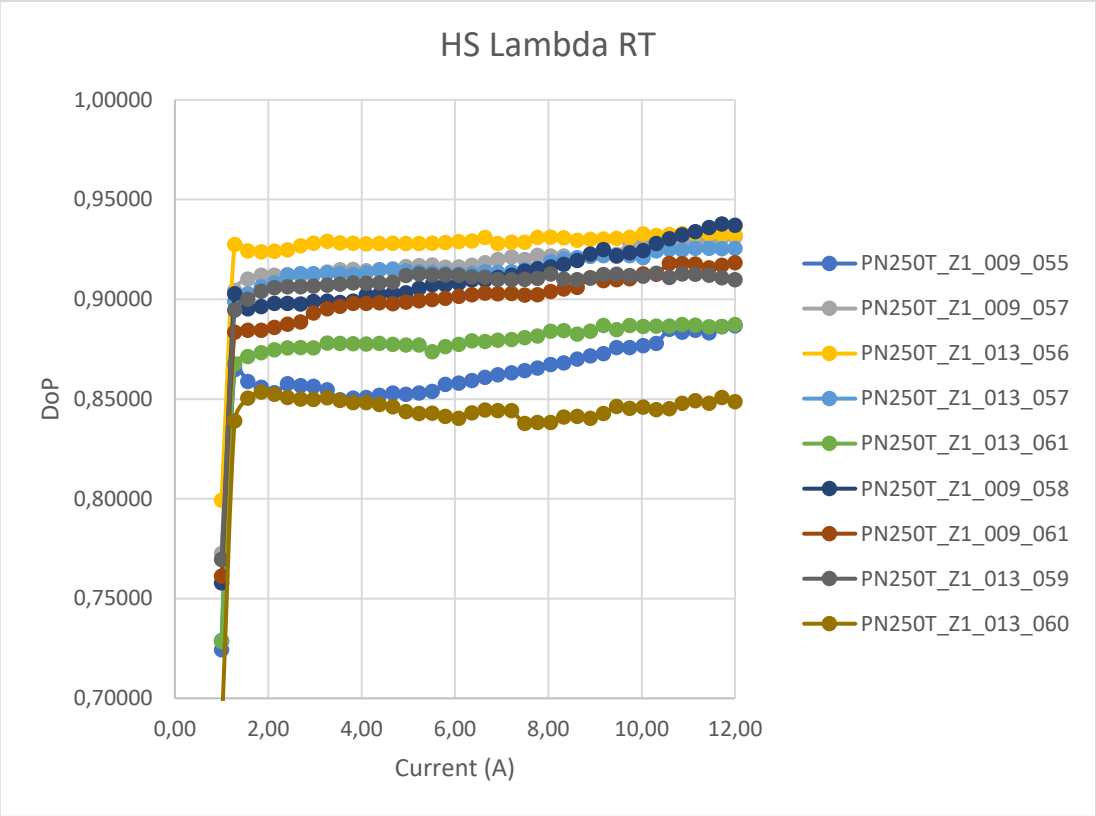

Figure 77 - DoP as a function of the current in the case of CoC and HS soldered with Lambda machine

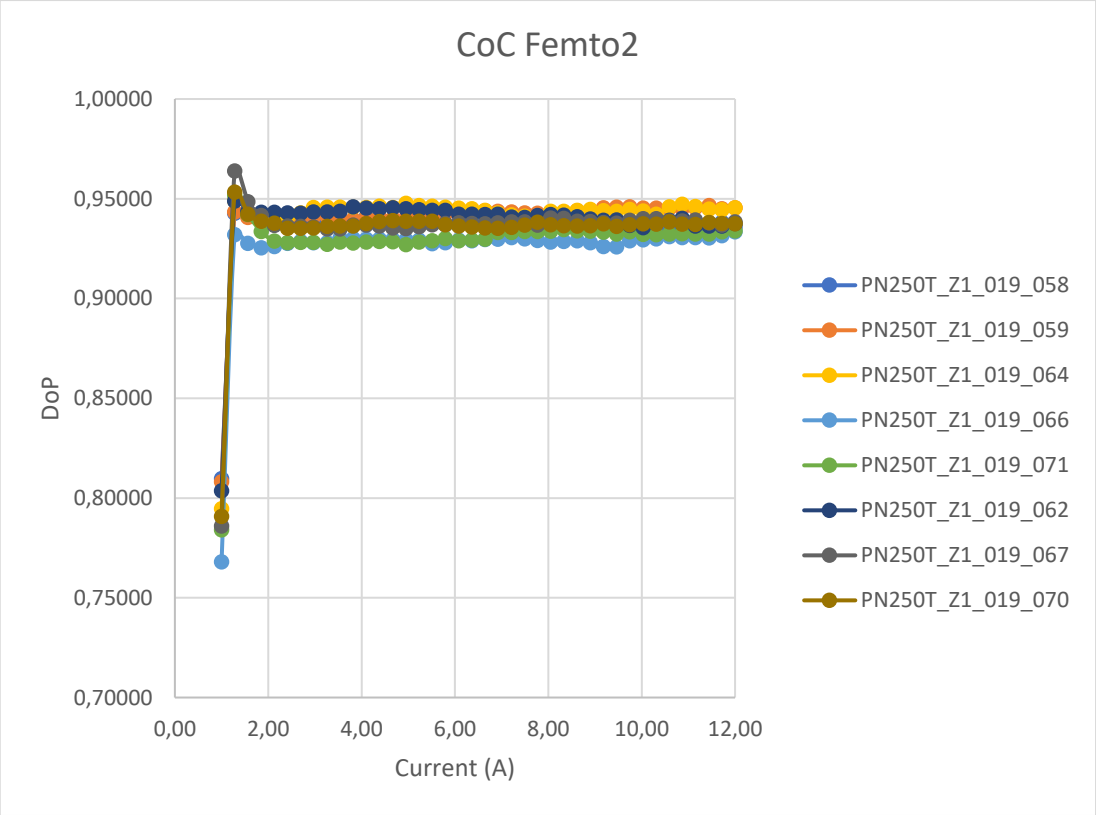

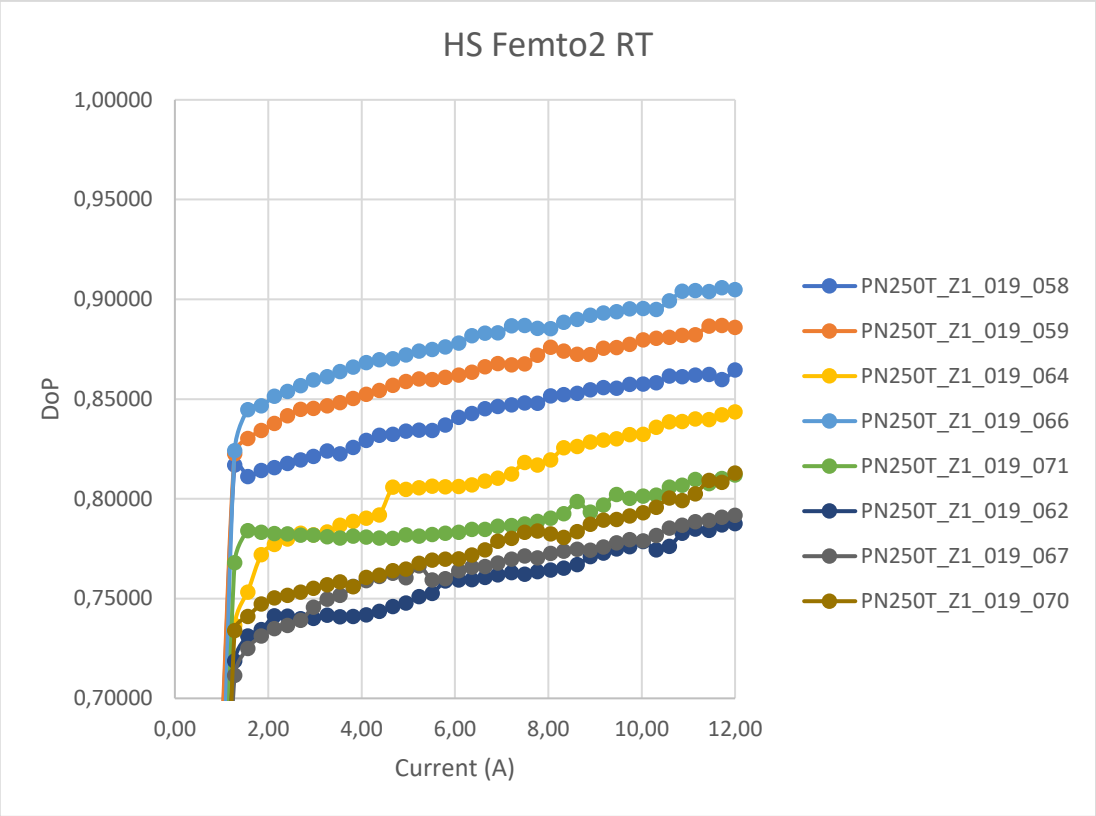

Figure 78 - DoP as a function of the current in the case of CoC and HS soldered with Femto2 machine

The joined data (*Lambda + Femto2*) of DoP show a significant difference between the two distributions, CoC before and after soldering on HS, see figures below a and b. It is evident a systematic degradation and a greater variance of the DoP after the soldering on the HS.

The soldering process, using a tin preform, has a strong negative impact on the stress induced on the laser diode. The reason lies in the peculiar characteristics of this soldering process, namely an explosive reaction.

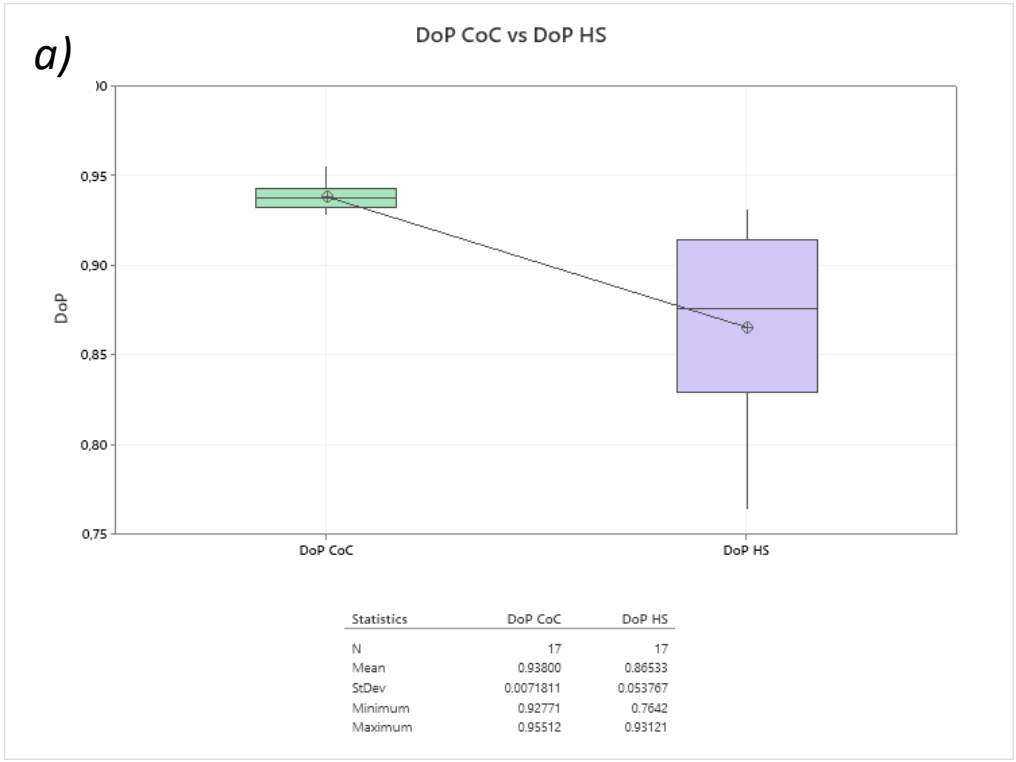

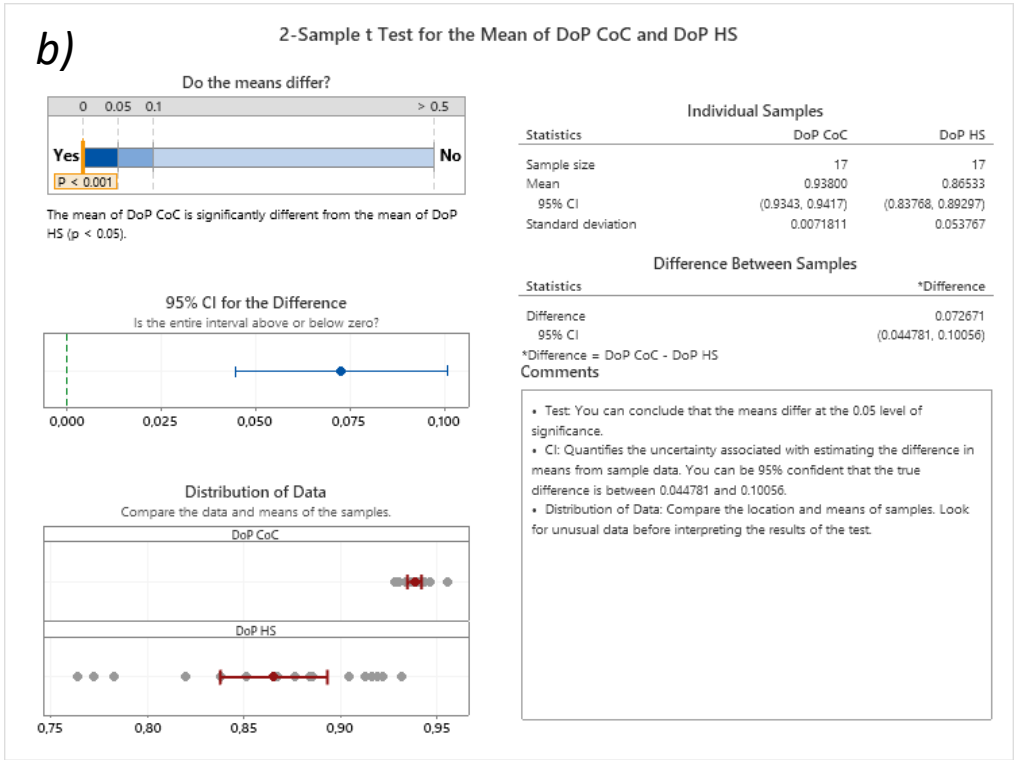

Figure 79 - 1) Boxplot of CoC DoP compared with HS DoP b) Statistical analysis of DoP difference

The statistical evidence of the 17 samples analysed (9 soldered with *Lambda* and 8 with *Femto2*) shows a clear difference between the CoC DoP before and after soldering them on the Heat Sink; we will now check if this difference is consistent for both diodes soldered with *Lambda* and *Femto2*.

From now on, the term "machine" will refer to the one used to solder chips on carrier, thus originating the CoC, while the machine used to solder CoC on the Heat Sink is always the *Lambda* one.

a)

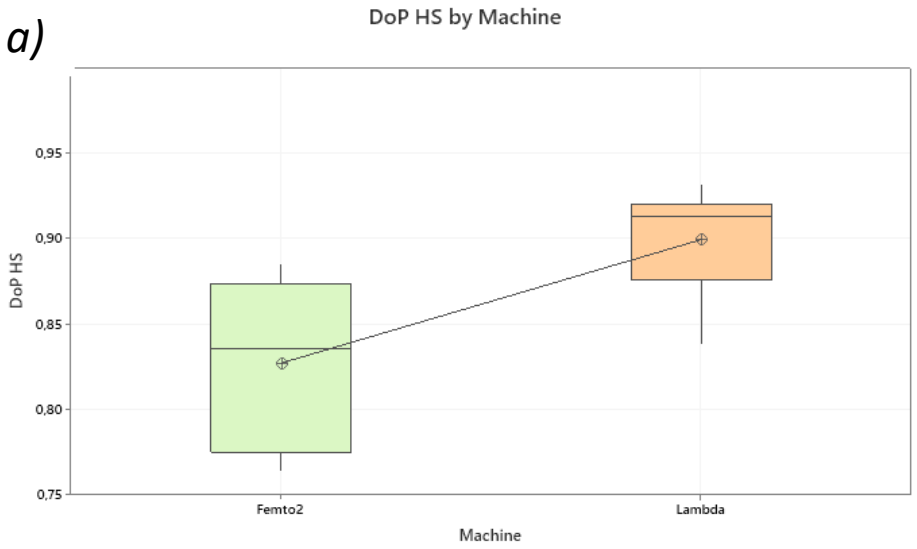

Statistics	Femto2 RT	Lambda RT
N	8	9
Mean	0.82709	0.89932
StDev	0.048984	0.030343
Minimum	0.7642	0.83823
Maximum	0.88521	0.93121

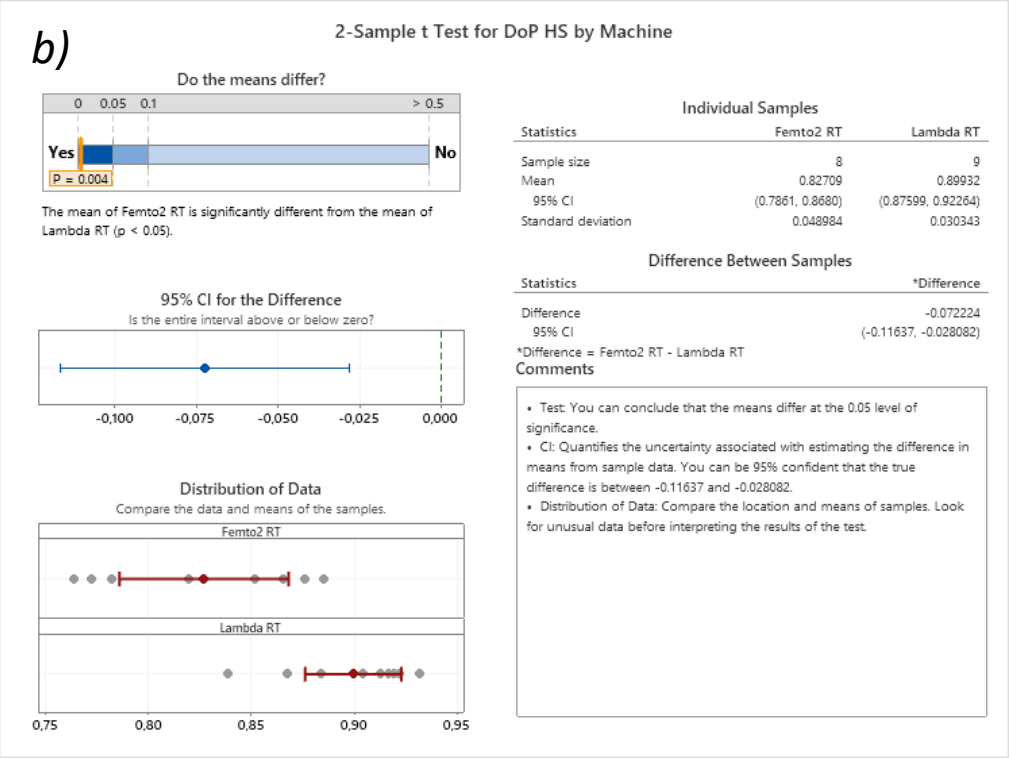

Figure 80 - a) Boxplot of HS DoP by machine b) Statistical analysis of DoP difference

Also, for HS, the data confirm a significant statistical difference between the two distributions.

As it was measured with the CoC not soldered on the HS, the DoP of the chips soldered with *Lambda* is greater than the ones soldered with *Femto2* under the same conditions (process, type and carrier lot).

We may now verify if, again, the chips soldered with the *Femto2* machine equipped with the *Spring Tool* will give better results than those soldered with the standard tool of the *Femto2*.

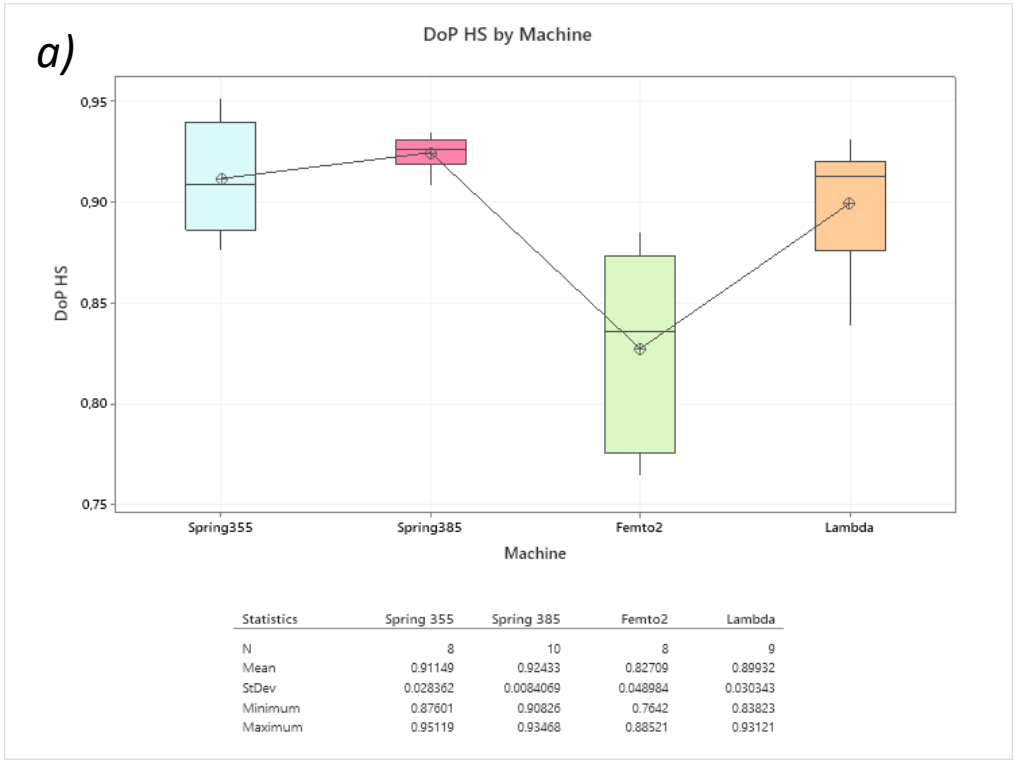

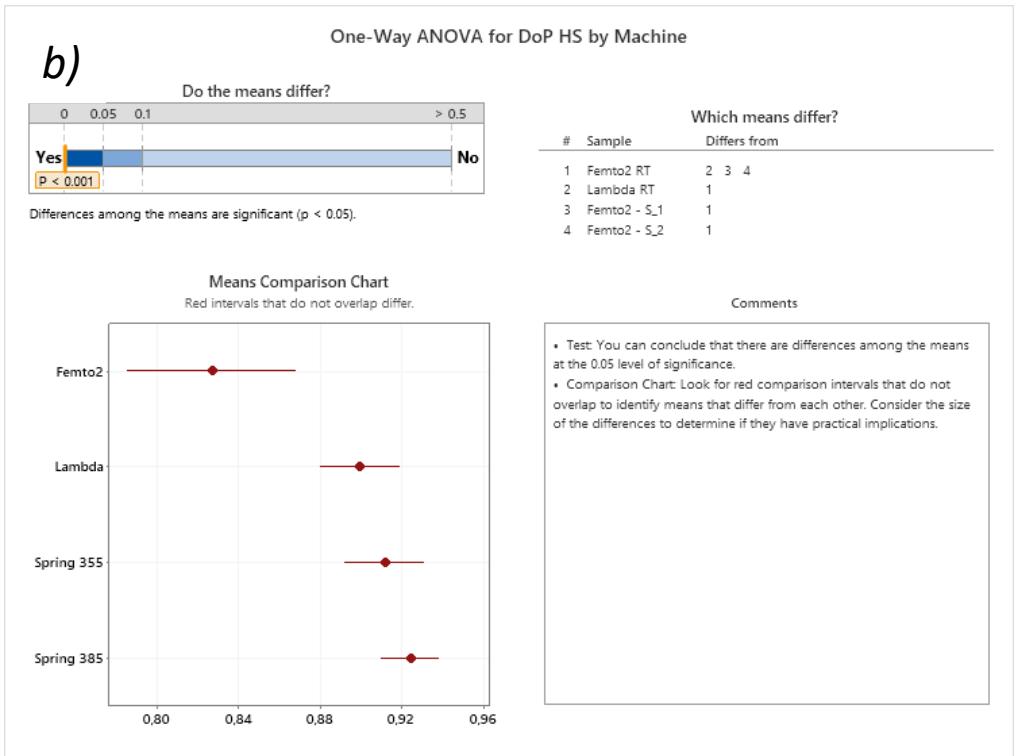

Figure 81 - a) Boxplot of HS DoP for different machines and tool b) Statistical analysis of HS DoP

We notice that, also after soldering the CoC on HS, the DoP of devices produced using the *Spring Tool* shows a clear difference from those produced with the standard *Femto2*.

Nevertheless, the soldering temperature effect observed on CoC is no longer visible on HS. In fact, while CoC made using the *Spring Tool* at $T = 355°C$ showed a higher DoP than those soldered at $T = 385°C$, now, after the HS soldering, the DoP obtained with the two soldering temperatures are not significantly different, see ANOVA results in the previous figure. Poorer quality is instead obtained with standard *Femto2* HS soldered chips, they show a lower DoP with a large standard deviation.

Basically, it is confirmed that chips soldered with the *Spring Tool* behave in a better way than the ones soldered with the *Standard Tool*.

The DoP of chips soldered with the *Spring Tool* at $385°C$ conserved the DoP value of about 0.92 while the DoP of chips soldered at $355°C$ decreased by about 0.05, from 0.96 to 0.91.

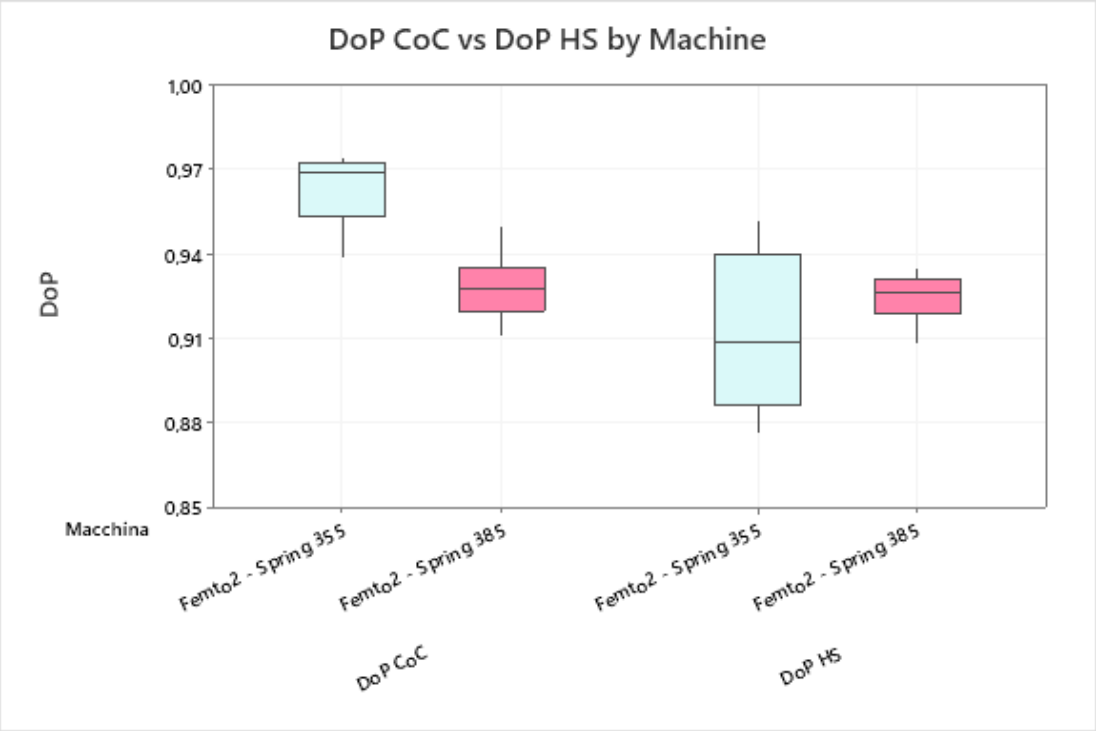

Figure 82 - Boxplot of CoC DoP and HS DoP for chips soldered with Spring Tool divided by temperature

We need more investigation to understand what combination of tools and conditions gives the best DoP. The investigation done so far to improve the production of the CoCs can be considered a starting point to improve the production of the multiemitter modules in which the CoCs are soldered.

The use of *Spring Tool* at $385°C$ shows better results about soldering degradation on the Heat Sink, in fact statistical distributions differ very little before and after HS soldering, while for production at $355°\ C$ we observe significant differences.

This behaviour can be clearly seen if we analyse the difference between the CoC distributions before and after HS soldering. As shown in *Figure 82* there is almost no variation in the data obtained using devices produced with *Spring Tool* at $385\ °C$, while we have significant differences in the mean value for the others and with a larger standard deviation.

It should be checked with further soldering experiments, but the data reflect the fact that this type of soldering process produces a random DoP degradation blurring the effects observed on CoC.

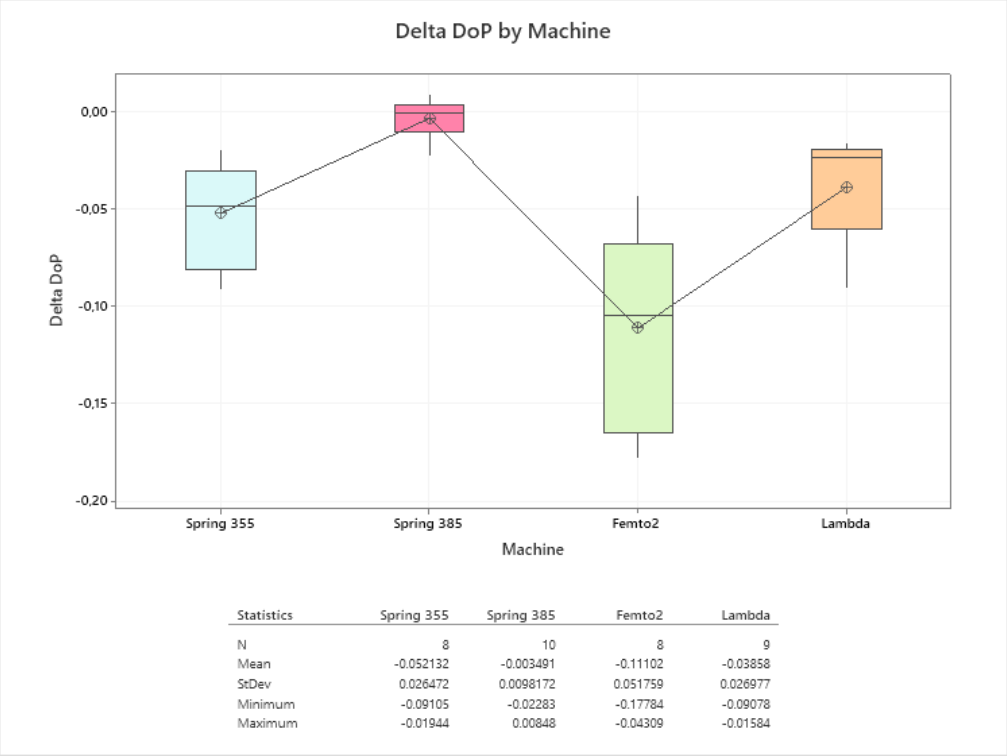

Statistics	Spring 355	Spring 385	Femto2	Lambda
N	8	10	8	9
Mean	-0.052132	-0.003491	-0.11102	-0.03858
StDev	0.026472	0.0098172	0.051759	0.026977
Minimum	-0.09105	-0.02283	-0.17784	-0.09078
Maximum	-0.01944	0.00848	-0.04309	-0.01584

Figure 83 - Boxplot of delta DoP by Tool

For correct statistical analysis, probably we need to use a comparison between single processes. The results of this statistic are shown below.

The changes are relatively small and also in this case *Spring Tool* at $385°C$ shows significantly better behaviour compared to other processes.

6.2.2 HS DoP and mechanical stress

In this paragraph, the microscopic deformation of the chips (on carrier) soldered on HS will be analysed. Also in this case Matlab has been used to create 2D maps in which it is possible to visualize the microscopic distortion of the CoC. The data analysis is relevant to the distortion (*bowing*) along the cavity length of laser the chip (*z axis*), given that its width is very small and its deformation can be neglected.

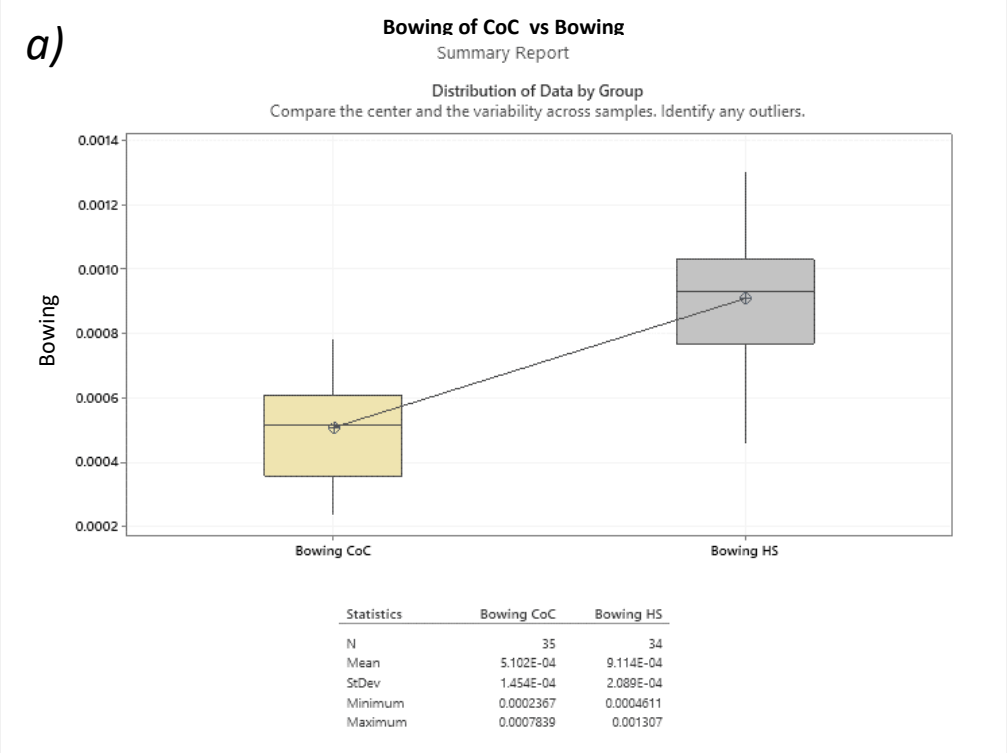

Statistics	Bowing CoC	Bowing HS
N	35	34
Mean	5.102E-04	9.114E-04
StDev	1.454E-04	2.089E-04
Minimum	0.0002367	0.0004611
Maximum	0.0007839	0.001307

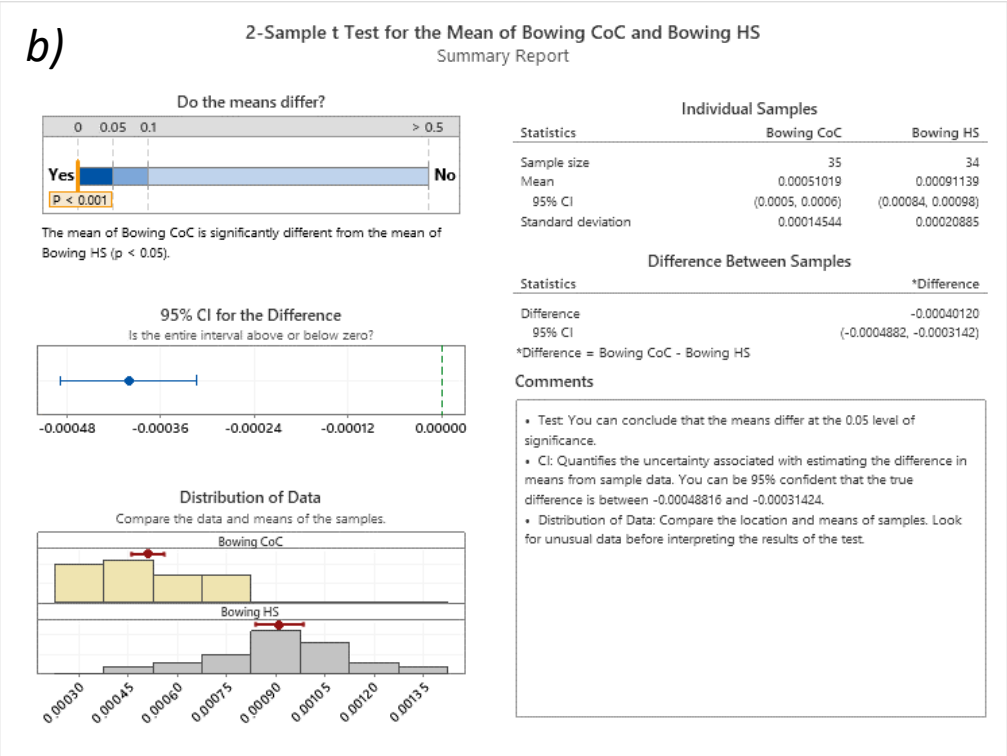

Figure 84 - a) Boxplot of CoC bowing vs HS bowing b) Statistical analysis of CoC bowing vs HS bowing

From previous figures, it is evident a change in the deformation (i.e *bowing*) that systematically increases in devices that are soldered on the HS.

Since we have seen that the DoP statistically decreases by soldering the CoC on the Heat Sink while the bowing increases, a correlation between the increase of deformation and the lowering of the DoP could be likely stated in this case.

The following figures show deformation profiles, after soldering the same CoC shown above on the HS.

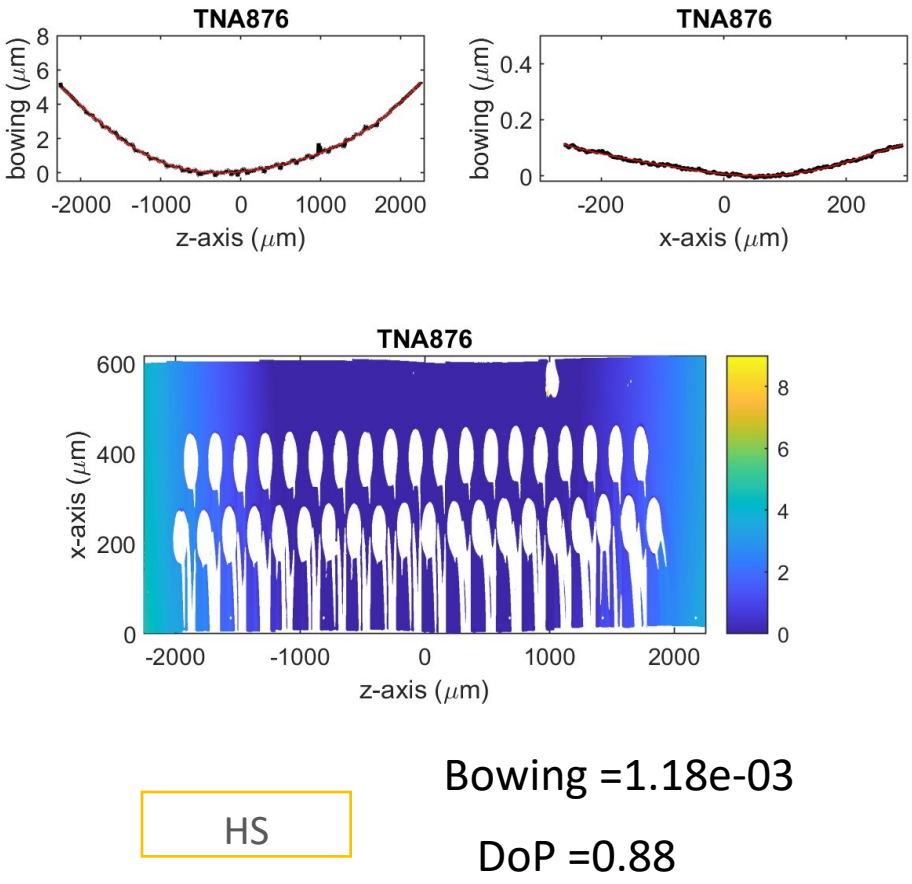

Figure 85 - Formation map and bowing profiles example of a HS soldered with Lambda machine

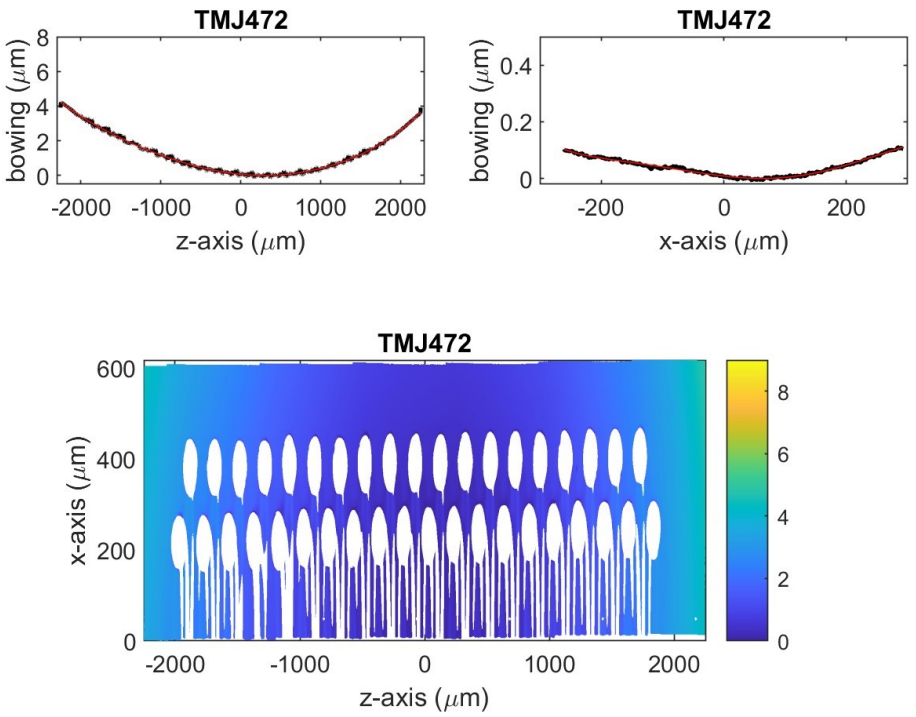

HS

Bowing =9.39e-04

DoP = 0.76

Figure 86 - Deformation map and bowing profiles example of a HS soldered with Femto2 machine

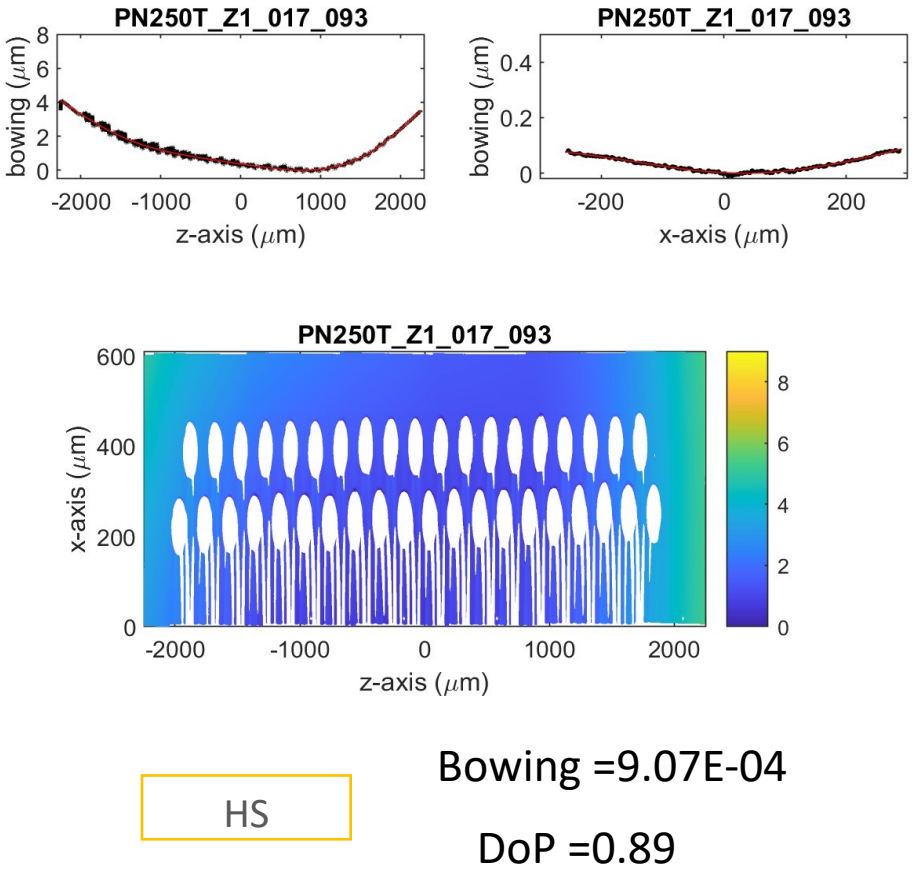

Figure 87 -Deformation map and bowing profiles example of a HS soldered with the Spring Tool at 355°C

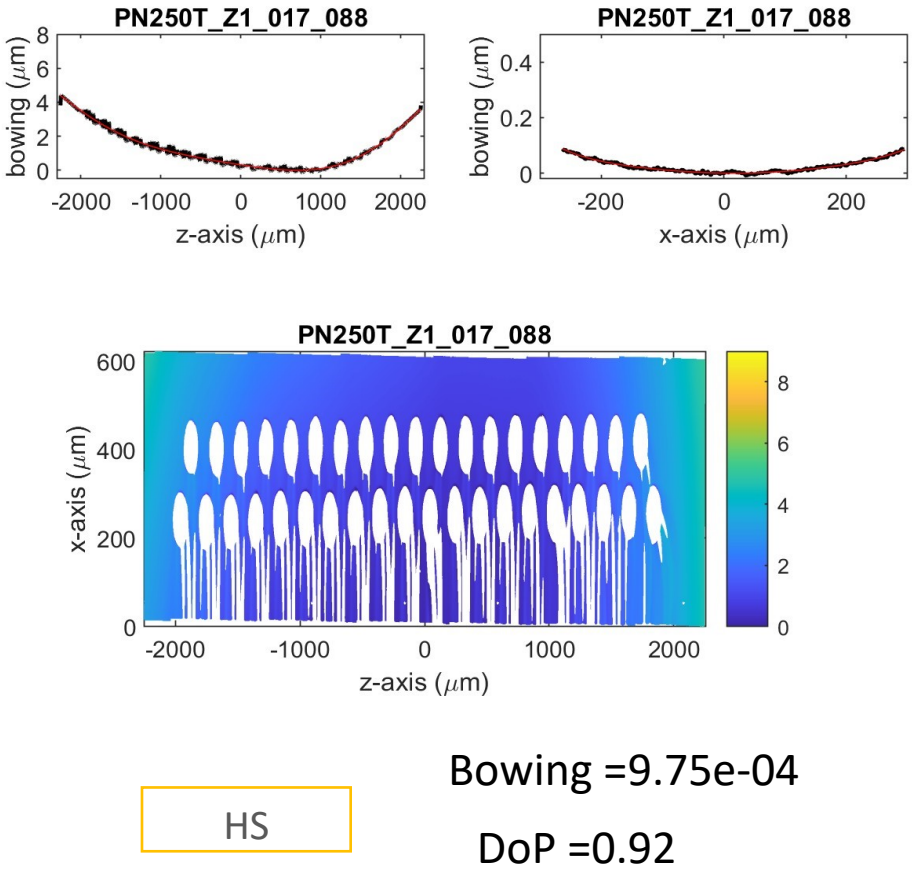

Figure 88 - Deformation map and bowing profiles example of a CoC soldered with the Spring Tool at 385°C

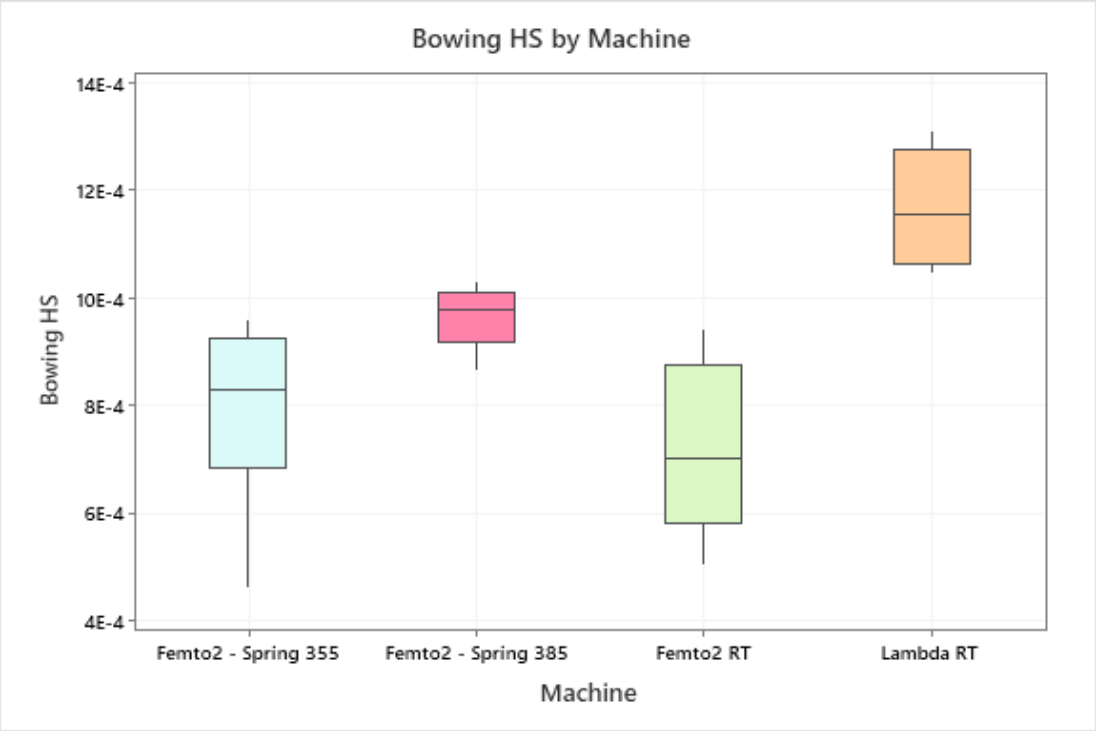

Figure 89 - Boxplot of CoC bowing for different tools and temperatures

The bowing distributions depending on the machines are interesting because they resemble those of CoC not soldered on HS, this is especially true for the difference between the *Femto2* and the *Lambda* machines.

The deformation profiles show a "homogenization" effect after soldering on HS. In fact, we see that the curves are parabola-like with a single minimum, even those of the devices soldered using *Spring Tool*, previously showing the two minima. It is reasonable to assume that this change in the deformation profile may be the cause of the degradation of the DoP.

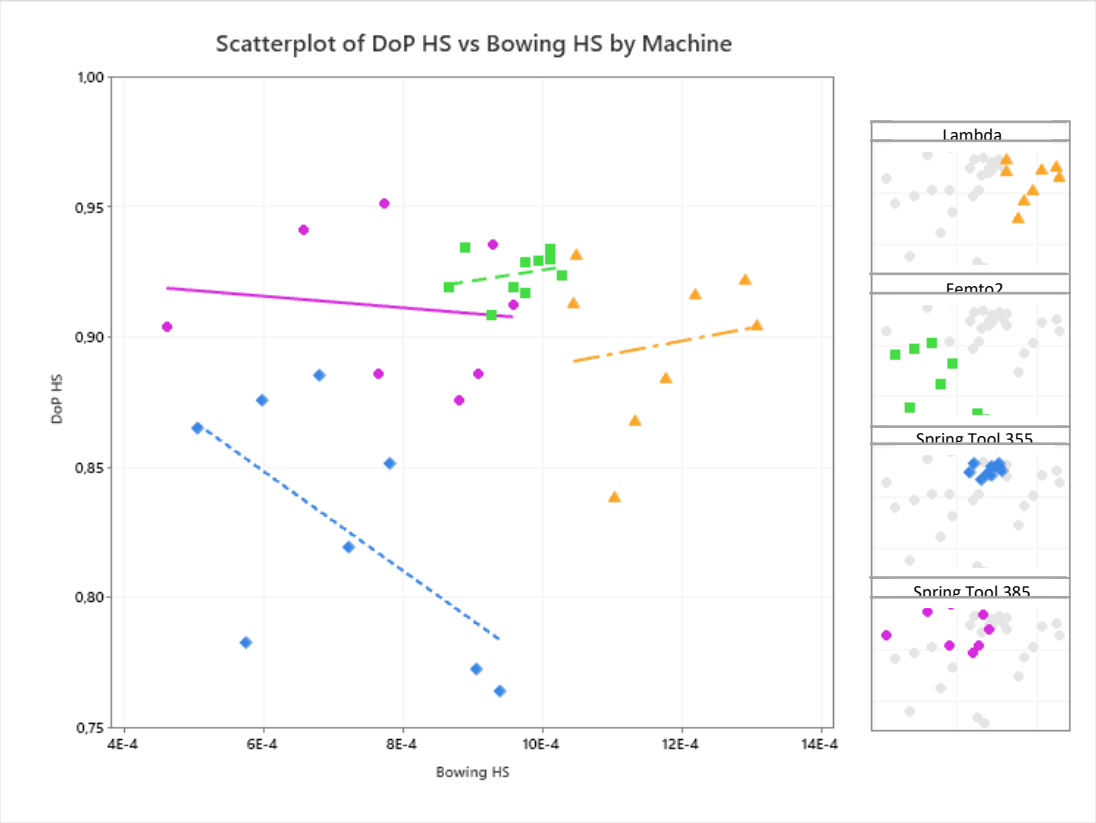

Figure 90 - Scatterplot of HS DoP as a function of the bowing for different machines and tool

After soldering CoC on HS, the clusters of DoP vs bowing previously observed are no longer visible. The deformation shape analysis for different machines and tools now cannot identify any fingerprint.

This confirms the strong impact of the soldering process using the tin preform that, somehow, «resets» the differences in the CoC (the «fingerprint»); we can call this behaviour an effect of «randomization» causing fingerprint categorization impossible

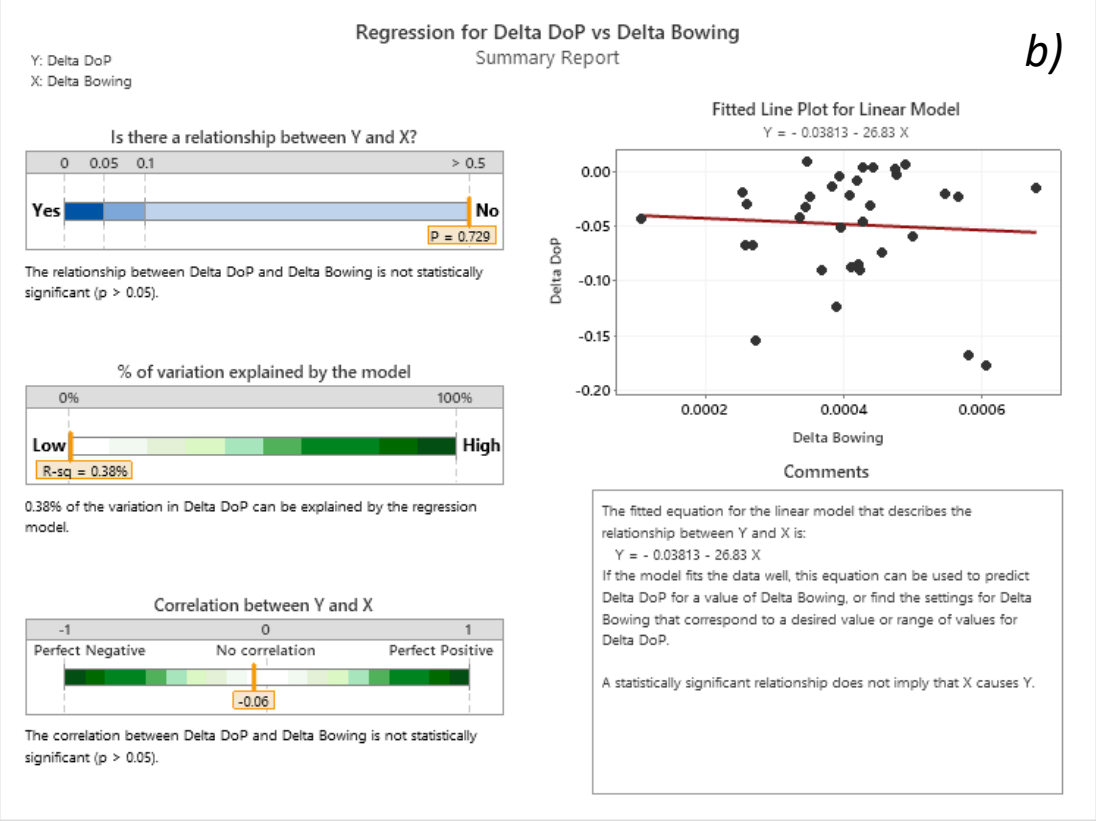

Figure 91 - a) Regression chart for delta bowing and delta DoP b) Statistical analysis of delta bowing and delta DoP

Analysis shows that there is no correlation of DoP change from CoC to HS, delta DoP, as a function of delta bowing (CoC to HS). This further result confirms that the soldering with the tin preform somehow «resets» the differences of «fingerprint» in CoC.

6.3 DoP vs current

In the following figures a summary of the DoP vs I curves for the different soldering experiments is reported:

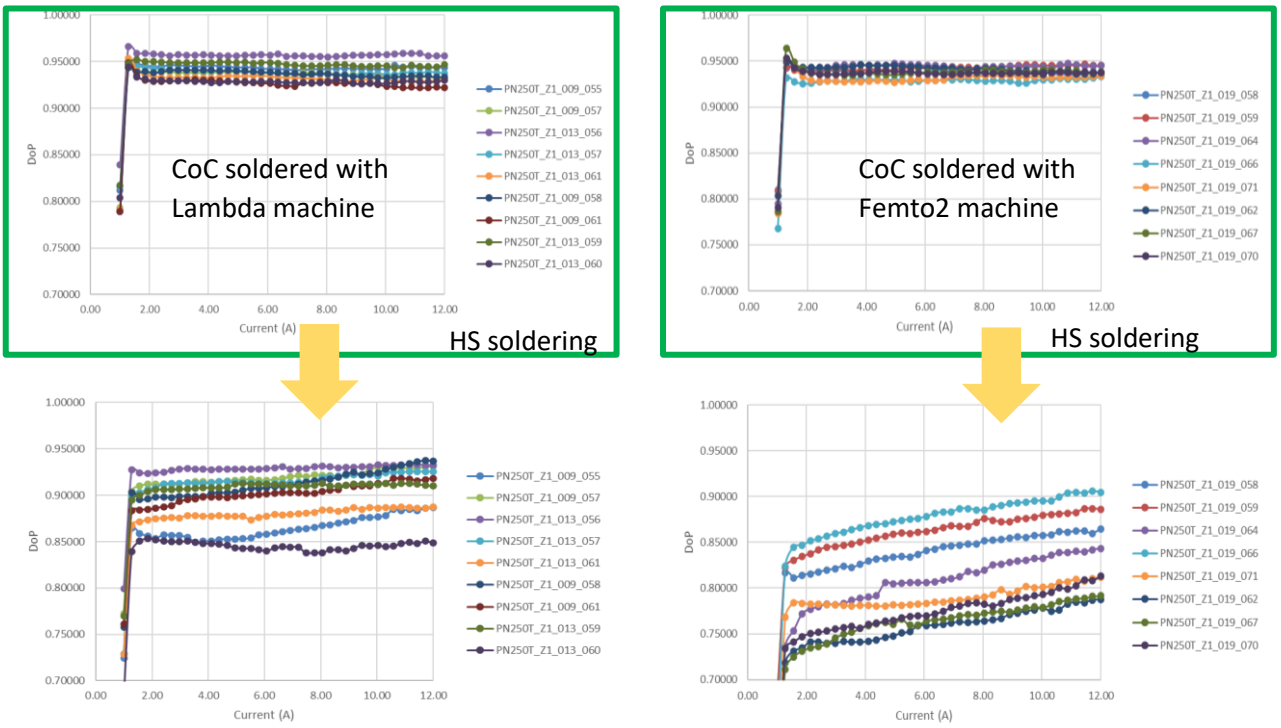

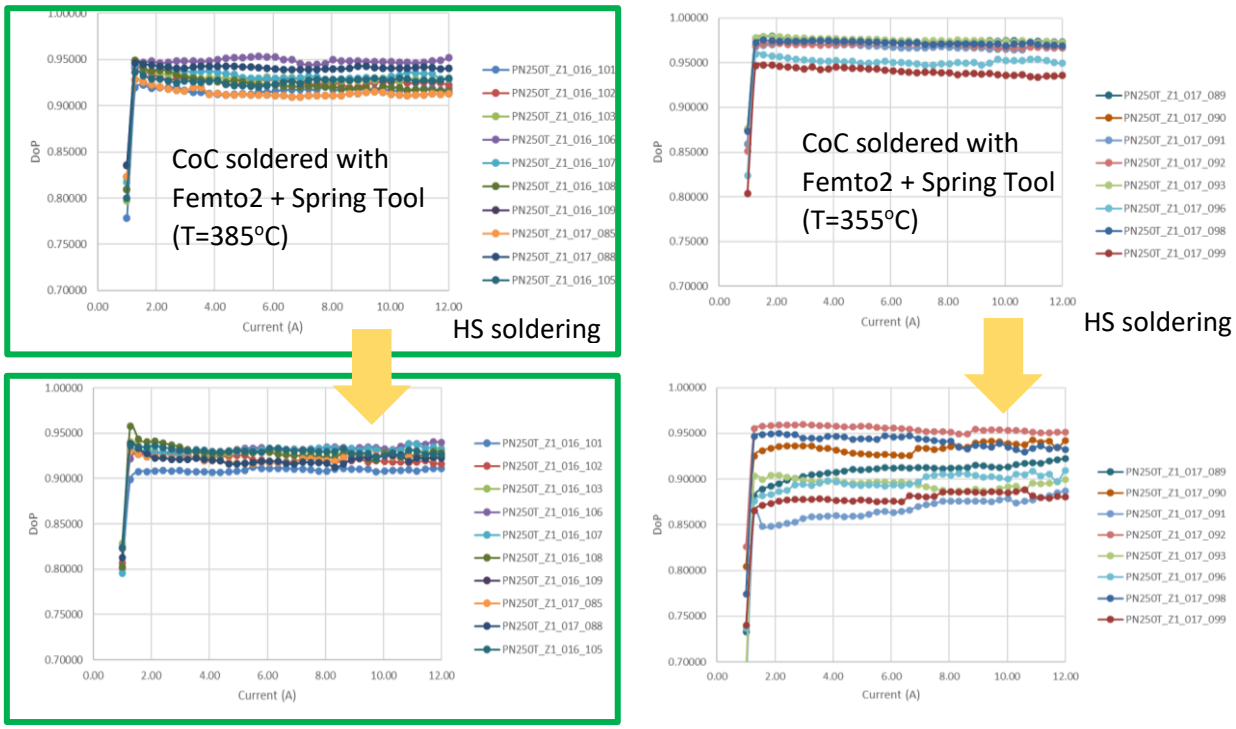

Figure 92 - Plots of the DoP as a function of the injected current for each set of data.

Based on the data obtained in the experiments, what emerges is the high DoP for CoC before HS soldering. The curves in this case are regular and flat, which means that DoP shows a small dependency on the injected current; values are grouped around a common value, both in the case of *Lambda* and in the case of *Femto2* soldering process.

After the soldering on HS, we notice a greater dispersion of the DoP values, with a subsequent degradation. In addition, the curves are no longer flat but show an increasing trend, especially in the case of chips soldered with the standard tool *Femto2*.

This trend can be related to the characteristics of the soldering and probably accounts for the randomization of the DoP values with soldering on HS.

Particularly relevant are data of chips soldered with the *Spring Tool* at 385° C, we see that DoP values are stable and relatively high for all the chips. This means that all the chips in this family have the same behaviour.

These are very important results of machine development and optimization of die attach parameters. These results suggest an investigation of the characteristics of this tool, in these conditions, for the study of further improvements to the standard production tool.

7 Conclusions and future perspectives

This thesis investigated how to optimise the manufacturing of high-power laser diode chips mounted on carriers (CoC) in order to maximize the Degree of Polarization (DoP) of the light emitted.

Data analysis shows that there is a degradation of the DoP following the soldering of the CoC on the Heat Sink, but it shows as well that soldering using different tools produces different DoP. In fact, comparing the DoP results obtained with two mounting machines, *Lambda* and *Femto2,* the latter one being equipped or not with a particular tool (*Spring Tool)*, the higher value of DoP was statistically demonstrated with the machine *Femto2* equipped with the *Spring Tool*.

The *Spring Tool* is named after its springs that compensate for the sudden change in the applied force caused by reaching the gold melting temperature. Soldering with the *Spring Tool* was tested at the temperature used for standard soldering and at a lower temperature, the latter one gave the best results.

A mechanical profile analysis, conducted with a microscopic interferometer, showed that bowing is not a distinctive parameter of the type of soldering, but it was found that each tool usage is characterised by a certain profile shape, which can be considered as a fingerprint. Assumptions were made about the variation of these fingerprints after soldering, but further studies need to be carried out in order to parameterise each type of profile.

The work conducted during these months was important in order to create the basis for a future study, it was ascertained which direction to take next in order to approach an increase in DoP on the final laser, assembled on a package.

In addition, the data show the need to move from the study of macroscopic distortions (bowing) to investigations at the microscopic level. The work was partly planned, based on the literature found on the subject, and it will include XRD (X-Ray Diffraction), cross sections images with SEM (Scanning Electron Microscope), TEM (Transmission Electron Microscope), EDX (Energy-dispersive X-ray spectroscopy), and PL (Photoluminescence) analyses.

This thesis focused on a specific part of the production process but, as we have seen, the whole production process may affect the quality of the laser beams, so it is worth investigating.

One area is related to the crystalline phases of the AuSn alloy that are created during soldering. Further analysis, employing X-rays, may help to understand the extent of these phases.

Photoluminescence analyses of the samples can then be used to study the stresses induced by the soldering directly on the crystal lattice and possibly find a correlation between the microscopic deformation of the diode structure and the variation in DoP.

Acknowledgments

I would like to express my sincere thanks to professor Alessandro Martucci for his support and suggestions. I would also like to show my appreciation to the R&D Group at Prima Electro S.p.A, in particular to Claudio Coriasso for helping me finalize my project and to Alberto Maina for his guidance throughout the project. Then, I would like to express my sincere gratitude to Natascia De Leo who was the first to let me take part in this project by allowing me to collaborate with INRiM. Furthermore, I would also like to thank Fulvio Gaziano and Gertruda Martin for their time and attention.

Finally, my biggest thanks go to those who allowed me to study and obtain my Master's degree and who have always supported me by pushing me to give my best, namely my parents and grandparents.

Bibliography

[1] G. Ghione, Semiconductor Devices for High-Speed Optoelectronics, New York: Cambridge University Press, 2009.

[2] L. Coldren and C. Scott, Diode Laser and Photonic Integrated Circuit, Santa Barbara, California: Wiley, 1995.

[3] S. M. Sze and M.-K. Lee, Semiconductor Devices, New York: John Wiley & Sons, 1985.

[4] O. Svelto, Principles of Lasers, Milano: Springer, 1998.

[5] A. Yariv and Y. Arakawa, "Quantum Well Lasers-Gain, Spectra, Dynamics," *IEEE Journal Of Quantum Electronics,* pp. 1887-1899, 1986.

[6] X. Liu, W. Zhao, L. Xiong and H. Liu, Packaging of High Power Semiconductor Laser, London: Springer, 2015.

[7] T. Suhara, Semiconductor laser fundamentals, New York: Ny Dekker, 2004.

[8] S. W. Koch and M. R. Hofmann, Encyclopedia of Modern Optics, Elsevier, 2018.

[9] A. E. Siegman, "New developements in laser resonators," *SPIE vol. 1224,* pp. 1-14, 1990.

[10] T. Y. Fan, "Laser beam combining for high-power, high-radiance sources," *IEEE Journal of Selected Topics in Quantum Electronics,* pp. 567 - 577, 2005.

[11] M. Romain, A. Golebiowski, A. Champagne and J. M. Glinski, "Selective TE-TM mode pumping efficiencies for ridge-waveguide lasers in presence of stress," *IEEE Journal of Quantum Electronics,* p. 651–661, 1989.

[12] D. T. Cassidy and M. A. Fritz, "Photoelastic effect from die bonding of diode lasers," *Applied Optics,* pp. 160-166, 2004.

[13] R. Maciejko, J. M. Glinski, A. Champagne, J. A. A. Berger and L. Samson, "Photoelastic Effects on the Emission Patterns of InGaAsP Ridge-Waveguide Lasers," *Journal of Quantum Electronics,* pp. 651-661, 1989.

[14] M. Huang, "Stress effect on the performance of optical waveguides," *International Journal of Solids and Structures ,* p. 1615–1632, 2003.

[15] A. Maina, C. Coriasso, S. Codato and R. Paoletti, “Degree of Polarization of High-Power Laser Diodes: Modeling and Statistical Experimental Investigation,” *Applied Sciences,* pp. 1-11, 2022.

[16] “https://galvani.eu/,” [Online].

[17] K. Wasmer, C. Ballif, R. Gassilloud, C. Pouvreau, R. Rabe, J. Michler, J.-M. Breguet, J.-M. Solletti, A. Karimi and S. Daniel, “Cleavage Fracture of Brittle Semiconductors from the Nanometer tothe Centimeter Scale,” *Advanced Engineering Materials,* pp. 309-317, 2005.

[18] G. A. Slack, R. A. Tanzilli, R. O. Pohl and J. W. Vandersande, “The Intrinsic Thermal Conductivity of AlN,” *Journal of Physics and Chemistry of Solids,* pp. 641-647, 1987.

[19] C. Siminski, C. Dong and A. Russell, “Fluxless Die Attach by Activated Forming Gas,” in *Ipc apex expo conference proceedings*, Allentown, 2013.

[20] T. Namazu, H. Takemoto, H. Fujita, S. Nagai and Y. Inoue, “Self-propagating explosive reactions in nanostructured al/ni multilayer films as a localized heat process technique for mems,” *Proceedings of the IEEE International Conference on Micro Electro Mechanical Systems (MEMS),* pp. 286 - 289, 2006.

[21] E.-M. Bourim, I.-S. Kang and H. Y. Kim, “Investigation of Integrated Reactive Multilayer Systems for Bonding in Microsystem Technology,” *Micromachines,* pp. 1-28, 2021.

[22] A.-C. Pliska, J. Mottin, N. Matuschek and C. Bosshard, “Bonding Semiconductor Laser Chips : Substrate Material Figure of Merit and Die Attach Layer Influence,” *THERMINIC,* p. 2005, 76-83.

[23] C. Zweben, “New, low-CTE, ultrahigh-thermal-conductivity materials for lidar laser diode packaging,” *Proc. SPIE 58870D,* pp. 1-10, 2005.

[24] F. Bachmann, P. Loosen and R. Poprawe, “High Power Diode Laser Technology and Applications,” *Springer Science + Business Media,* pp. 394-403, 2000.

[25] C. Scholz, “Thermal and Mechanical Optimisation of Diode Laser Bar Packaging,” Master's Thesis, Aachen, 2007.

[26] M. Y. Tsai, C. H. Hsu and C. N. Han, “A Note on Suhir’s Solution of Thermal Stresses for a Die-Substrate Assembly,” *Journal of Electronic Packaging,* vol. 126, pp. 115-119, 2004.

[27] D. Pustan, E. Rastiagaev and J. Wilde, “In Situ Analysis of the Stress Development during Fabrication Processes of Micro-Assemblies,” *Electronic Components and Technology Conference,* pp. 117-124, 2009.

[28] W. D. Zhuang, P. C. Chang, F. Y. Chou and R. K. Shiue, “Effect of solder creep on the reliability of large area die attachment,” *Microelectronics Reliability,* vol. 41, pp. 2011-2021, 2001.

[29] S. Woods, “Understanding Materials Processing Lasers,” *Laser Technik Journal,* pp. 23-26, 2009.